Title

Enhancing the Performance of Supercapacitors by Hybrid Materials, Novel Electrolytes and Advanced Separators

Author

Li, Mengping

Publication Date

2018

Peer reviewed|Thesis/dissertation

UNIVERSITY OF CALIFORNIA

Los Angeles

Enhancing the Performance of Supercapacitors by Hybrid Materials, Novel Electrolytes and Advanced Separators

A dissertation submitted in partial satisfaction of the

requirements for the degree Doctor of Philosophy

in Chemistry

by

Mengping Li

2018

ABSTRACT OF THE DISSERTATION

Enhancing the Performance of Supercapacitors by Hybrid Materials,

Novel Electrolytes and Advanced Separators

by

Mengping Li

Doctor of Philosophy in Chemistry

University of California, Los Angeles, 2018

Professor Richard B. Kaner, Chair

Supercapacitors are widely used in our everyday life. They can supply power for portable electronic devices and electric vehicles as well as be utilized for energy recovery systems to improve energy efficiency. It is reported that the global supercapacitor market will be $2.12 billion by 2020 with an annual growth rate of 20.7%. The popularity of supercapacitors is due to their high power density, long cycle life and ability to work at low temperatures. However, state-of-art supercapacitors suffer from relatively low energy density, which has prevented them from being used in more applications. Besides, commercial cells are assembled with organic electrolytes to enlarge their potential window, which are expensive and flammable, far away from meeting the

standards of ideal energy storage devices. In order to enhance the performance of current devices, advanced electrode materials, electrolytes as well as novel separators are needed.

In this thesis, a hybrid material composed of carbon and nanostructured metal oxides as electrode materials is investigated. With the synergetic effects between the two compositions, the charge storage capability of the hybrid material is enhanced. To further boost the energy density of devices, the performance of commercial activated carbon supercapacitors was enhanced by a combination of a laser scribing process and a redox electrolyte. In this way, the energy density obtained was nine times higher than the commercial device, while using a safer and less expensive aqueous electrolyte. Additionally, supercapacitors were integrated with energy harvesting devices to build self-powered systems. A self-charging power pack was fabricated based on a combination of a solar cell and a supercapacitor which is able to harvest 2.92% of the solar energy. Moreover, a self-charging supercapacitor was fabricated by using a piezoelectric separator. The device can harvest energy from the ambient environment and be charged to 0.2 V simply by pressing with one's palm.

The dissertation of Mengping Li is approved.

Yu Huang

William M. Gelbart

Richard B. Kaner, Committee Chair

University of California, Los Angeles

2018

I would like to delicate this dissertation to my family:

my parents, my grandparents and my husband for their love and support, without whom it would be impossible for me to finish this dissertation.

TABLE OF CONTENTS

LIST OF FIGURES

LIST OF TABLES

ACKNOWLEDGEMENTS

The five years as a graduate student in UCLA is a great adventure for me. I've learned and experienced so much thanks to all the kind people I've met.

First, I'd like to thank my advisor Professor Richard B. Kaner who is an awesome guide for my adventure. Ric is a very nice and understanding person who has the vision for research. He gives me freedom to choose the projects I like and never hesitates to help when I need guidance or support. His advice on research and life encourages me to learn and grow. Going to UCLA to work with Ric is definitely one of the best choices I've ever made! I would also like to thank my committee members, Professor Kendall N. Houk, Professor William M. Gelbart and Professor Yu Huang for their excellent advice for my research and career.

Dr. Maher F. El-Kady is another person who helped me so much for my adventure. He has been my mentor since 2012 when I was an exchange student at UCLA. Being an expert in the energy storage field, he is the person who introduced me to the world of supercapacitors. Whenever I have questions on my research, he is able to provide me with useful advice. Maher also helped me a lot when I needed to interpret data and write papers. I can't remember how many times he helped me out. I really appreciate that!

My adventure as a graduate student could be rather difficult if I don't have so many colleagues to support me for my research. I'd like to express my acknowledgements to Dr. Jee Youn Hwang, who worked closely with me on several projects. She taught me how to work efficiently and smartly hand by hand. Without her help, it is not possible for me to have such a good and smooth experience. It is also a great pleasure to work with Dr. Hanhui Liu, Haosen Wang, Dr. Lisa Wang, and Dr. Yuanlong Shao during my Ph.D. study. Not to mention the support I've

received from other colleagues in the Kaner lab: Matthew D. Kowal, Kris Marsh, Cheng-Wei Lin, Chris Turner, Brian McVerry, Jialin Lei, William Huang, Zhijuan Zhao, Michael Yeung, Jessica Wang, Georgiy Akopov, Wai Mak, Mit Muni, Stephanie Aguilar, Lisa Pangilinan, Volker Strauss and Mackenzie Anderson. Thank you all for your support!

It's also lucky for me to have several close friends, Yan Yan, Leyi Pan and Yuan Jin to accompany me during my adventure. It would be a lonely journey not for my dearest buddies! We are excited about our achievements but also support each other during bad times. They give me the strength to stand up and continue my adventure. Thank you for always being there for me and wish you all good luck with your own adventures!

Last but most importantly, I would like to express my sincere gratitude to my family, without whom I would not even start this wonderful adventure. Many thanks to my parents Jian Li and Gennan Yao, my role models who protect my curiosity and teach me how to learn. They are always by my side and encourage me to pursue the life I want. I'd like to thank my grandparents Haiquan Li and Xiuying Chen for their unconditional love. I also want to thank my husband Dr. Chengjie Wang, who always understands me and backs me up whenever I encounter difficulties.

Previous Publications and Contributions of Co-authors:

Chapter 2 is a version of M. Li, M.F. El-Kady, J.Y. Hwang, K. Marsh, H. Wang, M. Kowal, and R.B. Kaner, "Fabricating Hollow Co_3O_4/LSG Composite for High Performance Supercapacitors". M. Li designed the research, M. Li built the supercapacitors and carried out electrochemical analysis with M.F. El-Kady. M. Li performed the SEM, XRD and TGA tests. M. Li and J.Y. Hwang did the TEM imaging together. K. Marsh collected the XPS data and M. Kowal did the Raman spectra. M. Li and M.F. El-Kady wrote the manuscript. R.B. Kaner supervised the projects and provided suggestions on manuscript writing. All authors were involved in data interpretation, results discussion and manuscript review. This project was funded by the China Scholarship Council (CSC) and Nanotech Energy, Inc. This manuscript was accepted and published online by *Nano Research* in December 2017.

Chapter 3 is a version of J.Y. Hwang*, M. Li*, M.F. El-Kady, and R.B. Kaner, "Next-Generation Activated Carbon Supercapacitors: A Simple Step in Electrode Processing Leads to Remarkable Gains in Energy Density" (**both authors contributed equally*). J.Y. Hwang, M. Li and M.F. El-Kady designed the research. M. Li and J.Y. Hwang synthesized the electrodes, carried out electrochemical experiments and other characterization together. M. Li analyzed the data and prepared the graphs. M.F. El-Kady did the optical microscope analysis. J.Y. Hwang and M.F. El-Kady prepared the manuscript. R.B. Kaner supervised the project and provided a lot of suggestions on data presentation and manuscript writing. All authors were involved in results discussions and manuscript review. This project was funded by the China Scholarship Council (CSC) and Nanotech Energy, Inc. This manuscript was published by *Advanced Functional Materials* in April 2017.

Chapter 4 is a version of M. Li, J.Y. Hwang, M.F. El-Kady, B.T. McVerry, S. Xue, R.B. Kaner, "Integration of the Porous PVDF for a Self-charging Supercapacitor". M. Li, J.Y. Hwang and M.F. El-Kady designed the research. M. Li and J.Y. Hwang carried out the material fabrication, electrochemical analysis and other characterization. B.T. McVerry collected the FTIR data, while S. Xue contributed to the scheme design in the manuscript. R.B. Kaner supervised this project and provided suggestions on data presentation and manuscript writing. All authors were involved in results discussions and manuscript review. This project was funded by the China Scholarship Council (CSC) and Nanotech Energy, Inc. The manuscript is in preparation and will be submitted soon.

Chapter 5 is a version of H. Liu*, M. Li*, R.B. Kaner, S. Chen, Q. Pei, "A Monolithically Integrated Self-charging Power Pack Consisting of Silicon Nanowires Array/PEDOT:PSS Hybrid Solar Cell and Laser-scribed Graphene Supercapacitor" (**Both authors contributed equally*). H. Liu and M. Li designed the project, synthesized the material and did characterization together. H. Liu wrote the manuscript. R.B. Kaner, S. Chen and Q. Pei supervised the project and suggested data interpretation and manuscript preparation. All authors were involved in results discussions and manuscript review. This project was funded by the China Scholarship Council (CSC) and Nanotech Energy, Inc. The manuscript has been accepted by *ACS Applied Materials and Interfaces*.

VITA

2010	National Fellowship, Chinese Ministry of Education
2012	Junzheng Scholar (funded by Nobel Prize Winner: Tsung-Dao Lee)
2012	National Fellowship, Chinese Ministry of Education
2013	B.S., Materials Science, Fudan University
2013-2016	Graduate Student Fellowship
2017-2018	Dissertation Year Fellowship

PUBLICATIONS AND PRESENTATIONS

1. **M. Li**, M.F. El-Kady, J.Y. Hwang, K. Marsh, H. Wang, M. Kowal, and R.B. Kaner, "Fabricating Hollow Co_3O_4/LSG Composite for High Performance Supercapacitors", Accepted by *Nano Research*

2. **M. Li**, J. Y. Hwang , M. El-kady, B. McVerry, and R. B. Kaner, "Integration of Porous Piezoelectric Separator for a Self-Charging Supercapacitor", *In-preparation*

3. J.Y. Hwang*, **M. Li***, M.F. El-Kady, and R.B. Kaner, "Enhancing the energy density of commercial activated carbon supercapacitors using a combination of laser scribing technique and redox electrolyte", *Advanced Functional Materials*, **27**(15), 1605745. (*Both authors contributed equally)

4. H. Liu, **M. Li***, R.B. Kaner, S. Chen, Q. Pei, "A Monolithically Integrated Self-charging Power Pack Consisting of Silicon Nanowires Array/PEDOT:PSS Hybrid Solar Cell and Laser-scribed Graphene Supercapacitor", accepted by *ACS Applied Materials and Interfaces* (*Both authors contributed equally)

5. M.F. El-Kady, M. Ihns, **M. Li**, J.Y. Hwang, M.F. Mousavi, L. Chaney, A.T. Lech and R.B. Kaner, (2015). "Engineering three-dimensional hybrid supercapacitors and microsupercapacitors for high-performance integrated energy storage", *Proceedings of the National Academy of Sciences*, **112**(14), 4233-4238.

6. J.Y. Hwang, M.F. El-Kady, **M. Li**, C.W Lin, M. Kowal, X. Han and R.B. Kaner, "Boosting the Capacitance and Voltage of Aqueous Supercapacitors via Redox Charge Contribution from the both Electrode and Electrolyte", *Nanotoday*, **15**, 15-25.

7. Z. Zhao, K. J, J.C. Shaw, Z. Zhu, W. Wan, L. Zhan, **M. Li**, H. Wang, X. Chen, Z. Li, S. Chen, Y. Zhou, R. B. Kaner, and W.Cai, (2016) "Synthesis of sub-millimeter Bi-/multi-layer graphene by designing a sandwiched structure using copper foils", *Applied Physics Letters*, **109**, 123107.

8. R.B. Kaner*, M.F. El-Kady, Y. Shao, J.Y. Hwang, L. Wang, **M. Li**, H. Wang, M. Kowal, W. Sun, S. Cho and R. Rizvi, (2016, April). Contributed Presentation on (Invited) "Electrochemical Capacitors Based on Graphene", Meeting Abstracts (No. 6, pp. 565-565). The Electrochemical Society.

9. R.B. Kaner*, M.F. El-Kady, L. Wang, J.Y. Hwang, Y.Shao, **M. Li**, H.Wang, J.M. Ko, M, Mousavi, Contributed Presentation on "Graphene-based supercapacitors", AMN7 Advanced Materials & Nanotechnology, Nelson, New Zealand, February 8-12 2015.

CHAPTER 1

Introduction

1.1 Global energy crisis and the challenges for state-of-the-art energy storage devices

According to the world energy council[1], energy is one of the most crtical issues today. Figure 1.1 lists the impact and uncertainty of world issues. As can be seen, the majority of the world problems involve energy such as energy subsides, energy efficiency and renewable energy. This is not hard to understand since almost everything we rely on needs energy: our cars need energy to move, portable electronic devices need energy to run and our society needs energy to function.

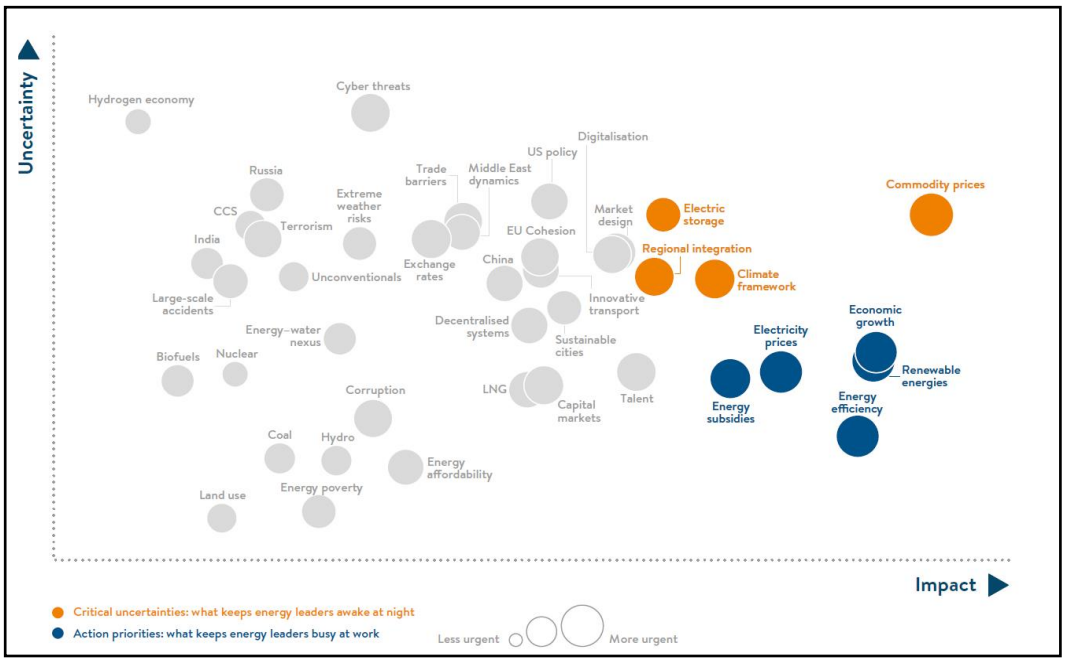

Figure 1.1 The impact and uncertainty of world issues[1]

Owing to the continuously growing population around the world, there has been an increasing demand for energy. However, oil and other fossil fuels have dominated the market for

the past 50 years (Figure 1.2). Although the oil market has been dropping for the past 15 years, it still occupies 1/3 of the market. Relying on fossil fuels not only means that we are using up this valuable nonrenewable energy resource, but it also adds a lot of greenhouse gases to the atmosphere, causing global warming. To prevent more greenhouse gas release, many efforts have been put into renewable energy resources such as solar, wind and water power. As a result, renewables have increased rapidly over the last 5 years, now accounting for a record 3.2% of global primary energy consumption.

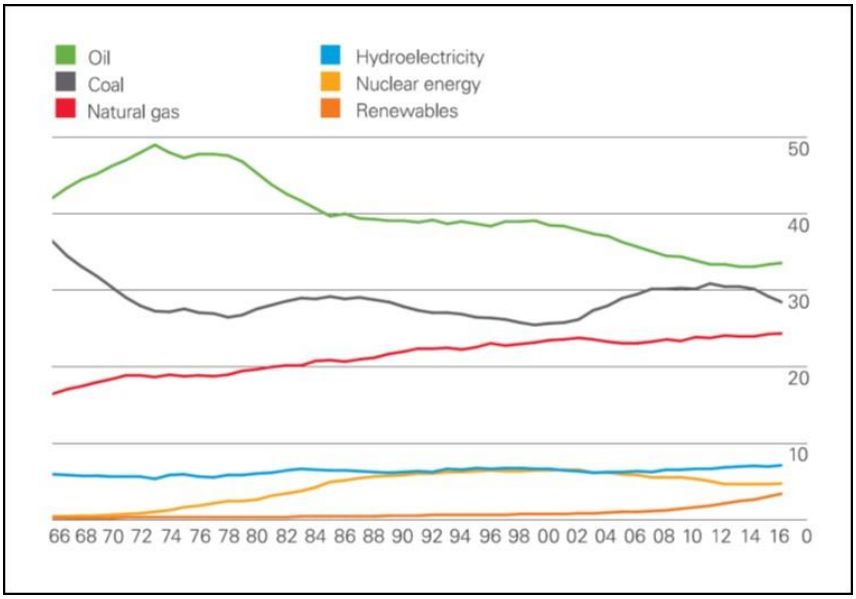

Figure 1.2 Shares of World Primary energy [2]

Since some of the renewable energy resources are not sustainable over time, reliable energy storage equipment is needed to save energy for future use. Batteries, especially lithium ion batteries are good candidates to store the energy thanks to their relatively high energy density. Unfortunately, they suffer from low power density, poor cycle life and are not able to work at low temperature. Besides, there have been reports about battery explosions which also limits the application of batteries. In contrast, electrochemical capacitors also known as supercapacitors, can

have very high power density and cycle life, but experience low energy density. Due to the miniaturization of electronic devices, there is also a demand for small, lightweight and even flexible power sources. Therefore, a lot of effort is needed to improve the performance of state-of-the-art energy storage devices.

1.2 Supercapacitors versus batteries

As discussed above, supercapacitors and batteries are popular energy storage devices. Both devices have two electrodes in the electrolyte separated by a separator film to prevent short circuits. In addition, the energy storage process in batteries and supercapacitors both occur on the phase boundary between the electrodes and electrolyte interfaces.[3] While the two devices share similarities, they also have essential differences. A battery stores energy by redox reactions in its cathode and anode, where phase transitions of the electrode materials usually take place.[4] The potential of the battery results from the chemical potential difference between the two electrodes, which can be determined by the Nernst equation. Ideally, its potential is constant during charging and discharging as demonstrated in Figure 1.3. On the contrary, a supercapacitor stores energy electrostatically or electrochemically. Its potential depends on the state of charge Q and thus is related to the state of charge as the curve shows in the image below.

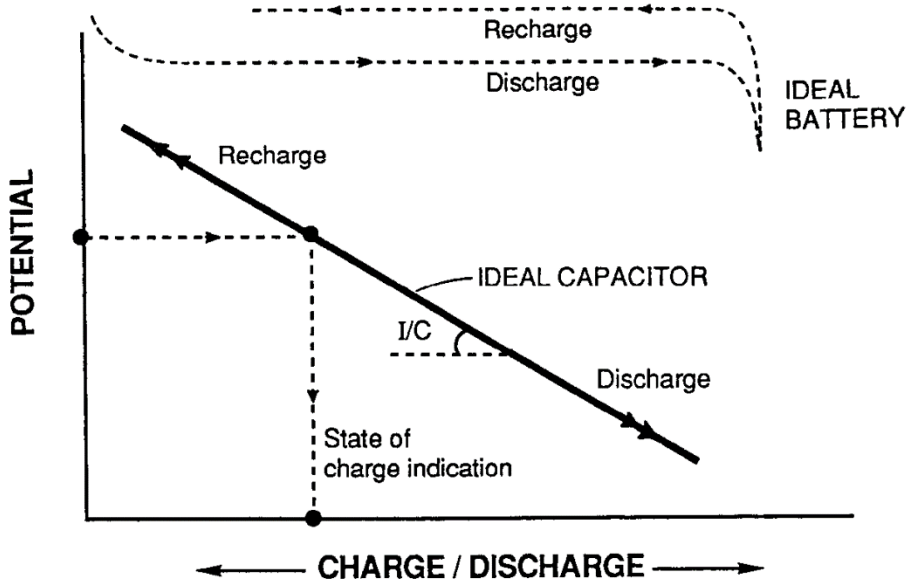

Figure 1.3 Difference of discharge and recharge relations for a capacitor and a battery: potential as a function of state of charge, Q. [5]

Because of their dissimilarity in charge storage mechanisms, batteries and supercapacitors display their own unique properties. Figure 1.4 is a Ragone plot comparing the power and energy densities of traditional capacitors, supercapacitors and batteries. Energy density describes the energy storage capacity of a device, while power density refers to the energy delivery rate. If we take an electric car as an example, energy density will be how far the car can travel and power density will be how fast the car can go. As the gray dot in the left corner indicates, traditional capacitors exhibit ultrahigh power densities, but their energy densities are rather low. Different from traditional capacitors, batteries show good energy densities, but they experience poor power densities. Supercapacitors bridge the gap between batteries and capacitors by having the intermediate energy and power densities. Figure 1.5 is a detailed comparison

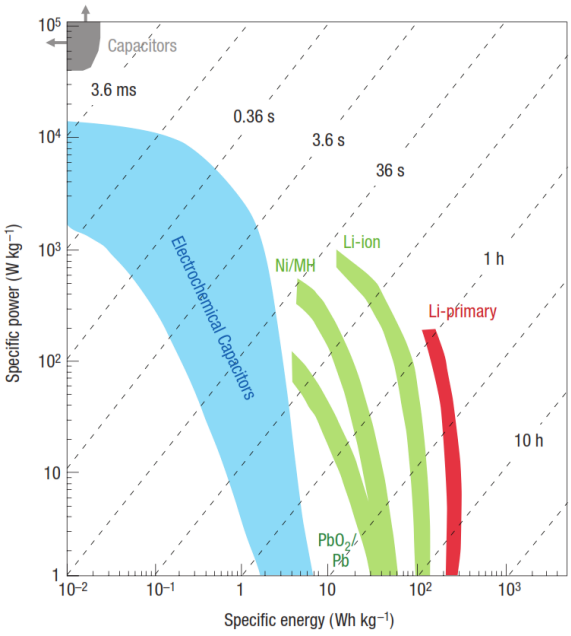

Figure 1.4 Ragone plot comparing traditional capacitors, supercapacitors and batteries. [6]

between lithium ion batteries and carbon based supercapacitors. We can learn from the graph that a supercapacitor is superior to a Li-ion battery by having higher power density and longer cycle life. It is also suitable to work at low temperatures. Nevertheless, a supercapacitor shows much lower energy density, typically only 5 Wh/kg compared to 100-100 Wh/kg for a lithium ion battery. This is the biggest problem with state-of-the-art supercapacitors.

Caracteristics	Li-ion baterries	ECs (EDLCs)
Power (kW/kg)	< 1**	> 10
Energy (Wh/kg)	100 - 150	5
Cycle Life	< 5000 (@C)	> 1 000 000
Discharge time*	3-5 min.	~ 1s
Charging time*	> 6 min.	~ 1s
Temperature (°C)	-20°C - +70°C	-40°C - +70°C
Efficiency	70% - 95%	> 95%
Cost (€ per Wh)	0.8 – 1.5	8 - 15
Cost (€ per kw)	60 – 120	20 - 40

Figure 1.5 Characteristics of lithium ion batteries and electric double-layer capacitors.[7-8]

1.3 Objectives of the thesis

This dissertation is dedicated to solving the problem of present supercapacitors. Novel electrode materials, electrolytes and separators are investigated to improve the performance of supercapacitors:

1) To boost their energy density, while maintaining good power density.

2) To improve the conductivity and cycle life of the cell.

3) To achieve high voltage using safer aqueous electrolytes.

4) To use inexpensive and environmentally friendly materials.

5) To create self-charging power units for portable electronic devices.

1.4 Energy storage mechanism for supercapacitors

There are two main types of supercapacitors classified by their charge storage mechanisms. One is called electric double-layer capacitors (EDLCs) which stores charges electrostatically. The other kind of supercapacitor stores energy by electrochemical reactions on its surface and is named pseudo- or battery-like capacitors depending on the specific electrode material.

1.4.1 Mechanism for electric double-layer capacitors (EDLCs)

The schematic image in Figure 1.6 compares the structure of a traditional capacitor and a supercapacitor. A traditional capacitor is composed of two metal plates separated by dielectric materials in between. The typical distance between separated charges is usually on the micrometer length

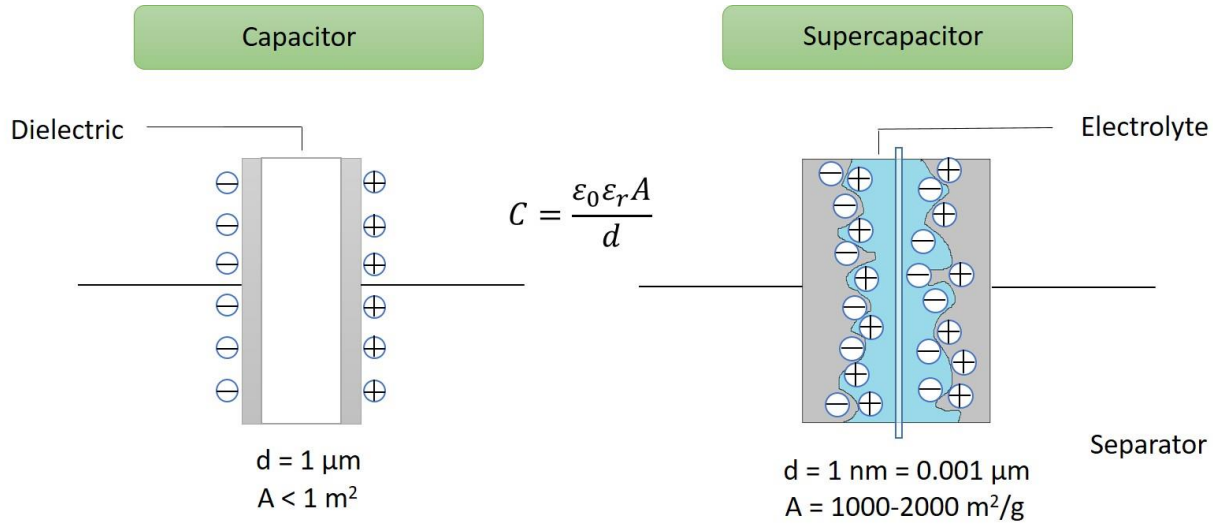

Figure 1.6 Schemes of a traditional capacitor and a supercapacitor

scale and the surface area of the whole device is less than 1 m^2. Similarly, a supercapacitor also has a sandwich structure with two electrodes and a separator. Electrolyte is also used in contact with the two electrodes. When the energy is provided in the form of electricity, electron transfer takes place and the charges in the EDLC's electrodes are held electrostatically. At the same time, the electrolyte ions are attracted by the opposite charges and absorb at the interface of the electrolyte and electrode to stabilize the charge stored, forming an electric double layer as Figure 1.6 illustrates. The distance between separated charges is around 1 nm and the surface area of the electrode material is usually 1000-2000 m^2/g. Based on the equation：

$$C = \frac{\varepsilon_0 \varepsilon_r A}{d} \quad (1.1)$$

(C is the capacitance, A is surface area of the active material, d is the distance of the separated charges, ε_0 is the permittivity of vacuum and ε_r is the dielectric constant of the electrolyte), the capacitance is proportional to A and is inversely proportional to d. Thanks to the huge surface area and small distance between charges, a supercapacitor has a much higher capacitance than a

traditional capacitor. Besides, proper control of the pore sizes of the active material based on the specific electrolyte is important to get optimal performance out of the supercapacitor.[10]

1.4.2 Mechanism for Pseudo- or battery-like capacitors

Although EDLCs can have very large surface areas, their capacitance is not good enough to satisfy the demand for high-energy power sources. To seek materials with good energy storage performance, scientists began to study a second type of supercapacitor. Different from the charge storage process in EDLCs, pseudo- or battery-like capacitors store charge by fast and reversible Faradaic reactions from the electrode material. As Figure 1.7 shows, MnO_2 on the negative electrode will get an electron and be reduced to $NaMnO_2$ when the cell is charging. In this way, charge can be stored. When it comes to the discharging process, the reverse reaction occurs and the stored electrons are released. Note that, only the materials displaying rectangular CV profiles as EDLCs can be defined as pseudo-capacitive. Supercapacitors composed of materials with distinct redox peaks are battery-like capacitors and their charge storage capability is evaluated with capacity (C/g) instead of capacitance (F/g).[11] The energy storage capacity of the pseudo- or battery-like capacitor is much higher than EDLCs due to the energy-dense Faradaic processes. However, they often suffer from slower charge/discharge rates and thus lower power densities.

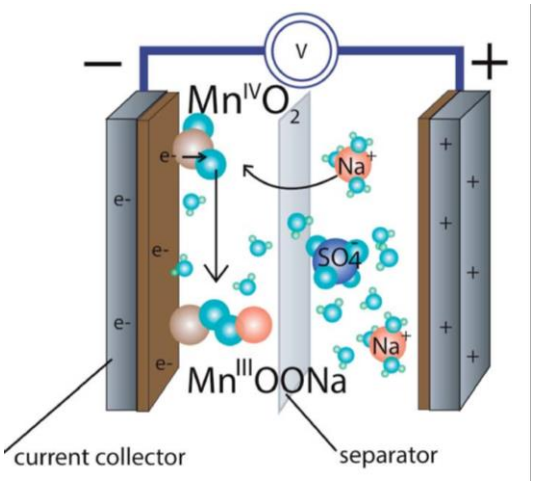

Figure 1.7 Basic schematics for a pseudo-capacitor composed of MnO_2.[12]

To combine the advantages of both types of supercapacitors, hybrid capacitors are introduced. Hybrid capacitors are made either by utilizing symmetric redox active material/carbon composite electrodes or an asymmetric structure (pseudo- or battery-like anode with EDLC cathode). Table 1 is a summary of diverse kinds of supercapacitors. The hybrid capacitor is able to get both high energy and power as well as good cyclability.

Table 1.1 Summary of Different Types of Supercapacitors[13]

Type of supercapacitor		Electrode material	Charge storage mechanism	Merits/shortcomings
Electrochemical double layer capacitor (EDLC)		Carbon	Electrochemical double layer (EDL), non-Faradaic process	Good cycling stability, good rate capability, low specific capacitance, low energy density
Pseudocapacitor		Redox metal oxide or redox polymer	Redox reaction, Faradaic process	High specific capacitance, relatively high energy density, relatively high power density, relatively low rate capability
Hybrid capacitor	Asymmetric hybrid	Anode: pseudocapacitance materials, cathode: carbon	Anode: redox reaction, cathode: EDL	High energy density, high power density and good cyclability
	Symmetric composite hybrid	Redox metal oxide/carbon or redox polymer/carbon	Redox reaction plus EDL	High energy density, moderate cost and moderate stability
	Battery-like hybrid	Anode: Li-insertion material, cathode: carbon	Anode: Lithiation/delithiation cathode: EDL	High energy density, high cost and requires electrode material capacity match

1.5 Materials for supercapacitors

1.5.1 Materials for EDLCs

EDLC materials are basically all carbon. The carbon materials studied can be sorted based on their dimensions as Figure 1.8 exhibits. Among all the materials, activated carbon (AC) is still the most widely used. As we discussed in the previous sections, high surface area is desirable to get high capacitance. Based on the activation process, the surface area of activated carbon is between 1000 to 2000 m^2/g resulting from its well-aligned pore structure. There are three kinds of pores in AC: macropores, mesopores and micropores. Macropores are the largest pores with sizes

over 50 nm. These serve as the electrolyte reservoir and ion pathways. Mesopores are between 2-50 nm, where most of the ion adsorption and desorption take place, and contribute to most of the capacitance. Micropores are actually nanopores which are smaller than 2 nm. This kind of pore is too small for electrolyte ion to diffuse into. As a result, not all the surface area in AC are accessible and will deliver capacitance. Moreover, the conductivity of the activated carbon is compromised by the oxygen-containing groups on its surface. Therefore, AC is not the ideal EDLC material for supercapacitors.

Figure 1.8 Summary of Different Carbon Materials[9]

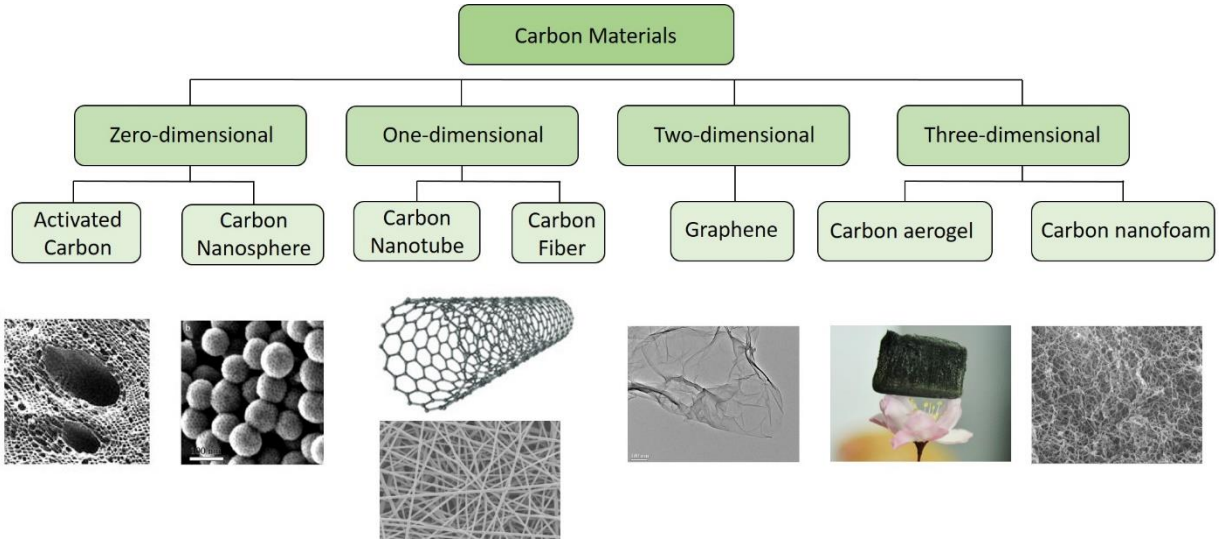

In recent years, one-dimensional carbon nanotubes (CNTs) and two-dimensional graphene have attracted great attention. They both exhibit high surface area (1315 m^2/g for SWCNTs[14] and 2630 m^2/g for graphene[15]) and good electric conductivities. Theoretically, graphene can obtain a capacitance of 550 F/g. However, excellent properties of this kind of material will not necessarily translate into good device performance due to the low packing density (<0.5 g/cm^3).[16] As a result, efforts are still needed to develop good carbon materials for supercapacitors. The performance of diverse carbon materials are summarized in Table 2.

Table 1.2 Properties and Characteristics of Various Carbon Materials as Supercapacitor Electrodes[9]

Materials	Specific surface area/m^2 g^{-1}	Density/g cm^{-3}	Aqueous electrolyte /F g^{-1}	Aqueous electrolyte /F cm^{-3}	Organic electrolyte /F g^{-1}	Organic electrolyte /F cm^{-3}
Carbon materials						
Commercial activated carbons (ACs)	1000–3500	0.4–0.7	< 200	< 80	< 100	< 50
Particulate carbon from SiC/TiC	1000–2000	0.5–0.7	170–220	< 120	100–120	< 70
Functionalized porous carbons	300–2200	0.5–0.9	150–300	< 180	100–150	< 90
Carbon nanotube (CNT)	120–500	0.6	50–100	< 60	< 60	< 30
Templated porous carbons (TC)	500–3000	0.5–1	120–350	< 200	60–140	< 100
Activated carbon fibers (ACF)	1000–3000	0.3–0.8	120–370	< 150	80–200	< 120
Carbon cloth	2500	0.4	100–200	40–80	60–100	24–40
Carbon aerogels	400–1000	0.5–0.7	100–125	< 80	< 80	< 40

1.5.2 Pseudo-capacitive and battery-like materials

Conducting polymers and transition metal oxides and are the typical pseudo- and battery-like materials for supercapacitors. Conducting polymers such as polyaniline, polythiophene, polypyrrole and poly(3,4-ethylenedioxythiophene) (PEDOT) have been studied for use as supercapacitor materials for their good capacity and conductivity.[17] But they experience the problems of low power and cycle life which limits their applications. Transition metal oxides also demonstrate good charge storage capability thanks to their energy-dense redox reactions. The characteristic of common metal oxides are listed in Table 3. The capacitance of a pseudo-capacitive material can be determined by the equation[13]:

$$C = \frac{n \times F}{M \times V} \tag{1.2}$$

Where C is the capacitance in F/g, n is the number of electrons transferred in the redox reaction, F is the Faraday constant, M is the molecular weight of the active material, and V is the working voltage window. Take MnO_2 as an example, its theoretical capacitance can be calculated as:

$$C_{MnO_2} = \frac{1 \times 96485\ C/mol}{87\ g/mol \times 0.8\ V} = 1386\ F/g$$

If the material belongs to the category of battery-like materials, its capacity can be derived from:

$$C = \frac{n \times F}{M} \tag{1.3}$$

However, the table also reveals the inherent drawbacks of this type of material. Most of the metal oxides except for RuO_2 are not very conductive. Accordingly, the sheet resistance and charge transfer resistance of metal oxide electrodes will increase, leading to poor power

Table 1.3 Charge Storage Capability and Conductivity of Selected Metal Oxides[9]

Oxide	Electrolytes	Charge Storage Mechanism	Theoretical Capacity/Capacitance	Conductivity (S/cm)
MnO_2	Na_2SO_4	$MnO_2{}^+ M^+ + e^- = MMnO_2$ (M could be H^+, Li^+, Na^+, K^+)	1380 F/g	$10^{-5} – 10^{-6}$
NiO	KOH, NaOH	$NiO + OH^- = NiOOH + e^-$	1292 C/g	0.01 – 0.32
Co_3O_4	KOH, NaOH	$Co_3O_4 + OH^- + H_2O = 3CoOOH + e^-$ $CoOOH + OH^- = CoO_2 + H_2O + e^-$	1607 C/g	$10^{-4} – 10^{-2}$
V_2O_5	Na_2SO_4, NaCl	$V_2O_5 + 4M^+ + 4e^- = M_2V_2O_5$ (M could be H^+, Li^+, Na^+, K^+)	2120 F/g	$10^{-4} – 10^{-2}$
RuO_2, xH_2O	Na_2SO_4, H_2SO_4	$RuO_2 + xH^+ + xe^- = RuO_{2-x}$, $(OH)_x$ $(0 < x < 2)$	1200-2200 F/g	1000 – 1

density and rate capability. In addition, strain will develop in the metal oxide during charge/discharge processes which can result in cracking of electrodes, limiting the long-term stability and cyclability of the supercapacitors. To enhance the electrochemical performance of the metal oxide, carbon materials are used to make composites with them. By doing the hybridization, the metal oxide gets physical support as well as channels for electron transport. The hybrid material is thus expected to have improved power density and rate capability. At the same time, the high charge storage capability of the metal oxide will boost the capacity of the whole material. Therefore, fabrication of carbon and pseudo-capacitive/battery-like materials is the way to go for future supercapacitors.

1.6 Characteristics of supercapacitors and evaluation methods

Capacitance (capacity), voltage window, equivalent series resistance, power density and energy density are the common criteria to assess the performance of a supercapacitor. Figure 1.9 demonstrates the important performance metrics, test methods and major influence factors for the evaluation of supercapacitors.[18] They are discussed in detail in the following section.

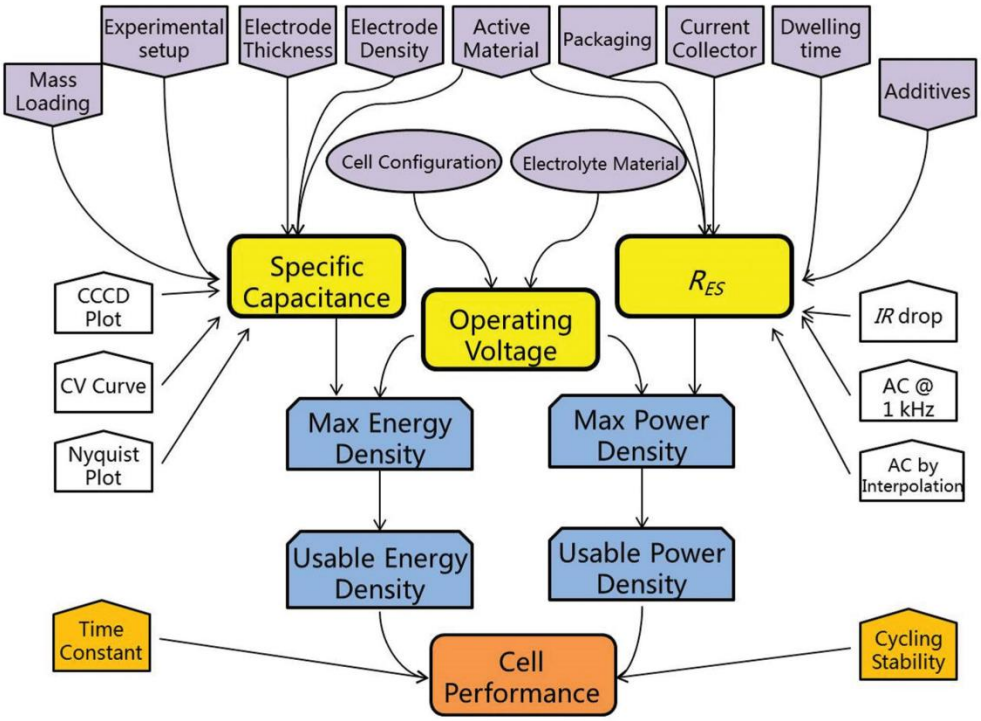

Figure 1.9 An illustration of key performance metrics, test methods, and major affecting factors for the evaluation of supercapacitors.[18]

1.6.1 Capacitance/capacity

Capacitance or capacity reveals the charge storage capability of the electrode material. It is the most important parameter for supercapacitors, which is closely related to the active material, electrode thickness and the electrolyte. The capacitance/capacity can be derived from cyclic

voltammetry (CV), constant current charge/discharge (CC) or electrochemical impedance spectroscopy (EIS).

Cyclic voltammetry is a potentiodynamic electrochemical measurement in which the instantaneous current is recorded when the potential of the working electrode is changed in a certain rate with time. When the potential reaches the set point, it will ramp in the opposite direction. Note that CV is also the most suitable method to study the charge storage mechanism of the active materials. For an adsorption-based mechanism, the current in the CV is proportional to the scan rate, while the current of a diffusion controlled process shows a linear relation with the square root of the scan rate.[19] As a result, the charge storage mechanism can be confirmed by assessing the CV data. Since capacitance is defined as the charge stored divided by the potential window, it can be calculated based on the CV using the equation:

$$C = \frac{\int_{V_1}^{V_2} idV}{v\,(V_2 - V_1)Y} \tag{1.4}$$

Where V_1 and V_2 are the potential range in Volts, i (A) is the instantaneous current, v (V/s) is the scan rate and Y is the volume, mass or area of the electrode. According to Y, the specific capacitance (F/g), the volumetric capacitance (F/cm^3) and the areal capacitance (F/cm^2) can be derived. For battery-like materials, capacity is used so that the charge stored is calculated instead:

$$C = \frac{\int_{V_1}^{V_2} idV}{v\,Y} \tag{1.5}$$

In addition to CV, CC is another way to evaluate the charge storage capability of the material. It is basically a repeated charging/discharging process at a constant current density. CC is widely used due to its accuracy and convenience. The capacitance is usually calculated based on the discharge curve:

$$\mathrm{C} = \frac{i\Delta t}{V_2 - V_1 - IR_{drop}} \ (\Delta t \ is \ the \ discharging \ time) \tag{1.6}$$

The capacitances derived from CV and CC under similar current density should be consistent with each other.

Besides, EIS can be utilized to evaluate the capacitance as well. It is carried out by measuring the impedance of the device as a function of the frequency. [18] According to Miller, et al.,[20] the capacitance is:

$$\mathrm{C} = -\frac{1}{2\pi f Z''} \tag{1.7}$$

Where f (Hz) is the frequency at the -45° phase angle and Z'' is the imaginary part of the impedance.

As illustrated above, there are three main methods to analyze the capacitance. We should choose the one that best suits the active material and available equipment. For real world applications, supercapacitors are often aligned in series or parallel to optimize the current and voltage. The series and parallel capacitance C_{series} and $C_{parallel}$ have the following relation with their component capacitors (C_1, C_2…), respectively:

$$\frac{1}{C_{series}} = \frac{1}{C_1} + \frac{1}{C_2} + \cdots \tag{1.8}$$

$$C_{parallel} = C_1 + C_2 + \cdots \tag{1.9}$$

1.6.2 Voltage window

Voltage window refers to the safe voltage range a cell can perform normally without the degradation of either electrolyte or electrode. It can be evaluated by both CV and CC. A small potential is tried on the device first and then one keeps raising the applied potential until a sharp spike shows up as displayed in Figure 1.10. The highest voltage before the appearance of the spike

is the voltage window. The voltage window is determined by the active material, the device configuration and the electrolyte. For aqueous symmetric systems, they usually have a 1 V voltage window, limited by the water decomposition voltage of 1.23 V. Since a large voltage window helps bring higher energy and power densities, asymmetric supercapacitors,[21] organic electrolytes[22] and ionic liquids[23] have been applied to increase the operating voltage.

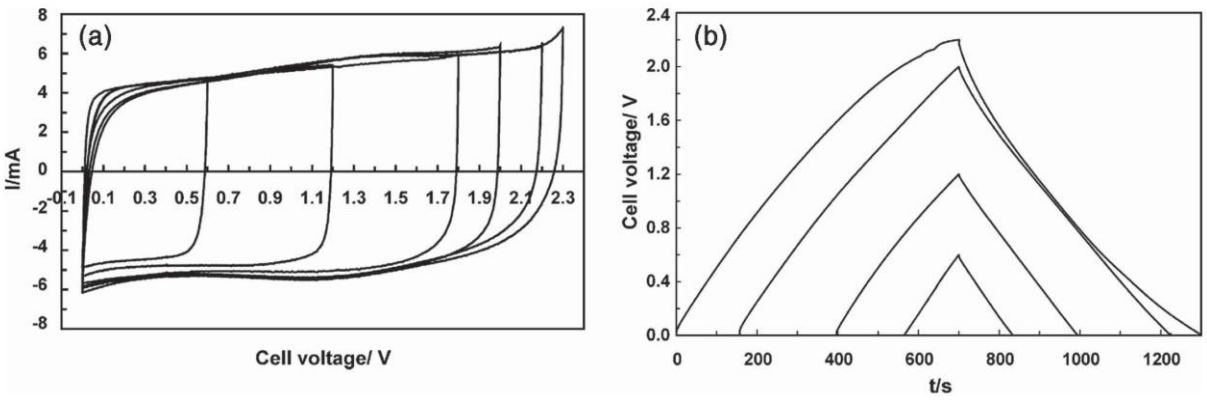

Figure 1.10 Illustration of voltage window determination by (a) CV, and (b) CC.[24]

1.6.3 Equivalent series resistance (ESR)

The ESR is another important property of a supercapacitor. It can affect the power density, rate capability and even cycle life of the cell. As Figure 1.11A illustrates, supercapacitors not only

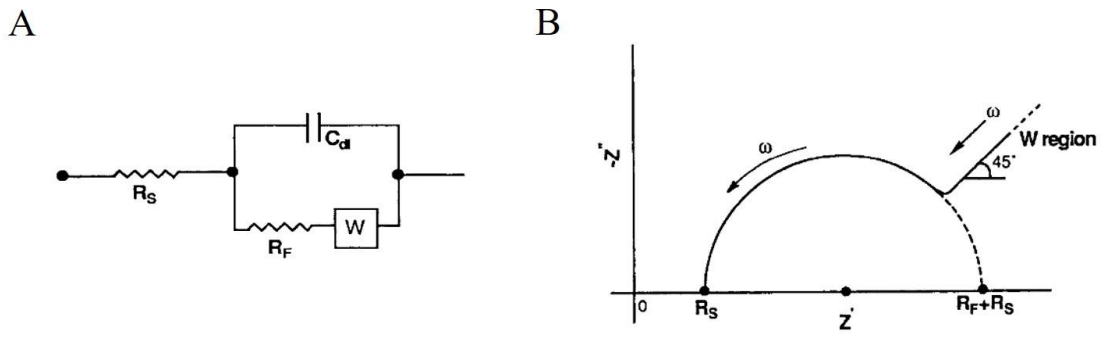

Figure 1.11 (A) Equivalent circuit, (B) complex impedance plot for a Faradaic process involving transition to diffusion control at low frequency.[5]

have the capacitor part C_{dl} in the equivalent circuit, they can also have internal resistance R_s, charge transfer resistance R_F or other impedance components W. One simple technique to find out the ESR is CC. At the beginning of the discharging curve, there is usually a voltage fall caused by the ESR named the IR drop. The Resistance is calculated as[18]:

$$\text{ESR} = \frac{IR_{drop}}{2i} \ (i \ is \ the \ constant \ current \ used) \tag{1.10}$$

In the equation, 2 i is used because the current change at the start of discharge is i - (- i) = 2 i. This method works best with small-sized supercapacitors.

The other way to evaluate ESR is electrochemical impedance spectroscopy. A typical EIS data (Nyquist plot) is exhibited in Figure 1.11B. The ESR is defined as the real part of the plot at the frequency of 1 KHz.[25] Sometimes, people also use the intercept of the reverse extension of the low-frequent plot and the x axis as ESR.[18] In addition to the ESR value, a list of detailed information can be achieved through a Nyquist plot where R_s is the intercept of the curve and $Z'' = 0$ is the sum of the active material resistance, the ionic resistance of the electrolyte and the interfacial contact resistance. The semicircle following R_s is an indication of the charge transfer resistance, which often appears in redox active systems. Moreover, the 45° tail after the semicircle is related to the ion diffusion process and called the Warburg impedance. As we can see, EIS is not just a useful tool to find the resistance, but it also helps better understand the electrochemical system.

1.6.4 Energy density and power density

Among all the characteristics, energy and power densities are the ones that most closely affect real-world applications. Therefore, they are the most evaluated parameters for supercapacitors. Figure 1.9 summarizes that energy density is related to the voltage window and capacitance, while power density is influenced by the operational voltage and ESR. More specifically, the energy and power density can be determined as[5]:

$$\mathrm{E} = \frac{1}{2}CV^2 (C\ is\ the\ capacitance\ and\ V\ is\ the\ potential\ window) \quad (1.11)$$

$$\mathrm{P} = \frac{V^2}{4\times ESR} \text{ or } \mathrm{P} = \frac{E}{t} (t\ is\ the\ discharge\ time) \quad (1.12)$$

To convert the energy density to the commonly used Wh/kg or Wh/L, the results in the equation need to be divided by 3600. In addition, the Ragone plot is a popular way to present and compare energy and power density data as Figure 1.4 displays. Since both high power and energy density are required for ideal supercapacitors, they should be located at the upper right corner of the plot.

1.7 Mass balance for supercapacitors

1.7.1 Enhance the energy density of supercapacitor by balancing the mass and capacitance of the electrodes

It is reported above that the energy density of a supercapacitor is proportional to its capacitance and the square of its voltage window. In order to improve the energy density, scientists are trying to develop new types of electrode materials and electrolytes. However, balancing the mass and capacitance of the electrodes is also of great importance to enlarge the operating potential window of supercapacitors.

According to Andres *et al.*[26], the optimal capacitance of a supercapacitor can be achieved by balancing the mass of positive and negative electrodes as Figure 1.12A shows. Especially in

cases where the sizes of hydrated cations and anions in the electrolyte are quite different, using equal mass on both electrodes will prevent the device from achieving high capacitance. As Figure 1.13B illustrates, Piñeiro-Prado *et al.*[27] tried to widen the operational window of activated carbon supercapacitors by mass balancing. The asymmetric structure (different mass on positive and negative electrodes) of the device enlarges the potential window and enhances the energy density when compared to a symmetric device.

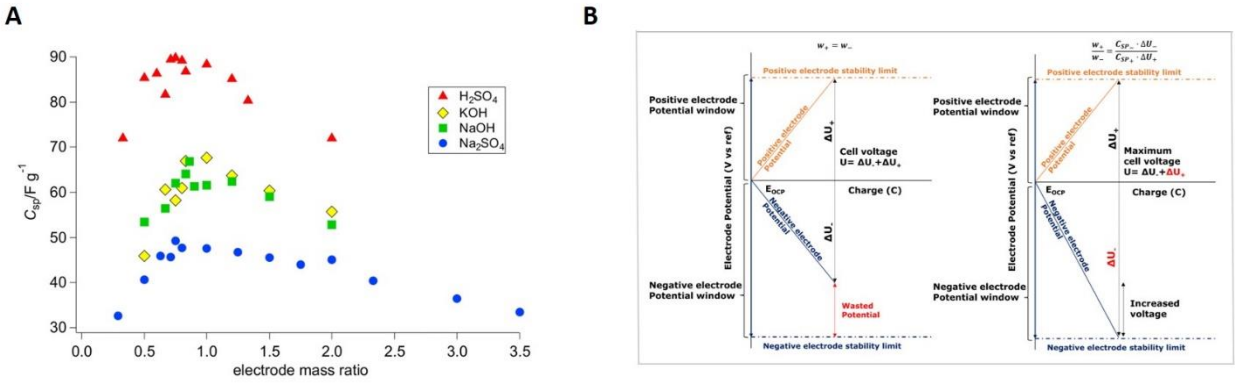

Figure 1.12 (A) Influence of electrode mass ratio on specific capacitance of supercapacitors with different aqueous electrolytes.[26] (B) Scheme of the relationship between electrode potentials, voltage, and charge in symmetric (left) and asymmetric (right) supercapacitors.[27]

1.7.2 Principle of mass and capacitance balance of the electrodes.

The principle[28] to balance capacitance and mass is:

$$m_+C_+V_+ = m_-C_-V_- \tag{1.13}$$

Where m_+ and m_- are the masses, C_+ and C_- are the specific capacitances and V_+ and V_- are the potential windows for positive and negative electrodes, respectively. We can see that the mass-balancing equation is essentially charge-balancing.

If both electrodes are made of either carbon or pseudo-capacitive materials like RuO_2, the capacitance over the whole potential window is constant and the mass ratio can be easily calculated: (1) A three-electrode set-up can be used to determine the stable operating voltage window for both electrodes. (2) The specific capacitance of the electrode materials can be evaluated through the three-electrode system as well. (3) The mass ratio of the electrodes will be:

$$\frac{m_+}{m_-} = \frac{C_- V_-}{C_+ V_+}. \tag{1.14}$$

However, when one or more electrodes contain battery-like materials such as polyaniline, Co_3O_4 or $Ni(OH)_2$, their charge storage capability cannot be described using capacitance. Capacity is used instead. In this case, the mass ratio of the electrode can be determined by:

$$\frac{m_+}{m_-} = \frac{Capacity_-}{Capacity_+}. \tag{1.15}$$

1.8 High potential supercapacitors with aqueous electrolytes

The traditional way to achieve large operation voltage is by utilizing organic electrolytes. Although this is able to enlarge the potential window from 1 V to 2.7 V, organic electrolytes are flammable and expensive which limits their applications. As a result, high voltage supercapacitors based on aqueous electrolytes have been studied in recent years to improve the energy density of the device. There are mainly two methods to realize a high operating voltage in aqueous systems. One is by design of an asymmetric cell configuration, while the other is by using a neutral electrolyte with high ion solvation energies.

An asymmetric supercapacitor is a very broad concept. It can refer to a device that employ diverse materials for the electrodes or it may also mean that the supercapacitor has different mass loading for the electrodes with the same material.[11] But asymmetric supercapacitors for high

voltage purposes are usually composed of two different materials as explained in Figure 1.13b.[29] A typical example is the MnO_2/AC supercapacitor, in which MnO_2 works in the positive potential region, while AC functions at the negative side. By combining these two different electrodes, the resulting cell is able to be charged to 2 V, much higher than the 1 V in a symmetric configuration (Figure 1.13a). While the asymmetric design has stretched the operational voltage of aqueous systems, it is not easy to fabricate. The electrochemical process in the asymmetric device is not well understood either.[30] Accordingly, a simple and reliable process to synthesize high voltage supercapacitors is still in demand.

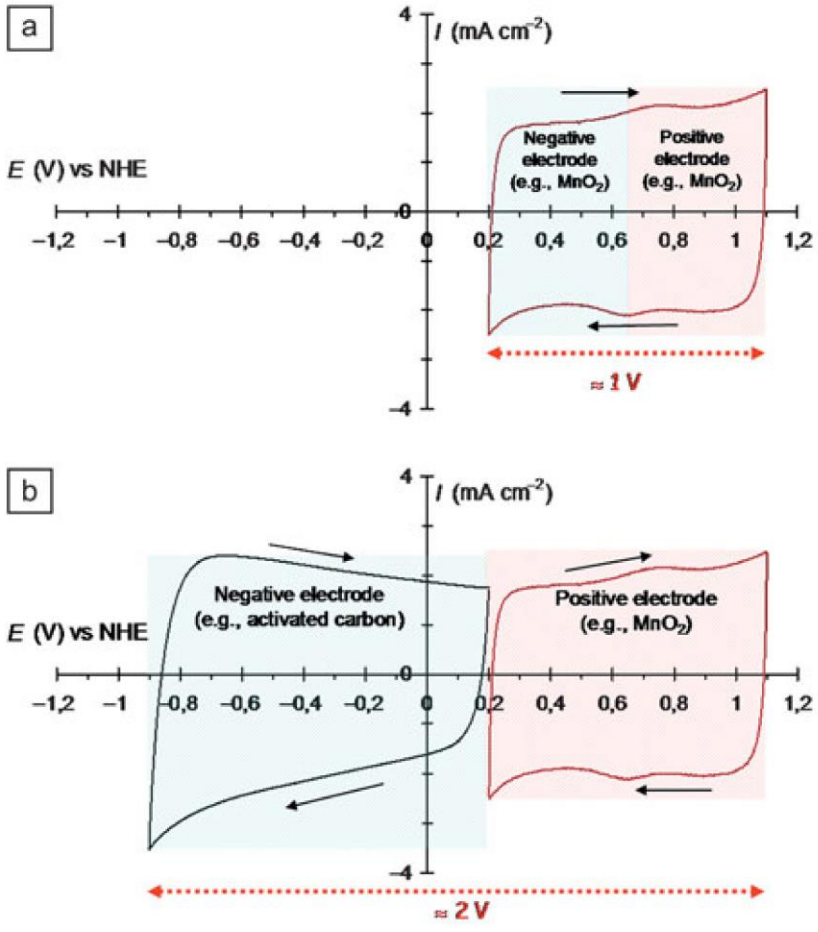

Figure 1.13 Illustration of the CV with different cell structures in which the red and blue areas are the potential windows for the positive and negative electrodes, respectively: (a) a symmetric MnO_2 supercapacitor, (b) an asymmetric device with MnO_2 and activated carbon.[29]

Another method to achieve a high voltage cell is by a judicious choice of the electrolyte. There has been a lot of research on neutral electrolytes recently because of their larger potential window, less corrosion and environmental friendliness.[31-34] Wang *et al.*[32] reported a 1.8 V device made with hierarchical porous carbon in 1 M Na_2SO_4. Gao *et al.*[33] discussed the research on a symmetric carbon supercapacitor with a large operating voltage of 1.9 V in a lithium sulfate electrolyte. Fic *et al*.[34] even expanded the potential of their aqueous device to 2.2 V using 1 M Li_2SO_4. More results are summarized in Table 4.[31] This is because the concentrations of the H^+ and OH^- ions in neutral electrolyte are lower than in acidic or basic solutions. Therefore, it is difficult for the water decomposition to take place at low voltage, enlarging the potential window. High solvation[35-36] energies for some electrolyte ions such as Li^+, Na^+ and SO_4^{2-} could also account for the large voltage window, especially for electrolytes with high concentrations. In this case, the ions have large solvation shells to break before the water can be decomposed, which increases the potential window. When compared with the asymmetric approach, this method is inexpensive and facile, and therefore promising for future applications.

Table 1.4 Supercapacitors Based on Neutral Electrolytes and Their Performance[31]

Aqueous electrolyte/ concentration	Electrode materials	Specific capacitance ($F\ g^{-1}$)	Cell voltage (V)	Energy density ($W\ h\ kg^{-1}$)	Power density ($W\ kg^{-1}$)	Temp. (°C)
Na_2SO_4/1 M	3D FHPC	—	1.8	15.9	317.5	—
$NaNO_3$/1 M	AC	116 at 2 mV s^{-1}	1.6	—	—	RT
Na_2SO_4/0.5 M	Microporous carbon	~60 at 0.2 A g^{-1}	1.8	~7	~40	—
$NaNO_3$–EG/4 M	AC	22.3 at 2 mV s^{-1} (0 °C)	2	14–16 (RT)	~500	0 to 60
Na_2SO_4/0.5 M	Seaweed carbons	123 at 0.2 A g^{-1}	1.6	10.8	—	—
Na_2SO_4/0.5 M	AC	135 at 0.2 A g^{-1}	1.6	~10	—	—
KCl/1 M	$MnCl_2$-doped PANI/SWCNTs nanocomposites	546 at 0.5 A g^{-1}	1.6	194.13	~550	RT
Li_2SO_4/1 M	AC	180 at 0.2 A g^{-1}	2.2	—	—	—
Na_2SO_4/1 M	Mesoporous MnO_2	278.8 at 1 mV s^{-1}	1	~28.4	~70	RT
Li_2SO_4/1 M	Mesoporous MnO_2	284.24 at 1 mV s^{-1}	1	~28.8	~70	RT
K_2SO_4/0.65 M	Mesoporous MnO_2	224.88 at 1 mV s^{-1}	1	~24.1 (0.5 M K_2SO_4)	~70	RT
Na_2SO_3/1 M	Well-ordered mesoporous carbon/Fe_2O_3 nanoparticle composites	235 at 0.5 A g^{-1}	1	39.4	—	RT
Na_2SO_4/0.5 M	MnO_2@carbon nanofibers composites	551 at 2 mV s^{-1} (75 °C)	0.85	—	—	0 to 75
Na_2SO_4/1 M	Hydrous RuO_2	52.66 at 0.625 A g^{-1}	1.6	18.77	500	—
Na_2SO_4/1 M	CNFs with radially grown graphene sheets	—	1.8	29.1	450	—

1.9 Applications of supercapacitors

1.9.1 Portable electronic devices

Supercapacitors can be used to supply energy for cellphones (Figure 1.14A), laptops (Figure 1.14B), small electric tools and the photographic flash (Figure 1.14C) [37] in cameras. It was reported that a lifetime flashlight ((Figure 1.14D)) was developed by 5.11 Tactical which is able to be fully charged in 90 s thanks to the high power density of a supercapacitor.[38]

Figure 1.14 Examples of consumer electronics embedded with supercapacitors (A) mobile phones, (B) cameras (C) laptops and (D) a flashlight.

1.9.2 Electric vehicles

Electrochemical capacitors are also utilized in transportation. The Yaris Hybrid-R concept car (Figure 1.15A) launched by Toyota uses a supercapacitor to deliver impulse power. Germany manufactured the first "ultracapbus" in 2001, which integrates supercapacitors with a diesel-electric drive (Figure 1.15C). Most interestingly, supercapacitors are embedded to provide energy for aerial lifts (Figure 1.15B).[37] Since cable cars are operated without stopping, the only chance to get recharged is when the vehicle arrives at the station to load and unload passengers. The time is too short to fully charge a battery, but sufficient for a supercapacitor because of its fast charging/discharging capabilities.

Figure 1.15 Applications of supercapacitors in (A) electric cars, (B) gondolas and (C) buses.

1.9.3 Power buffer

Another application of supercapacitors is to provide emergency energy for devices. Most random-access memory (RAM) and static random-access memory (SRAM) are volatile as Figure 1.16A and 1.16B show, which means the data will be lost if they lose their power supply. By connecting

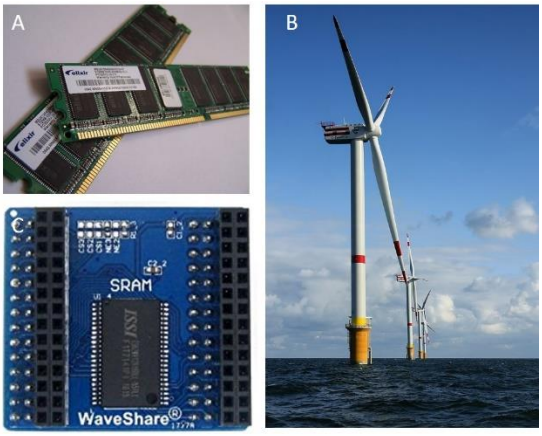

Figure 1.16 (A) Random-access memory (RAM), (B) wind turbine pitch and (C) static random-access memory (SRAM)

to a supercapacitor, the memories can still be powered during shutdown. The same idea is used for wind turbine pitch systems. A supercapacitor is integrated into the system so that the blades can be adjusted even when the major power dies.

1.9.4 Energy recovery

Another important application for supercapacitors is to recover the braking energy for vehicles. A typical example is the Mazda i-ELOOP[39] system which utilizes an alternator to generate electricity from the rotation of the wheels when the car is breaking. This portion of the energy will be stored in the supercapacitors and reused when the car is accelerating. By using the regenerative braking system, the energy is used more efficiently, leading to better fuel economy.

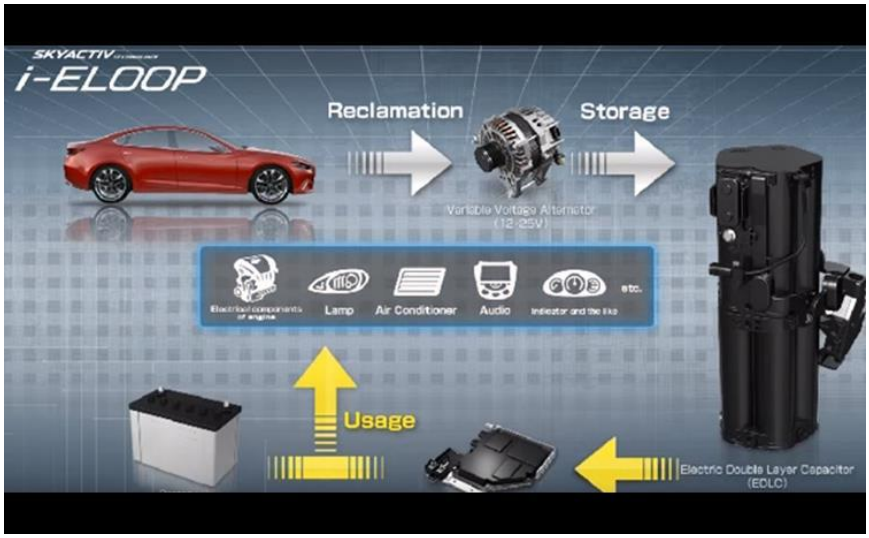

Figure 1.17 Scheme of the regenerative braking system for Mazda.

1.9.5 Self-powered unites by combination of energy harvesting devices

Moreover, supercapacitors can be combined with energy harvesting systems to become self-powered units. Figure 1.18A illustrates the idea to generate electricity by a revolving door. The energy is stored in the supercapacitor and is used to power the electronic components in the building. Figure 1.18B is a self-powered system composed of a solar cell and a supercapacitor. The solar cell harvests energy from sunlight and stores it in the electrochemical capacitor. The stored energy can be used for illumination at night. In addition, nanogenerators based on piezoelectric materials are integrated with a supercapacitor to create a self-powered unit (Figure 1.18C).

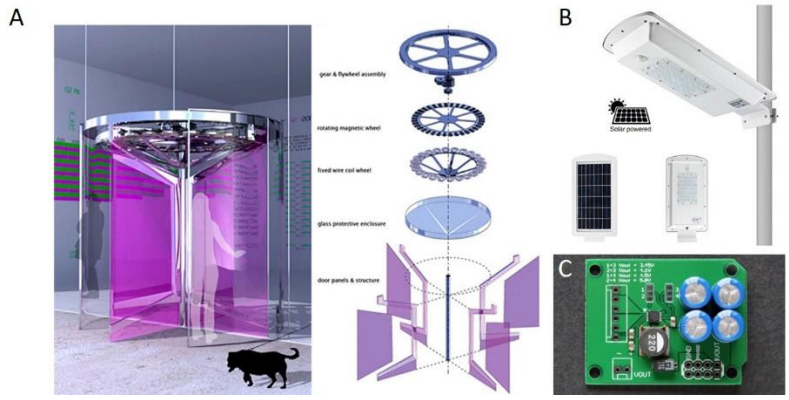

Figure 1.18 (A) A self-powered system in which a revolving door generates energy for storage in supercapacitors, (B) lights based on a solar cell/supercapacitor combination and (C) self-charging supercapacitors powered by piezoelectric materials.

1.10 Structure of the thesis

Chapter 1 is an introduction of the background information for supercapacitors, the trend to enhance their performance and applications. It also explains the purpose of the thesis as to develop more reliable energy storage devices.

Chapter 2 demonstrates the facile fabrication of a hollow Co_3O_4/LSG composite material. The unique hollow structure of the metal oxide not only provides a large number of active sites for redox reaction, but it also reduces the ion diffusion length and improves the material's utility efficiency. Thanks to the synergetic effect between the cobalt oxide and the carbon material, the hybrid material exhibits good capacity (60.0 C/cm^3), low resistance (0.9 Ω) and long cycle life (113.1% capacity retention after 10,000 cycles).

Chapter 3 shows the possibility of building a high-voltage aqueous symmetric supercapacitor using commercial activated carbon and an $Fe(CN)_6^{3-}/Fe(CN)_6^{4-}$ redox electrolyte. A laser scribing process is also performed on the thick AC electrodes to improve the ion diffusion

process, increasing its capacitance. Since energy density and power density are related to the operational voltage and capacitance, our supercapacitor is able to store 9 times more energy than commercial AC cells, which is promising for real world applications.

Chapter 4 presents the work of a self-charging power unit by a combination of a porous PVDF separator and polyaniline electrodes. This kind of device is attractive due to its capability to harvest energy from the ambient environment. The pore size and pore volume of the PVDF film is optimized by a judicous choice of the sacrificial template. Because PVDF is piezoelectric, there will be potential difference on its two faces when deformation is applied, which charges the supercapacitor spontaneously. Our device is able to go over 0.2 V with simple palm impact.

Chapter 5 introduces another self-powered device by the combination of a Si based solar cell and an LSG supercapacitor. In this way, solar energy can be converted into electricity and stored for future use in the energy storage device. The merits of this work is it integrates two separate devices into a single cell, which fits the needs for portable and lightweight power units. The total efficiency of the device is 2.92%.

Chapter 6 concludes all the work in this thesis and discusses possible future work to improve the performance of state-of-the-art supercapacitors.

1.11 References

(1) https://www.worldenergy.org/wp-content/uploads/2017/04/1.-World-Energy-Issues-Monitor-2017-Full-Report.pdf

(2) http://www.bp.com/en/global/corporate/energy-economics/statistical-review-of-world-energy/primary-energy.html

(3) Winter, M.; Brodd, R.J. What are batteries, fuel cells, and supercapacitors? *Chem. Rev.* **2004**, *104*, 4245−4269.

(4) Simon, P.; Gogotsi, Y.; Dunn, B. Where do batteries end and supercapacitors begin? *Science*, **2014**, *343*, 1210-1211.

(5) Conway, B. E. *Electrochemical supercapacitors: scientific fundamentals and technological applications*; Springer Science & Business Media: New York, 2013.

(6) Burke, Andrew. R&D considerations for the performance and application of electrochemical capacitors. *Electrochim. Acta*, **2007**, *53*, 1083-1091.

(7) Simon, P.; Gogotsi, Y. Materials for electrochemical capacitors. *Nat. Mater.* **2008**, *7*, 845-854.

(8) Miller, J.R.; Simon, P. Fundamentals of electrochemical capacitor design and operation. *Electrochem. Soc. Interface*, **2008**, *17*, 31-32.

(9) Zhang, L.L.; Zhao, X.S. Carbon-based materials as supercapacitor electrodes. *Chem. Soc. Rev.* **2009**, *38*, 2520-2531.

(10) Largeot, C.; Portet, C.; Chmiola, J.; Taberna, P.L.; Gogotsi, Y.; Simon, P. Relation between the ion size and pore size for an electric double-layer capacitor. *J. Am. Chem. Soc.* **2008**, *130*, 2730-2731.

(11) Brousse, T.; Bélanger, D.; Long, J.W. To be or not to be pseudocapacitive? *J. Electrochem. Soc.* **2015**, *162*, 5185-A5189.

(12) Jost, K.; Dion, G.; Gogotsi, Y. Textile energy storage in perspective. *J. Mater. Chem. A*, **2014**, *2*, 10776-10787.

(13) Zhi, M.; Xiang, C.; Li, J.; Li, M.; Wu, N. Nanostructured carbon–metal oxide composite electrodes for supercapacitors: a review. *Nanoscale*, **2013**, *5*, 72-88.

(14) Peigney, A.; Laurent, C.; Flahaut, E.; Bacsa, R.R.; Rousset, A. Specific surface area of carbon nanotubes and bundles of carbon nanotubes. *Carbon*, **2001**, *39*, 507-514.

(15) Zhu, Y.; Murali, S.; Stoller, M.D.; Ganesh, K.J.; Cai, W.; Ferreira, P.J.; Pirkle, A.; Wallace, R.M.; Cychosz, K.A.; Thommes, M.; Su, D. Carbon-based supercapacitors produced by activation of graphene. *Science*, **2011**, *332*, 1537-1541.

(16) Gogotsi, Y.; Simon, P. True performance metrics in electrochemical energy storage. *Science*, **2011**, *334*, 917-918.

(17) Snook, G.A.; Kao, P.; Best, A.S. Conducting-polymer-based supercapacitor devices and electrodes. *J. Power Sources*, **2011**, *196*, 1-12.

(18) Zhang, S.; Pan, N. Supercapacitors performance evaluation. *Adv. Energy Mater*. **2015**, *5*, 1401401.

(19) Kim, J.W.; Augustyn, V.; Dunn, B. The effect of crystallinity on the rapid pseudocapacitive response of Nb_2O_5. *Adv. Energy Mater.* **2012**, *2*, 141-148.

(20) Miller, J.R.; Outlaw, R.A.; Holloway, B.C. Graphene double-layer capacitor with ac line-filtering performance. *Science*, **2010**, *329*, 1637-1639.

(21) Yu, M.; Wang, Z.; Han, Y.; Tong, Y.; Lu, X.; Yang, S. Recent progress in the development of anodes for asymmetric supercapacitors. *J. Mater. Chem. A*, **2016**, *4*, 4634-4658.

(22) Béguin, F.; Presser, V.; Balducci, A.; Frackowiak, E. Carbons and electrolytes for advanced supercapacitors. *Adv. Mater.* **2014**, *26*, 2219-2251.

(23) Lu, W.; Qu, L.; Henry, K.; Dai, L. High performance electrochemical capacitors from aligned carbon nanotube electrodes and ionic liquid electrolytes. *J. Power Sources*, **2009**, *189*, 1270-1277.

(24) Omanda, H.; Brousse, T.; Marhic, C.; Schleich, D.M. Improvement of the thermal stability of $LiNi_{0.8}Co_{0.2}O_2$ cathode by a SiO_x protective coating. *J. Electrochem. Soc.* **2004**, *151*, A922-A929.

(25) Burke, A.; Miller, M. Testing of electrochemical capacitors: Capacitance, resistance, energy density, and power capability. *Electrochim. Acta*, **2010**, *55*, 7538-7548.

(26) Andres, B.; Engström, A.C.; Blomquist, N.; Forsberg, S.; Dahlström, C.; Olin, H. Electrode mass balancing as an inexpensive and simple method to increase the capacitance of electric double-layer capacitors. *PloS one* **2016**, *11*, e0163146.

(27) Piñeiro-Prado, I.; Salinas-Torres, D.; Ruiz-Rosas, R.; Morallón, E.; Cazorla-Amorós, D. Design of activated carbon/activated carbon asymmetric capacitors. *Frontiers in Mater.* **2016**, *3*, 16.

(28) Zhang, J.; Zhao, X.S. On the configuration of supercapacitors for maximizing electrochemical performance. *ChemSusChem*, **2012**, *5*, 818-841.

(29) Long, J.W.; Belanger, D.; Brousse, T.; Sugimoto, W.; Sassin, M.B.; Crosnier, O. Asymmetric electrochemical capacitors—Stretching the limits of aqueous electrolytes. *MRS Bull*. **2011**, *36*, 513-522.

(30) Wang, F.; Xiao, S.; Hou, Y.; Hu, C.; Liu, L.; Wu, Y. Electrode materials for aqueous asymmetric supercapacitors. *RSC Adv*. **2013**, *3*, 13059-13084.

(31) Zhong, C.; Deng, Y.; Hu, W.; Qiao, J.; Zhang, L.; Zhang, J. A review of electrolyte materials and compositions for electrochemical supercapacitors. *Chem. Soc. Rev*. **2015**, *44*, 7484-7539.

(32) Wang, Q.; Yan, J.; Wang, Y.; Wei, T.; Zhang, M.; Jing, X.; Fan, Z. Three-dimensional flower-like and hierarchical porous carbon materials as high-rate performance electrodes for supercapacitors. *Carbon*, **2014**, *67*, 119-127.

(33) Gao, Q.; Demarconnay, L.; Raymundo-Piñero, E.; Béguin, F. Exploring the large voltage range of carbon/carbon supercapacitors in aqueous lithium sulfate electrolyte. *Energy Environ. Sci*. **2012**, *5*, 9611-9617.

(34) Fic, K.; Lota, G.; Meller, M.; Frackowiak, E. Novel insight into neutral medium as electrolyte for high-voltage supercapacitors. *Energy Environ. Sci*. **2012**, *5*, 5842-5850.

(35) Kelly, C.P.; Cramer, C.J.; Truhlar, D.G. Aqueous solvation free energies of ions and ion−water clusters based on an accurate value for the absolute aqueous solvation free energy of the proton. *J. Phys. Chem. B*, **2006**, *110*, 16066-16081.

(36) Yang, L.; Fan, Y.; Gao, Y.Q. Differences of cations and anions: Their hydration, surface adsorption, and impact on water dynamics. *J. Phys. Chem. B*, **2011**, *115*, 12456-12465.

(37) https://en.wikipedia.org/wiki/Supercapacitor

(38) https://www.511tactical.com/accessories/flashlights.html

(39) http://www.mazda.com/en/innovation/technology/env/i-eloop/

CHAPTER 2

Embedding Hollow Co_3O_4 Nanoboxes into a 3D Macroporous Graphene Framework for High-Performance Supercapacitors

2.1 Abstract

Carbon materials are widely used for supercapacitor applications thanks to their high surface area, good rate capability and excellent cycling stability. However, the development of high energy density carbon supercapacitors still remains a challenge. In this work, hollow Co_3O_4 nanoboxes have been embedded into 3D macroporous laser scribed graphene (LSG) to produce composite electrodes with improved electrochemical performance. Here, Co_3O_4 provides high capacity through fast and reversible redox reactions, while LSG serves as a conductive network to maintain high power. The open nanobox morphology is a unique solution for extracting the maximum capacity from Co_3O_4, resulting in electrodes whose surfaces, both internal and external, are accessible to the electrolyte. The electrochemical performance of the composite material is promising with a volumetric capacity of 60.0 C/cm^3 and a specific capacity of 542.3 C/g, corresponding to 682.0 C/g of the constituent Co_3O_4. With a low equivalent series resistance (ESR) of 0.9 Ω, the Co_3O_4/LSG electrode is able to maintain 113.1% of its original capacity after 10,000 cycles. This work provides new insights into the design of high-performance carbon/metal oxide nanocomposites as an effective approach for the next-generation of high-energy energy storage devices.

2.2 Introduction

Rapid improvements in consumer electronics and electric vehicles drive the need for reliable energy storage systems with enhanced energy density and power density. Because of their excellent electrochemical properties, supercapacitors have been recognized as one of the most promising energy storage systems. They exhibit intermediate properties between those of traditional capacitors and chemical batteries[1]. In addition, they are likely to play an important role in the future of energy storage thanks to their high power density, long cycle life and ability to work at low temperatures[2]. These characteristics make supercapacitors the technology of choice for consumer electronics, backup power and regenerative braking. In addition, battery/supercapacitor combinations are now under investigation as promising power sources for electric vehicles[1,3,4].

There are two main types of supercapacitors distinguished by their charge storage mechanism[5]. The first, called an electric double-layer capacitor (EDLC), stores energy electrostatically through adsorption of electrolyte ions on the electrode surfaces. The second type of supercapacitor is composed of pseudo-capacitive or battery-like materials. Energy is stored via fast and reversible redox reactions occurring primarily on their surfaces. Following recommendations from Brousse *et al*[6], one needs to distinguish between normal pseudo-capacitive materials and battery-like materials. According to Brousse *et al.*[6] the term pseudo-capacitive can only be used when the redox active material has the electrochemical signature of a capacitive carbon electrode. A typical example under this category is ruthenium oxide, whose rectangular CV profile over a large voltage window is the origin of the term pseudo-capacitance. Other metal oxides/hydroxides showing clear redox peaks during charge and discharge can no

longer be described as pseudo-capacitors, but instead they have characteristics similar to those of batteries. To put things in perspective, capacity in Coulombs per gram (C/g) should be used instead of capacitance Farads per gram (F/g) for the evaluation of the performance of such battery-like electrodes.

Carbon materials with large specific surface areas, such as activated carbons, carbon nanotubes and graphene, are normally used in EDLCs[7]. Their high surface area provides a large number of sites for charge storage through ion adsorption. The surface area of the carbon materials can be further optimized by introducing well-aligned pore structures with methods that include templating and chemical etching[8]. Among all the carbon materials, graphene has shown the greatest promise because of its excellent electrical conductivity, good mechanical properties and extraordinary high surface area[9-11]. While graphene supercapacitors have demonstrated excellent electrochemical properties, practical applications of carbon materials are still limited by their relatively low energy density. On the other hand, pseudo-capacitive and battery-like materials can exhibit up to ten times higher capacity than carbonaceous materials thanks to energy dense Faradaic reactions. Typical electrode materials for the second type of supercapacitor consist of metal oxides and nitrides[12-15,39,40] and conducting polymers[16] or combinations thereof. Because of its high theoretical capacity, Co_3O_4 is a very attractive material for energy storage. In addition, it is promising for mass production due to its abundance and low cost. However, like most other metal oxides, Co_3O_4 suffers from low electronic conductivity and limited stability, losing its capacity rapidly upon cycling.

In order to improve the electrochemical performance of metal oxides, morphology control and pore size design is of paramount importance. A rationally controlled structure may facilitate

ion diffusion and improve the mechanical properties of the material and, therefore, its energy efficiency. A number of research groups have synthesized Co_3O_4 with different nanostructures, such as nanowires[17], nanotubes[18], nanobelts[19], nanoneedles[20], nanorods[21] and hollow nanoparticles[22]. Synthesis of layered Co_3O_4 by chemical exfoliation is also reported to enhance its surface area and improve ion diffusion[8,23]. Among these, the hollow nanoparticle architecture is most desirable for supercapacitor applications. The hollow structure not only provides an outside surface for charge storage, but also makes the inner surface accessible, resulting in more active sites for redox reactions. In addition, the hollow structure lowers the diffusion length of ions and improves the power density of the system. Moreover, less dead mass will be involved and the materials will be more effectively used. Representative methods for fabrication of hollow Co_3O_4 includes hard templates[24], soft templates[25], the nanoscale Kirkendall effect[22], and Ostwald ripening methods[26].

Although the structure of Co_3O_4 can be tailored with high precision, its low conductivity of 10^{-4} to 10^{-2} S/cm[13] hinders Co_3O_4 from approaching its theoretical capacity. Besides, the poor mechanical properties of metal oxides makes them prone to degradation during repeated charging and discharging. To overcome these drawbacks, metal oxides are often combined with carbon nanomaterials to form new composite electrodes with chemical and physical properties that are distinct from their individual components[27-28,41]. In these composites, carbon provides a conductive network, allowing fast electron transport and high power output, while the metal oxide boosts the energy density of the entire system thanks to its high specific capacity. Previous work from our group shows that the laser scribing of graphite oxide (GO) films results in 3D macroporous graphene electrodes, called laser scribed graphene (LSG)[9]. The LSG exhibits an excellent electrical conductivity of more than 1700 S/m and a large surface area in excess of 1500 m^2/g.

These features make LSG an ideal candidate for the fabrication of metal oxide/carbon composite electrodes.

Inspired by these features, we developed a hybrid system comprising hollow Co_3O_4 nanoboxes and LSG macroporous electrodes. Here, the hollow Co_3O_4 nanoboxes are produced by using the nanoscale Kirkendall effect[22], which involves low temperature recrystallization of cobalt acetate followed by slow calcination. These hollow Co_3O_4 structures are embedded into the LSG framework by mixing the metal oxide with graphite oxide and converting the composite into Co_3O_4/LSG via a laser scribing technique as shown in Figure 2.1. A high specific surface area of 357 m^2/g was measured for the composite material. In such a porous structure, the LSG performs as a three-dimensional conductive scaffold for the metal oxide, expediting electron transport via lowering the ESR to <1 Ω. The LSG also functions as a 3D matrix over which the metal oxide is anchored, allowing for improved electrochemical properties of Co_3O_4 and preventing the nanoboxes from aggregating. The Co_3O_4 not only makes up for the relatively low capacity of LSG, but also offers more active sites for redox reactions, leading to electrodes with both enhanced energy and power density. With the synergistic effects between the metal oxide and LSG, an areal capacity of 60.0 mC/cm^2 is reached, which is 8 times higher than pure LSG. These features make hollow Co_3O_4/LSG a promising candidate for the next generation of high-performance energy storage electrodes. This work also provides new insights into our understanding of the properties of metal oxides and lays down new strategies for designing improved metal oxide-based energy storage devices.

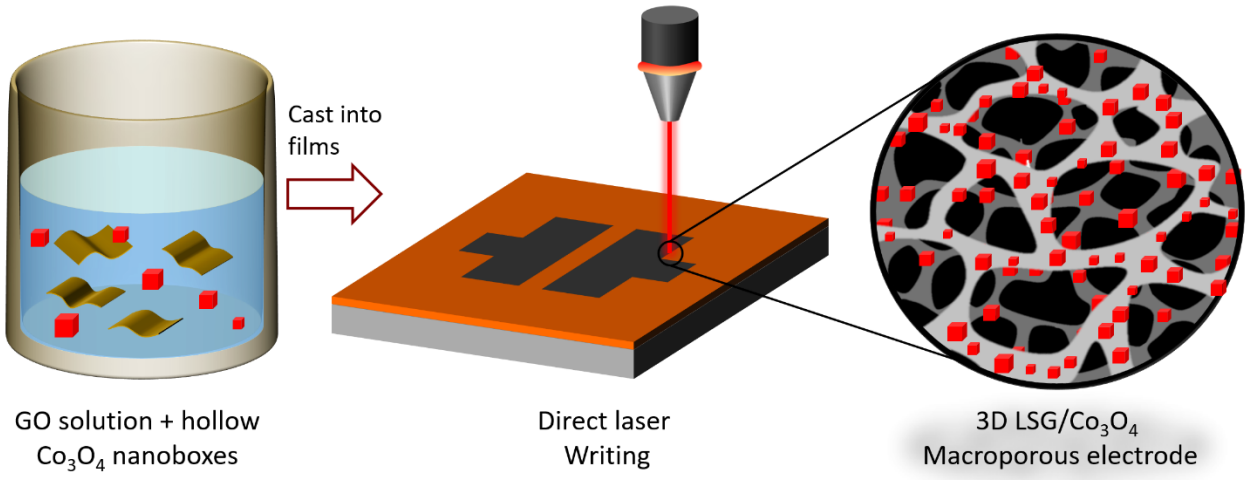

Figure 2.1 Fabrication of hollow Co_3O_4/LSG composite electrodes. First, cobalt oxide nanoboxes are made with a combination of recrystallization and calcination steps. The as-prepared Co_3O_4 boxes are mixed with GO, coated onto a substrate, and then scribed with a CO_2 laser to produce the Co_3O_4/LSG composite, which is confirmed by a color change from light gray to black. The resulting electrode features a 3D graphene matrix with high surface area where the Co_3O_4 nanoboxes are uniformly anchored to its surface, allowing for efficient charge storage.

2.3 Experimental

2.3.1 Preparation of Hollow Co_3O_4 nanoboxes

In a typical experiment, 0.8 g of $Co(CH_3COO)_2 \cdot 4H_2O$ is dissolved in 500 mL[22] of cold ethanol and the solution is kept at -5 ºC. After several weeks, the precipitate is collected and washed with ethanol by centrifugation, followed by drying overnight in a vacuum oven. The powder is then heated to 300 ºC at the rate of 1 ºC per minute and calcinated for 10 minutes to complete the conversion to Co_3O_4.

2.3.2 Synthesis of the hollow Co_3O_4/LSG composite

The as-prepared Co_3O_4 nanoboxes are mixed with freeze-dried GO and water, stirred and sonicated. This forms a homogeneous solution, which is then drop-cast onto stainless steel substrates and dried overnight. A CO_2 laser (Full spectrum laser, MLE-40, 10.6 μm) is used to scribe the film, turning it from light gray Co_3O_4/GO to black Co_3O_4/LSG (Figure 2.2).

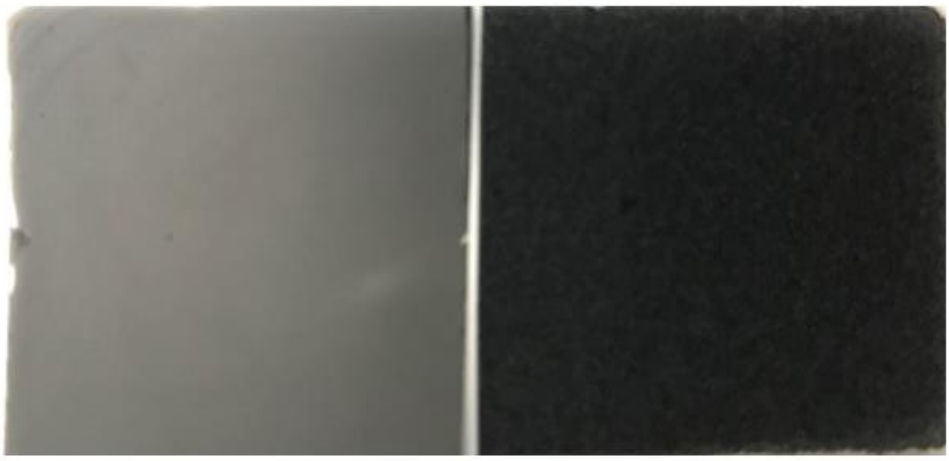

Figure 2.2 Images comparing the as-prepared Co_3O_4/GO and Co_3O_4/LSG after laser scribing. As the picture shows, the GO/metal oxide mixture exhibits a light gray color, while the Co_3O_4/LSG composite is black, indicating the reduction of GO to LSG after laser scribing.

2.3.3 Fabrication of the commercial Co_3O_4/LSG composite

The same ratio of the commercial Co_3O_4 is mixed with freeze-dried GO and water, stirred and sonicated. The drop-casting and laser scribing procedure as described above is then used to make the commercial Co_3O_4/LSG composite.

2.3.4 Electrochemical measurements

A three-electrode system was used to evaluate the performance of the Co_3O_4, the LSG and the Co_3O_4/LSG composite materials. In this system, platinum foil functions as the counter electrode, a Hg/HgO electrode as the reference electrode and a 6.0 M KOH solution is used as the electrolyte. The electrochemical performance was evaluated by cyclic voltammetry (CV), galvanostatic charge/discharge cycles and electrochemical impedance spectroscopy (EIS) using a Biologic VMP3 electrochemical workstation. The Co_3O_4/LSG films were cut into 0.5 cm × 0.5 cm squares and made into electrodes by connecting with copper tape and passivated with 5-minute epoxy (Devcon).

2.3.5 Characterization

The morphology of both metal oxide and composite films were studied using a field emission scanning electron microscope (FESEM, JEOL JSM-6700F FE-SEM) and a transmission electron microscope (TEM, T12 Quick CryoEM and CryoET (FEI)). The crystalline nature of the materials was further characterized by X-ray diffraction (XRD, Bruker DUO Apexll CCD-single crystal X-ray Diffractometer). Elemental analysis was carried out using X-ray photoelectron spectroscopy (XPS, Kratos Axis Ultra DLD spectrometer). The surface area of the composite material was analyzed using the methylene blue absorption method and the absorbance was measured by UV-vis spectroscopy (Shimadzu UV/Vis/NIR spectrophotometer, UV-3101PC).

2.4 Results and discussion

2.4.1 Fabrication of hollow Co_3O_4/LSG composites

The Co_3O_4 nanoboxes are fabricated in a two-step process, in which cobalt acetate is recrystallized in cold ethanol followed by calcination at a slow rate. The hollow structure is obtained as a result of the difference in the diffusion rates of C, H and Co atoms from cobalt acetate

during the slow heating process, a phenomenon known as the nanoscale Kirkendall effect[29]. The process can be described as follows, the C, H and Co on the surface are oxidized to form a layer of Co_3O_4. At the same time, the C, H and Co from the inside will constantly diffuse to the surface and react with oxygen, continuously forming cavities and eventually leading to the formation of the hollow Co_3O_4 structure. In order to fabricate the electrodes, a homogeneous solution of Co_3O_4 and graphite oxide is made by stirring and sonicating an equal amount (w/w) of metal oxide and freeze-dried GO in DI water. The solution is coated onto stainless steel foil and allowed to dry overnight under ambient conditions. Next, laser irradiation of the coated Co_3O_4/GO films using a CO_2 laser table (10.6 μm) running at a power of 6 Watts is applied. The laser triggers the deoxygenation of GO in the composite through a photothermal process. This is manifested by a change in the color of the composite film from light gray to gray-black, indicating the successful transition from Co_3O_4/GO to a Co_3O_4/LSG nanocomposite.

2.4.2 Characterization of hollow Co_3O_4 nanoboxes and Co_3O_4/LSG composite electrodes

The crystal structure of the Co_3O_4 nanoboxes was investigated using X-ray powder diffraction. As Figure 2.3a shows, the XRD pattern has major peaks positioned at 2θ = 19.0, 31.3, 36.9, 38.6, 44.8, 59.4, and 65.3 degrees, which matches well with the Co_3O_4 cubic spinel structure (JCPDS card no. 42-1467)[18]. This confirms the successful oxidation of cobalt acetate to Co_3O_4 during calcination. X-ray patterns of Co_3O_4/LSG nanocomposites show the same peaks, while maintaining the same position and intensity ratio except for a broad peak around 25 degrees, which indicates the formation of graphene. The similarity in the XRD patterns for the metal oxide and the composite indicates that the metal oxide material remains as Co_3O_4 after laser processing.

X-ray photoelectron spectroscopy (XPS) of both the metal oxide and the composite provide additional confirmation of the production of the desired materials. As shown in Figure 2.3b, both samples exhibit XPS peaks at 779.7 eV for Co $2p_{3/2}$ and 794.7 eV for Co $2p_{1/2}$, which is consistent with literature values[30] and confirms the existence of Co_3O_4 in both samples. In the composite material, metal oxide nanoboxes are embedded into LSG, causing a much weaker signal for the Co 2p peaks. In addition, Figure 2.3c shows photoemission peaks at 284.6 eV and 284.2 eV, corresponding to the carbon in LSG and ambient CO_2, respectively. When compared with the C1s spectra of Co_3O_4/GO (Figure 2.4), the LSG exhibit no apparent peaks for oxygen containing groups, confirming the conversion from GO to graphene. Furthermore, the O 1s peaks in the metal oxide sample appear at binding energies of 529.9 eV and 531.5 eV (Figure 2.3d), in good agreement with the literature values for Co_3O_4[30]. The broad emission peak of the composite at 532.3 eV is related to the oxygen functional groups remaining in the LSG network, overriding the signal from the metal oxide oxygen. Raman spectra were also collected for LSG and the composite materials, which both show typical peaks for graphene (Figure 2.5). The D:G ratio is between 1.4 to 1.6, indicating that the samples are rich in edges[31].

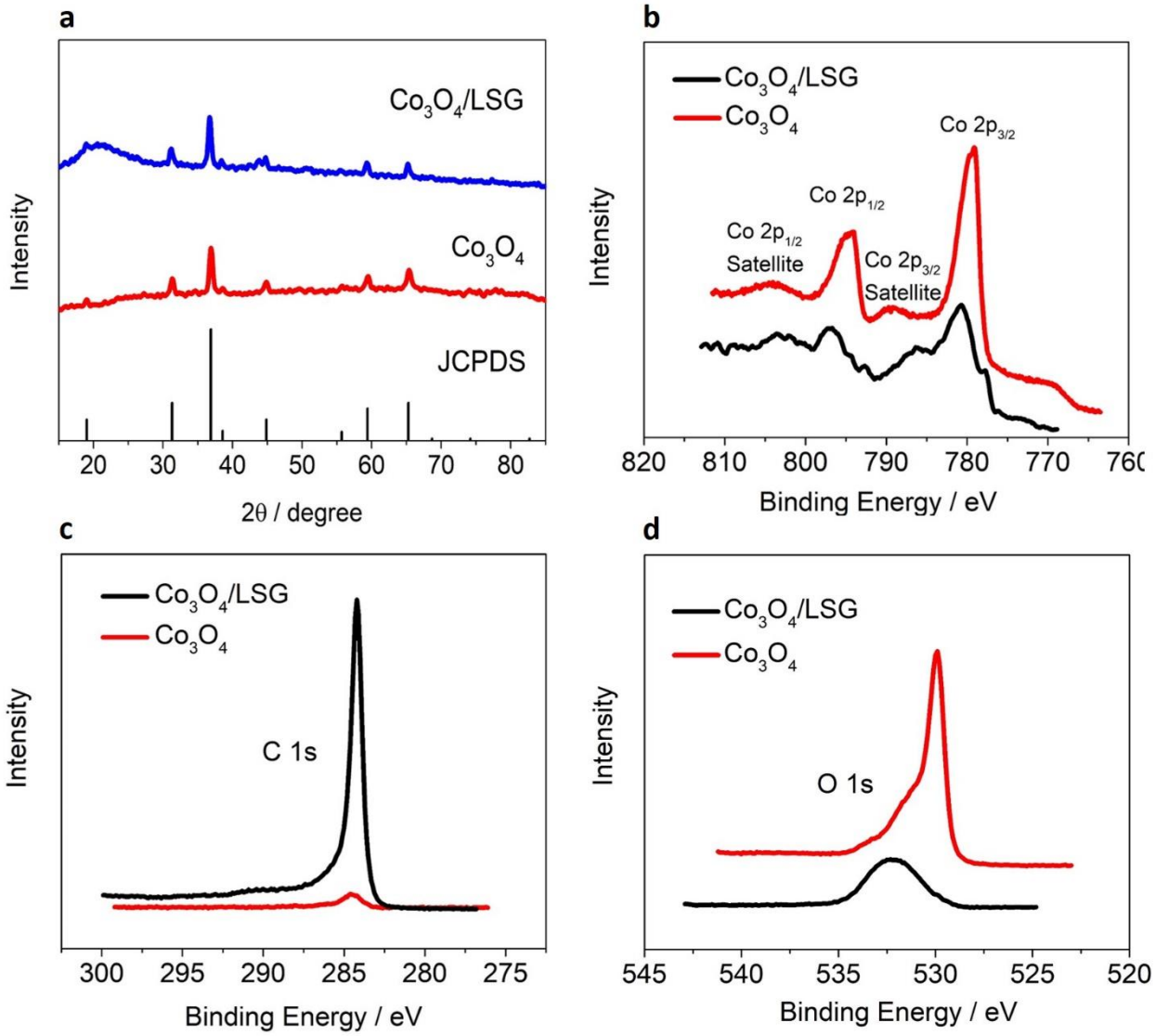

Figure 2.3 (a) XRD patterns of the as-prepared hollow Co_3O_4 and Co_3O_4/LSG compared with the Joint Committee on Powder Diffraction Standards (JCPDS) pattern, confirming the material is Co_3O_4 with a cubic spinel structure. (b) Co 2p spectra confirm that Co is in both the metal oxide and the composite. (c) C 1s indicates the presence of carbon (as LSG) in the composite. (d) O 1s spectra of Co_3O_4 and Co_3O_4/LSG.

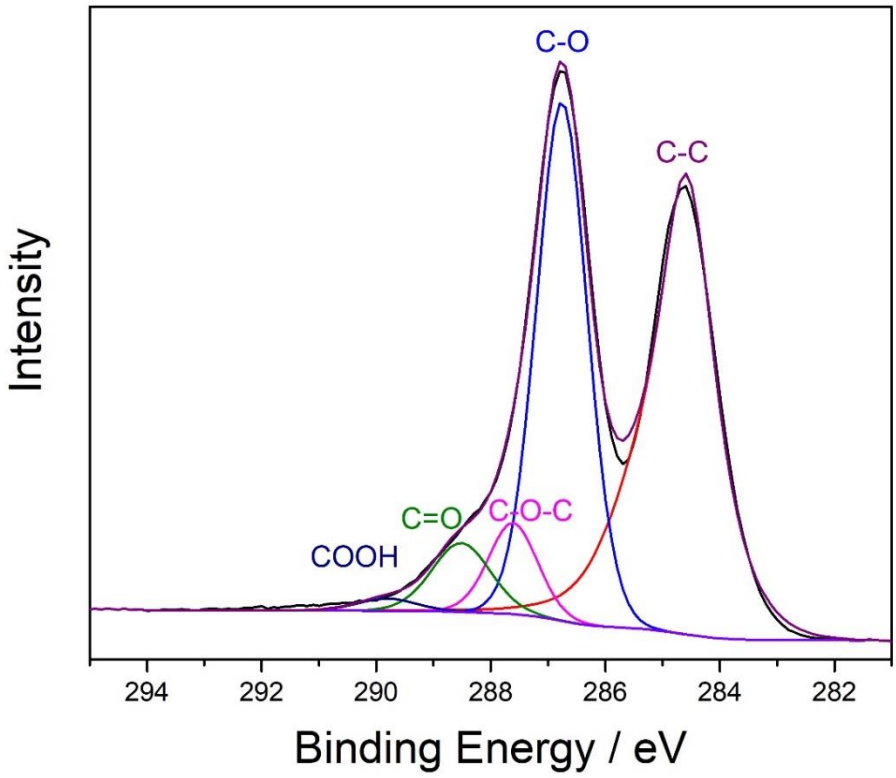

Figure 2.4 C 1s spectra of the Co_3O_4/GO show oxygen containing groups before laser treatment.

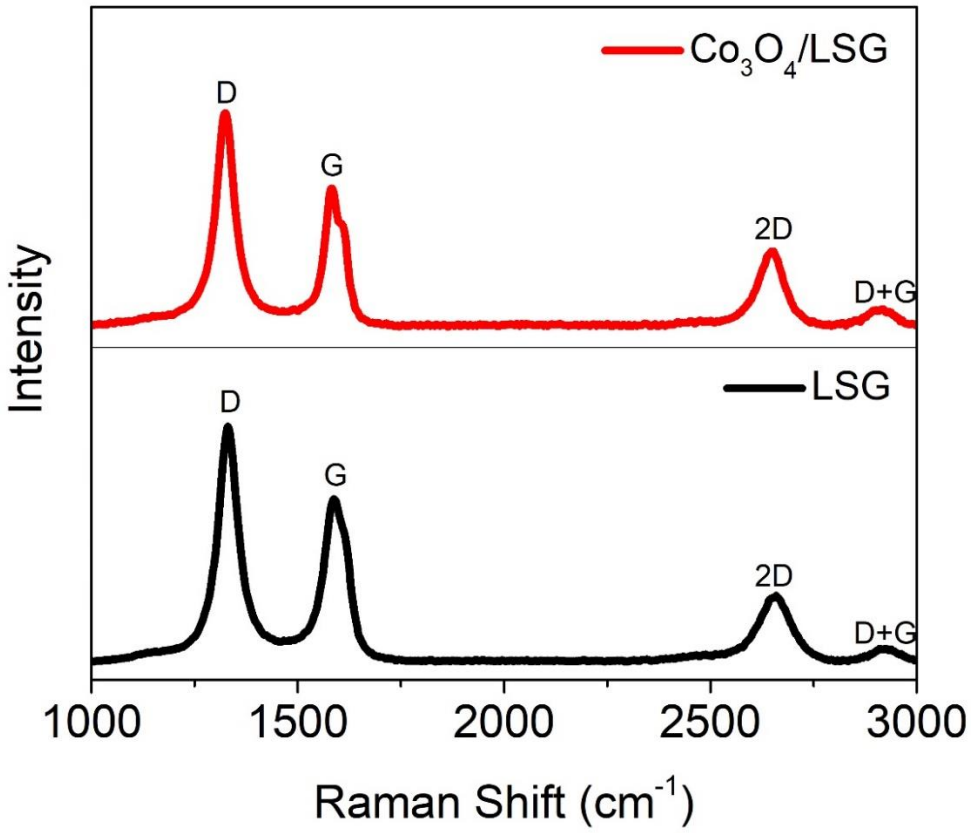

Figure 2.5 Raman spectra of Co_3O_4/LSG and pure LSG. It shows almost identical peaks for both samples, indicating the electronic structure of graphene does not change by the addition of Co_3O_4. The D: G ratios are 1.54 and 1.44 respectively, confirming the porous structure of the LSG which is rich in edges known to be beneficial for charge transfer.

To confirm the unique structure of the Co_3O_4, transmission electron microscopy (TEM) was used. The TEM image in Figure 2.6a reveals the distinct hollow nature of the as-prepared Co_3O_4, with particle sizes ranging from a hundred to a few hundred nanometers. The morphology of the metal oxide nanoboxes was further investigated by scanning electron

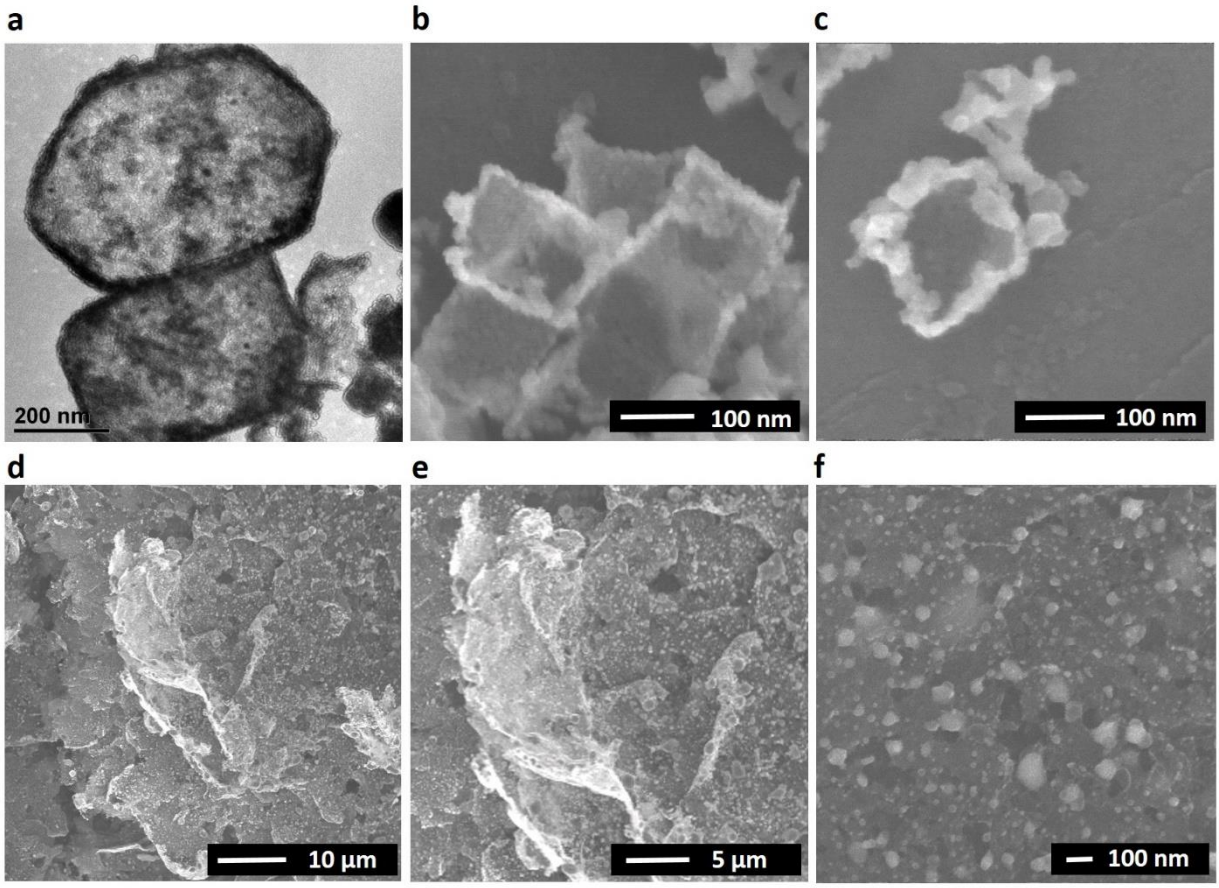

Figure 2.6 Electron Microscope images of Co_3O_4 nanoboxes and the Co_3O_4/LSG composite. (a) A TEM image shows the hollow structure of the Co_3O_4 nanoboxes. (b), (c) SEM images confirm the morphology of the nanoboxes and that they are hollow. (d-f) SEM images of the Co_3O_4/LSG composite indicate that the metal oxide is homogeneously dispersed in the LSG framework.

microscopy (SEM). As shown in Figure 2.6b,c, the vacancy inside the nanoboxes is clearly displayed through an open end. Benefiting from the hollow structure of the Co_3O_4, the materials will have more surface area for redox reactions, fast ion diffusion and a decreased amount of useless dead mass. Figure 2.6d-f indicate that embedding Co_3O_4 into an LSG electrode results in the uniform distribution of the nanoboxes in the graphene matrix with the box shape maintained

after the process of laser scribing. Graphene serves as a large flexible carpet over which the metal oxide nanoboxes can be anchored to form a stable matrix with no sign of metal oxide aggregation, preserving the surface area of the hollow Co_3O_4. The surface area is further enhanced by the intrinsic ultrahigh surface area of the LSG structure. Additionally, this carbon scaffold serves as a conductive holder for the metal oxide, providing superhighways for electrons and enabling fast charge transfer. Furthermore, the porous nature of the composite electrode provides tunnels for fast ion diffusion, which will improve the power output of the system.

2.4.3 Electrochemical properties of the hollow Co_3O_4 nanoboxes and the Co_3O_4/LSG composite

To test the electrochemical performance of the as-prepared Co_3O_4 nanoboxes and the Co_3O_4/LSG composite, a three-electrode measurement was carried out, in which an Hg/HgO electrode was used as the reference and 6.0 M KOH as the electrolyte. During the test, typical Faradaic peaks were observed in the cyclic voltammetry (CV) curves from samples containing Co_3O_4 (Figure 2.7a). These peaks arise from the redox reactions shown in Equations (2.1) and (2.2) [13].

$$Co_3O_4 + OH^- + H_2O \leftrightarrow 3CoOOH + e^- \quad (2.1)$$

$$3CoOOH + 3OH^- \leftrightarrow 3CoO_2 + 3H_2O + 3e^- \quad (2.2)$$

Much higher currents for both the Co_3O_4 nanobox and the Co_3O_4/LSG composite are observed relative to the pure LSG, owing to the very large specific capacity of cobalt oxide. With LSG as a 3D holder, the Co_3O_4 is less likely to aggregate and maintain its hollow structure. Thanks to the unique structure, the electrolyte ions do not have to diffuse all the way into the bulk material

and surface reaction takes place instead, resulting in less apparent redox peaks. Moreover, both LSG and hollow Co_3O_4 contribute to a relatively high surface area (357 m^2/g), which gives rise to a large double layer capacitance. As a result, the CV of the composite material is more rectangular, while the redox peaks are hidden due to overlapping with the double-layer current. Interestingly, the composite CV also exhibits a much larger CV area than the metal oxide. The improved electrochemical performance is obvious from capacity calculations as shown in Figure 2.7b. The capacity of the composite material is 60.0 mC/cm^2, which is 6 times larger than pure metal oxide and 8 times larger than graphene. When converted to volumetric capacity, the composite demonstrates 68.5 C/cm^3, compared to 6.0 C/cm^3 for the LSG electrodes. This is also superior to previously reported graphene/Co_3O_4 composite electrodes, such as 15.4 C/cm^3 (calculated based on a capacitance of 30.8 F/cm^3 and a 0.5 V voltage window) reported by Mazloumi *et al.*[32]. Based on the active mass of the electrode, a specific capacity of 542.3 C/g is derived for our composite material, which is superior to the value of 109.0 C/g reported for Co_3O_4/carbon nanoneedles[33], 293 C/g for Co_3O_4/carbon nanofibers[34], 324.5 C/g for Co_3O_4/MWCNTs[35] and 367.3 C/g for Co_3O_4/graphene[36] (the values have all been recalculated based on the reported capacitance and potential window). When subtracting the capacitance of graphene, the specific capacity attributed to just the constituent Co_3O_4 is calculated to be 682.0 C/g based on 77% mass loading (calculated by thermogravimetric analysis (TGA) of the Co_3O_4/LSG sample, see Figure 2.8). This value demonstrates the good charge storage capability of hollow Co_3O_4 nanoboxes and shows a clear advance over other hollow structures, such as 329.5 C/g for Co_3O_4 nanotubes[37]. This excellent electrochemical performance can be attributed to the increased surface area of the nanoboxes, enabling maximum utilization of the Faradaic properties of Co_3O_4 and resulting in electrodes

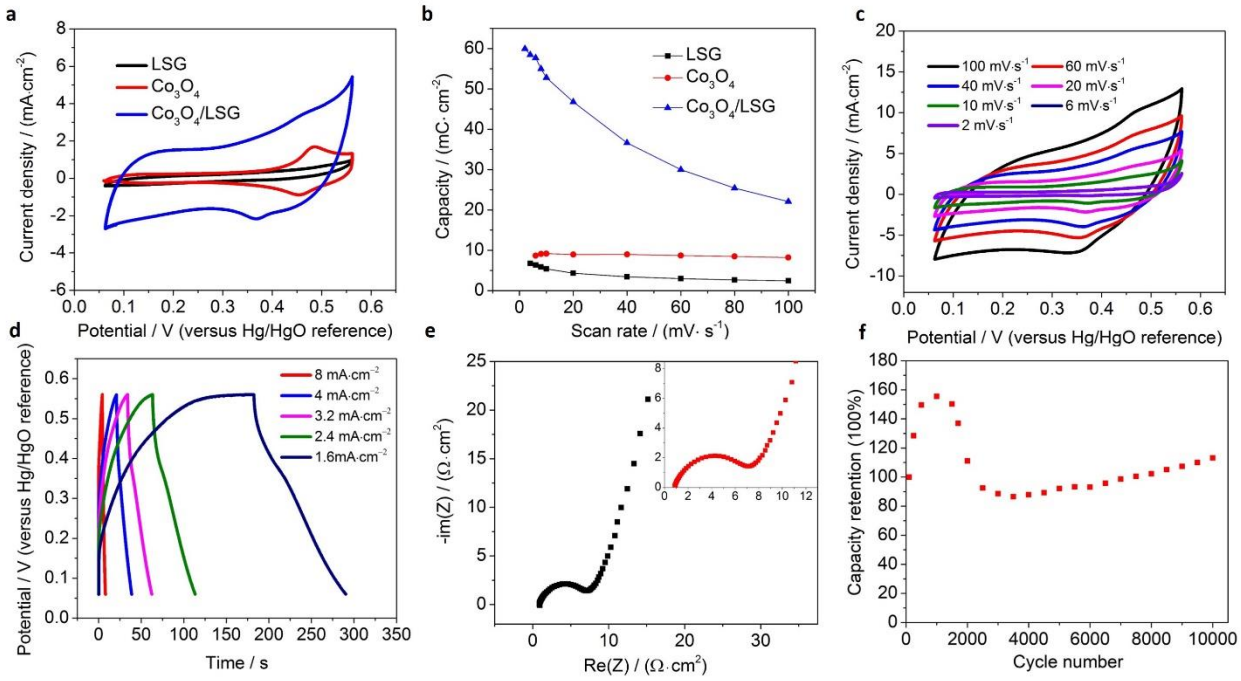

Figure 2.7 (a) Cyclic voltammetry (CV) comparison of the Co_3O_4/LSG composite, LSG and pure metal oxide at a scan rate of 20 mV/s. (b) Areal capacity comparing the Co_3O_4/LSG composite, LSG and pure metal oxide at different scan rates. (c) CVs of the Co_3O_4/LSG composite at scan rates from 2 to 100 mV/s, displaying similar shape. (d) Galvanostatic charge/discharge curves of the Co_3O_4/LSG composite at different current densities from 8 to 1.6 mA/cm^2. (e) Nyquist plot of the Co_3O_4/LSG composite demonstrating low resistance for the electrode material, the electrolyte and the inter-particle contacts, as well as low internal charge transfer and ion diffusion resistance. (f) Capacity retention as a function of cycle number indicating that the Co_3O_4/LSG composite is able to maintain its capacity for at least 10,000 cycles.

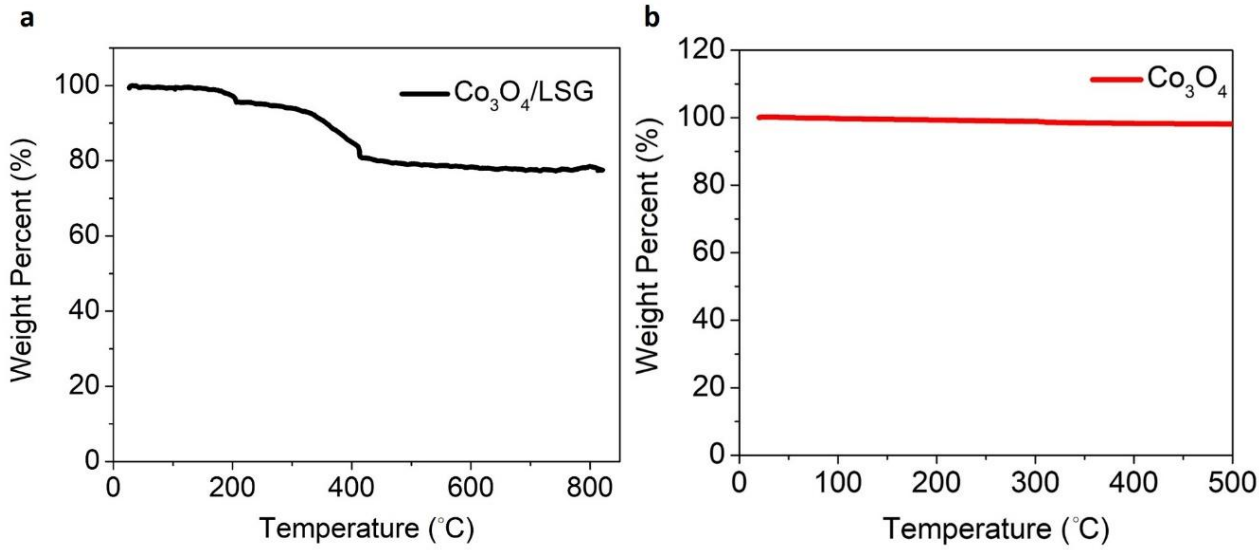

Figure 2.8 (a) Thermogravimetric analysis (TGA) of the Co_3O_4/LSG sample. The composite electrode contains 77% of Co_3O_4 by weight. (b) TGA curve of hollow Co_3O_4 nanoboxes. There is no apparent weight loss even after heating to 500 °C, indicating the good thermal stability of the cobalt oxide nanoboxes.

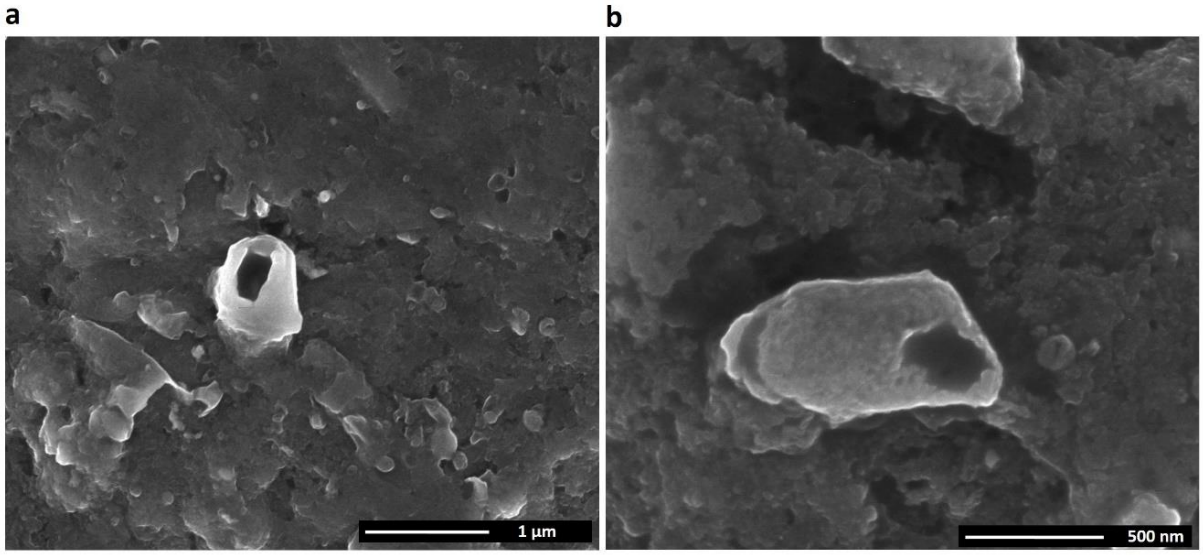

Figure 2.9 (a) and (b) are SEM images of the Co_3O_4/LSG composite after 10,000 cycles. As the images show, the nanoboxes still maintain their hollow structure even when cycled for a long time, confirming that the structure is stable.

with ultrahigh specific capacity. In addition, the synergetic interactions between LSG and Co_3O_4 help improve the overall performance of the composite. In such a hybrid material system, the LSG keeps the Co_3O_4 nanoboxes from aggregating, maintaining the intrinsic properties, while also contributing a significant amount of EDLC capacitance. The electrically conductive framework of LSG enhances the charge transfer from the metal oxide, more fully utilizing the potential capacity of Co_3O_4. The porous structure of the film also facilitates ion migration in the electrolyte. As a result, the conductivity of the whole system, both electronic and ionic, is improved. This is also reflected in the CV and Constant current charge and discharge curves (CC) curves shown in Figures 2.7c-d. Even at a high scan rate of 100 mV/s, the shape of the LSG/Co_3O_4 composite CV is similar to those at lower scan rates. Similarly, the time for charging/discharging is almost inversely proportional to the current density and there's no apparent iR drop in Figure 2.7d, indicating fast charge propagation and good power output. The internal resistance shown in the Nyquist impedance plot in Figure 2.7e provides further evidence for the high power density of this composite electrode. As explained[38], the equivalent series resistance (ESR) measured as the curve's intercept with the x-axis including the electrode material, the electrolyte and the inter-particle contacts, is as low as 0.9 Ω in the figure. In addition, there's no 45-degree diagonal in the plot, accounting for the good ion diffusion process. The semi-circle observed corresponds to a Faradaic resistance[38] of less than 8 Ω, related to the redox reaction and charge transfer. At the same time, the electrochemical processes within the Co_3O_4/LSG composite are highly reversible as the electrode maintains 113.1% of its original capacity after 10,000 cycles (Figure 2.7f) without the breakdown of the hollow structure (Figure 2.9). Onward from the first cycle, the capacity keeps increasing reaching a maximum at ~1000 cycles. This can be attributed to electrochemical activation processes commonly encountered in carbon and metal oxide electrodes.

In order to understand the role of the hollow structure of the Co_3O_4 nanoboxes, we fabricated composite electrodes using LSG in combination with commercially available round and solid Co_3O_4 particles at the same mass loading. The electrochemical performance of these composite electrodes are presented in Figure 2.10. The current density of the hollow metal oxide nanoboxes is much larger than commercial Co_3O_4, both in its pure form (Figure 2.10a) and in a composite electrode (Figure 2.10b). The CV curve of the composite material is more rectangular than the composite containing commercial Co_3O_4 due to fast surface reaction and large double layer capacitance from the hollow structure. The corresponding capacity derived from the CV curves are shown in Figure 2.10c, which agrees very well with the results discussed above. The excellent performance of our materials can be attributed to the hollow structure of Co_3O_4, as explained in the schematic illustration shown in Figure 2.11. The hollow metal oxide supplies not only accessible outer surfaces, but also makes the inside surfaces available, offering more surface area for ion absorption and active sites for redox reactions. Here, all the materials are expected to be used more efficiently, leaving behind less dead mass. In contrast to the solid morphology, ions are able to move readily through the open cavities in the hollow nanoboxes, leading to enhanced wetting properties. In addition, the ion diffusion length and charge transfer distance are shortened since only near surfaces are involved, further expediting ion migration.

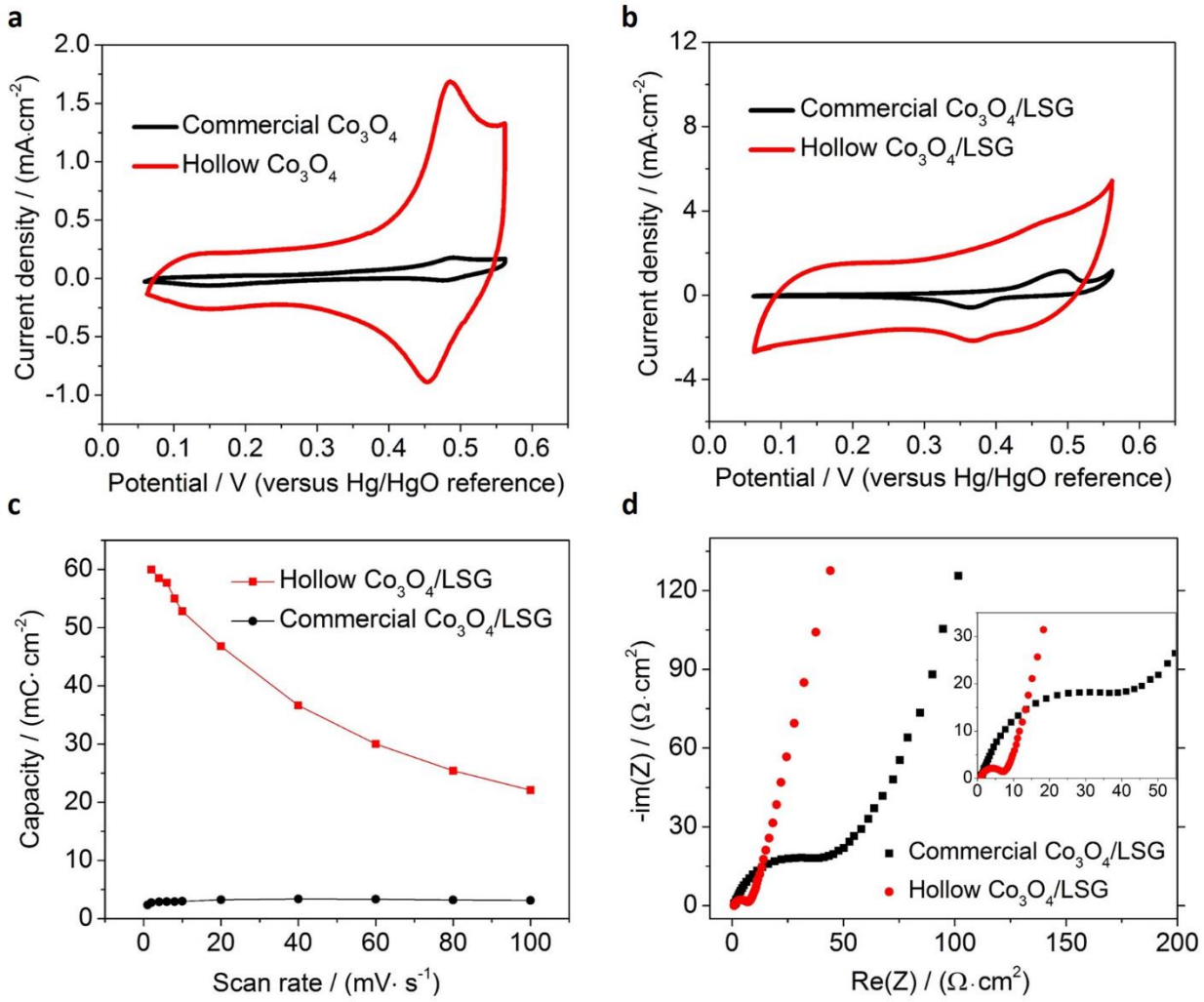

Figure 2.10 (a) Cyclic voltammetry comparison of commercial Co_3O_4 and as prepared Co_3O_4 hollow nanoboxes at 20 mV/s. (b) CV comparison of commercial and hollow Co_3O_4/LSG composites at 20 mV/s. (c) Areal capacity comparing commercial and hollow Co_3O_4/LSG composites at scan rates from 2 to 100 mV/s. (d) Nyquist plots of the commercial and hollow Co_3O_4/LSG composites, showing the lower charge transfer and ion diffusion resistance of the hollow Co_3O_4/LSG composite.

These explanations are backed up by the EIS measurements (Figure 2.10d). In contrast to the hollow Co_3O_4/LSG composite, the commercial Co_3O_4/LSG composite exhibits a much larger semi-circle, which means a significant charge transfer resistance. The commercial composite also shows an obvious 45-degree diagonal between 50 and 70 ohms, due to the more difficult ion diffusion processes. These results demonstrate the outstanding electrochemical performance of hollow Co_3O_4 nanoboxes embedded in a 3D macro-porous graphene matrix (Figure 2.12).

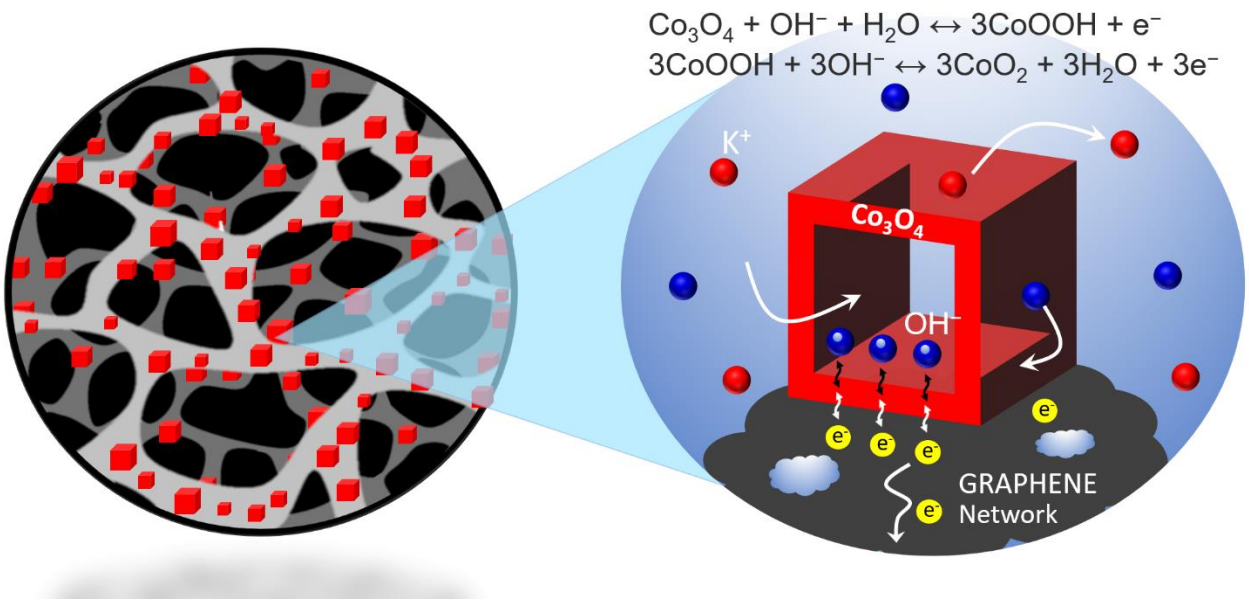

Figure 2.11 Schematic illustration showing the advantage of using hollow Co3O4 nanoboxes. I. Both the inside and the outside surfaces of the metal oxide can be utilized, providing more sites for redox reactions and ion absorption. II. Ions can diffuse freely throughout the cavity to the surfaces, easing the wetting of the material and enhancing the power output. III. More active materials are accessible compared to a solid morphology, thus lowering the amount of dead mass.

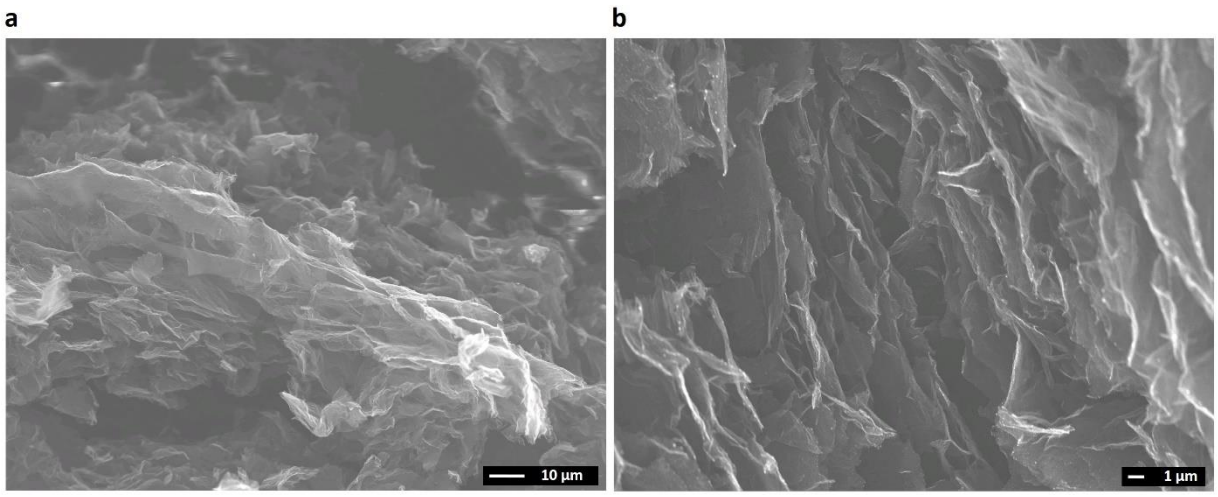

Figure 2.12 (a) and (b) show SEM images of macroporous laser scribed graphene.

2.5 Conclusions

In this report, we have demonstrated a facile method to fabricate hollow Co_3O_4/LSG electrodes. Hollow Co_3O_4 nanoboxes are made via low temperature recrystallization, followed by a calcination process. The as-prepared metal oxide is then mixed with a GO solution, cast as a film, and the GO component is photothermally reduced to LSG using a CO_2 laser. Thanks to the unique structure of the hollow Co_3O_4 nanoboxes and a synergetic effect between the metal oxide and the LSG matrix, the composite exhibits a large surface area, good ion diffusion and fast charge transfer, leading to excellent electrochemical performance. This composite electrode demonstrates ultrahigh specific capacity, low internal resistance and excellent cycling stability. These interesting features of hollow Co_3O_4/LSG offer a great opportunity to increase the energy density of state-of-the-art supercapacitors.

2.6 Appendix to Chapter 2

Specific surface area measurement by methylene blue adsorption:

The specific surface area of the Co_3O_4/LSG composite is determined by the methylene blue adsorption method[42]. A known concentration of methylene blue is made by dissolving the dye into DI water. The initial absorbance of the solution is measured by UV-vis spectroscopy at 665 nm. A certain amount of the composite material is added into the dye solution and stirred for 24 hours to get maximum adsorption. The solution is then centrifuged at high speed to remove any suspended particles and its absorbance is measured. By comparing the concentration before and after adding the composite material, the amount of the methylene blue adsorbed can be determined. Since each methylene blue molecule has a surface area of 1.35 nm^2, the specific surface of the Co_3O_4/LSG composite can be calculated accordingly.

Calculations:

The areal capacities of LSG, Co_3O_4 and Co_3O_4/LSG are calculated from Cyclic Voltammetry at different scan rates:

Areal Capacity $\mathrm{C}\ (C\ cm^{-2}) = \frac{\int_{V_1}^{V_2} idV}{v\ S}$ ($V_1(Volt)$ and $V_2(Volt)$ are the potential range, $i\ (A)$ is the current, $v(Volt\ sec^{-1})$ is the scan rate, $S(cm^2)$ is the electrode area)

Specific Capacity $\mathrm{C}\ (C\ g^{-1}) = \frac{\int_{V_1}^{V_2} idV}{v\ Mass}$ (Mass refers to the weight of the active materials in g)

2.7 References

(1) Simon, P.; Gogotsi, Y. Materials for electrochemical capacitors. *Nat. Mater.* **2008**, *7*, 845-854.

(2) Burke, A. R&D considerations for the performance and application of electrochemical capacitors. *Electrochim. Acta* **2007**, *53*, 1083-1091.

(3) Miller, J. R.; Burke, A. F. Electrochemical capacitors: challenges and opportunities for real-world applications. *Electrochem. Soc. Interface* **2008**, *17*, 53.

(4) Simon, P.; Gogotsi, Y.; Dunn B. Where do batteries end and supercapacitors begin? *Science* **2014**, *343*, 1210-1211.

(5) Winter, M.; Brodd R. J. What are batteries, fuel cells, and supercapacitors? *Chem. Rev.* **2004**, *104*, 4245-4270.

(6) Brousse, T.; Bélanger, D.; Long, J.W. To be or not to be pseudocapacitive? *J. Electrochem. Soc.* **2015**, 162, 5185-A5189.

(7) Zhang, L. L.; Zhao X. S. Carbon-based materials as supercapacitor electrodes. *Chem. Soc. Rev.* **2009**, *38*, 2520-2531.

(8) Kou, T.; Yao, B.; Liu, T.; Li, Y. Recent advances in chemical methods for activating carbon and metal oxide based electrodes for supercapacitors. *J. Mate. Chem. A*, **2017**, *5*, 17151-17173.

(9) El-Kady, M. F.; Strong, V.; Dubin, S.; Kaner, R. B. Laser scribing of high-performance and flexible graphene-based electrochemical capacitors. *Science* **2012**, *335*, 1326-1330.

(10) Shao, Y.; El-Kady, M. F.; Lin, C. W.; Zhu, G.; Marsh, K. L.; Hwang, J. Y.; Zhang, Q.; Li, Y.; Wang, H.; Kaner, R. B. 3D Freeze-Casting of Cellular Graphene Films for Ultrahigh-Power-Density Supercapacitors. *Adv. Mater.* **2016**, *28*, 6719-6726.

(11) Wang, L. J.; El-Kady, M. F.; Dubin, S.; Hwang, J. Y.; Shao, Y.; Marsh, K.; McVerry, B.; Kowal, M. D.; Mousavi, M. F.; Kaner, R. B. Flash Converted Graphene for Ultra-High Power Supercapacitors. *Adv. Energy Mater.* **2015**, *5*, 1500786.

(12) El-Kady, M. F.; Ihns, M.; Li, M.; Hwang, J. Y.; Mousavi, M. F.; Chaney, L.; Lech, A.T.; Kaner, R. B. Engineering three-dimensional hybrid supercapacitors and microsupercapacitors for high-performance integrated energy storage. *Proc. Natl. Acad. Sci. U.S.A.* **2015**, *112*, 4233-4238.

(13) Zhi, M.; Xiang, C.; Li, J.; Li, M.; Wu, N. Nanostructured carbon–metal oxide composite electrodes for supercapacitors: a review. *Nanoscale* **2013**, *5*, 72-88.

(14) Wang, L.; Ji, H.; Wang, S.; Kong, L.; Jiang, X.; Yang, G. Preparation of Fe_3O_4 with high specific surface area and improved capacitance as a supercapacitor. *Nanoscale* **2013**, *5*, 3793-3799.

(15) Chen, Y.; Wang Y.; Sun, P.; Yang, P.; Du, L.; Mai, W. Nickel oxide nanoflake-based bifunctional glass electrodes with superior cyclic stability for energy storage and electrochromic applications. *J. Mater. Chem. A* **2015**, *3*, 20614-20618.

(16) Wang, Y.; Wei, H.; Wang, J.; Liu, J.; Guo, J.; Zhang, X.; Weeks, B. L.; Shen, T. D.; Wei, S.; Guo, Z. Electropolymerized polyaniline/manganese iron oxide hybrids with an enhanced color switching response and electrochemical energy storage. *J. Mater. Chem. A* **2015**, *3*, 20778-20790.

(17) Li, Y.; Tan, B.; Wu, Y. Mesoporous Co_3O_4 nanowire arrays for lithium ion batteries with high capacity and rate capability. *Nano Lett.* **2008**, *8*, 265-270.

(18) Du, N.; Zhang, H.; Chen, B. D.; Wu, J. B.; Ma, X. Y.; Liu, Z. H.; Zhang, Y. Q.; Yang, D. R.; Huang, X. H.; Tu, J. P. Porous Co_3O_4 Nanotubes Derived From $Co_4(CO)_{12}$ Clusters on

Carbon Nanotube Templates: A Highly Efficient Material For Li-Battery Applications. *Adv. Mater*. **2007**, *19*, 4505-4509.

(19) Tian, L.; Zou, H.; Fu, J.; Yang, X.; Wang, Y.; Guo, H.; Fu, X.; Liang, C.; Wu, M.; Shen, P. K.; Gao, Q. Topotactic Conversion Route to Mesoporous Quasi-Single-Crystalline Co_3O_4 Nanobelts with Optimizable Electrochemical Performance. *Adv. Funct. Mater.* **2010**, *20*, 617-623.

(20) Lou, X. W.; Deng, D.; Lee, J. Y.; Feng, J.; Archer, L. A. Self-Supported Formation of Needlelike Co_3O_4 Nanotubes and Their Application as Lithium-Ion Battery Electrodes. *Adv. Mater*. **2008**, *20*, 258-262.

(21) Cheng, G.; Kou, T.; Zhang, J.; Si, C.; Gao, H.; Zhang, Z. O_2^{2-}/O^- Functionalized Oxygen-deficient Co_3O_4 Nanorods as High Performance Supercapacitor Electrodes and Electrocatalysts towards Water Splitting. *Nano Energy* **2017**, *38*, 155-166.

(22) Du, W.; Liu, R.; Jiang, Y.; Lu, Q.; Fan, Y.; Gao, F. Facile synthesis of hollow Co_3O_4 boxes for high capacity supercapacitor. *J. Power Sources* **2013**, *227*, 101-105.

(23) Xuan, L.; Chen, L.; Yang, Q.; Chen, W.; Hou, X.; Jiang, Y.; Zhang, Q.; Yuan, Y. Engineering 2D multi-layer graphene-like Co_3O_4 thin sheets with vertically aligned nanosheets as basic building units for advanced pseudocapacitor materials. *J. Mater. Chem. A*, **2015**, *3*, 17525-17533.

(24) Xia, X. H.; Tu, J. P.; Wang, X. L.; Gu, C. D.; Zhao, X. B. Mesoporous Co_3O_4 monolayer hollow-sphere array as electrochemical pseudocapacitor material. *Chem. Commun*. **2011**, *47*, 5786-5788.

(25) He, T.; Chen, D.; Jiao, X.; Wang, Y. Co_3O_4 Nanoboxes: Surfactant-Templated Fabrication and Microstructure Characterization. *Adv. Mater.* **2006**, *18*, 1078-1082.

(26) Wang, X.; Fu, H.; Peng, A.; Zhai, T.; Ma, Y.; Yuan, F.; Yao, J. One-pot solution synthesis of cubic cobalt nanoskeletons. *Adv. Mater.* **2009**, *21*, 1636-1640.

(27) Hwang, J. Y.; El-Kady, M. F.; Wang, Y.; Wang, L.; Shao, Y.; Marsh, K.; Ko, J. M.; Kaner, R.B. Direct preparation and processing of graphene/RuO_2 nanocomposite electrodes for high-performance capacitive energy storage. *Nano Energy* **2015**, *18*, 57-70.

(28) Foo, C. Y.; Sumboja, A.; Tan, D. J. H.; Wang, J.; Lee, P.S. Flexible and Highly Scalable V_2O_5-rGO Electrodes in an Organic Electrolyte for Supercapacitor Devices. *Adv. Energy Mater.* **2014**, *4*, 1400236.

(29) Yin, Y.; Rioux, R. M.; Erdonmez, C. K.; Hughes, S.; Somorjai, G. A.; Alivisatos, A. P. Formation of hollow nanocrystals through the nanoscale Kirkendall effect. *Science* **2004**, *304*, 711-714.

(30) Xu, J.; Wu, J.; Luo, L.; Chen, X.; Qin, H.; Dravid, V.; Mi, S.; Jia, C. Co_3O_4 nanocubes homogeneously assembled on few-layer graphene for high energy density lithium-ion batteries. *J. Power Sources* **2015**, *274*, 816-822.

(31) Ni, Z.; Wang, Y.; Yu T.; Shen, Z. Raman spectroscopy and imaging of graphene. *Nano Res.* **2008**, *1*, 273-291.

(32) Mazloumi, M.; Shadmehr, S.; Rangom, Y.; Nazar, L. F.; Tang, X. Fabrication of three-dimensional carbon nanotube and metal oxide hybrid mesoporous architectures. *ACS nano* **2013**, *7*, 4281-4288.

(33) Silva, R.; Pereira, G. M.; Voiry, D.; Chhowalla, M.; Asefa, T. Co_3O_4 Nanoparticles/ Cellulose Nanowhiskers-Derived Amorphous Carbon Nanoneedles: Sustainable Materials for Supercapacitors and Oxygen Reduction Electrocatalysis. *RSC Adv.* **2015**, *5*, 49385-49391.

(34) Abouali, S.; Akbari Garakani, M.; Zhang, B.; Xu, Z. L.; Kamali Heidari, E.; Huang, J. Q.; Huang, J.; Kim, J. K. Electrospun Carbon Nanofibers with in situ Encapsulated Co_3O_4 Nanoparticles as Electrodes for High Performance Supercapacitors. *ACS Appl. Mater. Interfaces* **2015**, *7*, 13503-13511.

(35) Wang, X.; Li, M.; Chang, Z.; Yang, Y.; Wu, Y.; Liu, X. Co_3O_4@MWCNT nanocable as cathode with superior electrochemical performance for supercapacitors. *ACS Appl. Mater. Interfaces* **2015**, *7*, 2280-2285.

(36) Dong, X. C.; Xu, H.; Wang, X. W.; Huang, Y. X.; Chan-Park, M. B.; Zhang, H.; Wang, L. H.; Huang, W.; Chen, P. 3D graphene–cobalt oxide electrode for high-performance supercapacitor and enzymeless glucose detection. *ACS nano* **2012**, *6*, 3206-3213.

(37) Xia, X. H.; Tu, J. P.; Mai, Y. J.; Wang, X. L.; Gu, C. D.; Zhao, X. B. Self-supported hydrothermal synthesized hollow Co_3O_4 nanowire arrays with high supercapacitor capacitance. *J. Mater. Chem.* **2011**, *21*, 9319-9325.

(38) Conway, B. E. *Electrochemical supercapacitors: scientific fundamentals and technological applications*; Springer Science & Business Media: New York, **2013**.

(39) Lian, C.; Wang, Z.; Lin, R.; Wang, D.; Chen, C.; Li, Y. An efficient, controllable and facile two-step synthesis strategy: Fe_3O_4@RGO composites with various Fe_3O_4 nanoparticles and their supercapacitance properties. *Nano Res.* **2017**, *10*, 3303-3313.

(40) Zhang, X.; Shi, W.; Zhu, J.; Zhao, W.; Ma, J.; Mhaisalkar, S.; Maria, T.L.; Yang, Y.; Zhang, H.; Hng, H.H.; Yan, Q. Synthesis of porous NiO nanocrystals with controllable surface area and their application as supercapacitor electrodes. *Nano Res.* **2010**, *3*, 643-652.

(41) Peng, Y.; Chen, Z.; Wen, J.; Xiao, Q.; Weng, D.; He, S.; Geng, H.; Lu, Y. Hierarchical manganese oxide/carbon nanocomposites for supercapacitor electrodes. *Nano Res*. **2011**, *4*, 216-225.

(42) Hang, P.T.; Brindley, G.W. Methylene blue absorption by clay minerals. Determination of surface areas and cation exchange capacities (clay-organic studies XVIII). *Clays Clay Miner*. **1970**, *18*, 203-212

CHAPTER 3

Next-Generation Activated Carbon Supercapacitors: A Simple Step in Electrode Processing Leads to Remarkable Gains in Energy Density

3.1 Abstract

The global supercapacitor market has been growing rapidly during the past decade. Today, virtually all commercial devices use activated carbon. In this work, we show that laser treatment of activated carbon electrodes result in the formation of micro-channels that can connect the internal pores of activated carbon with the surrounding electrolyte. These micro-channels serve as electrolyte reservoirs that in turn shorten the ion diffusion distance and enable better interaction between the electrode surfaces and electrolyte ions. The capacitance can be further increased through fast and reversible redox reactions on the electrode surface using a redox active electrolyte, enabling the operation of a symmetric device at 2.0 V, much higher than the thermodynamic decompostion voltage of water. This simple approach can alleviate the low energy density of supercapacitors which has limited the widespread use of this technology. This work represents a clear advancement in the processing of activated carbon electrodes towards the next-generation of low-cost supercapacitors.

3.2 Introduction

The need for higher energy density storage devices has increased rapidly due to the burgeoning market for portable electronic devices.[1] Besides battery, electrochemical capacitors (ECs) have garnered a great deal of attention due to their high power density, excellent low temperature performance and essentially unlimited charge/discharge cycles. Today, virtually all ECs use activated carbon derived from coconut-shells as the active material, aluminum current

collectors and tetraethylammonium tetrafluoroborate in acetonitrile as the electrolyte.[2] While these carbon supercapacitors demonstrate excellent electrochemical performance, the high cost per kWh has limited the wide-spread adoption of this technology. Compared to lithium ion batteries, supercapacitors provide energy at 10 times higher cost per kWh.[3] This not only is a major concern for capacitive energy storage, but also it prevents supercapacitors from replacing batteries in many applications. Here, we suggest two strategies for solving this problem. The first involves increasing the capacitance of carbon electrodes through a simple yet effective step in the electrode processing currently used in the manufacture of supercapacitors. The second strategy focuses on the use of redox active electrolytes, increasing capacitance and reducing cost of fabrication relative to the currently used more expensive organic electrolytes. Increasing the capacitance of carbon electrodes will reduce the cost of storing energy in supercapacitors.

Although other forms of carbon such as carbon aerogels, carbon nanotubes and graphene have been developed, activated carbon is still attractive because of its low cost and well-established electrochemical properties. In addition, activated carbons can be solution processed and thus provide an effective means for the manufacture of supercapacitors using standard industrial processes from slurry preparation, coating and drying, calendering, slitting, welding, electrolyte filling and packaging. Here, we discovered that laser irradiation of the carbon coated electrodes results in the formation of microscale trenches that provide better means for storing electrolyte for effective charging and discharging. Laser scribed activated carbon (LSAC) can also reduce the distance over which the ions will have to move during charge and discharge processes. As a result, laser scribed carbon electrodes demonstrate both higher capacitance and lower internal resistance. This method provides an effective strategy for the design and fabrication of high-energy carbon

electrodes with only one simple additive to the electrode processing techniques that are currently utilized for the industrial production of supercapacitors.

Another way for reducing the cost of carbon supercapacitors is to replace the expensive components in the current technology with inexpensive alternatives without compromising the cell performance. For example, a cost breakdown of a supercapacitor cell shows that the greatest cost driver is the organic salt used for making the electrolyte.[4] These electrolytes are generally made by dissolving tetraethylammonium tetrafluoroborate salt in acetonitrile or propylene carbonate. While this allows the operation of ECs at a relatively high voltage of 2.7 V, this electrolyte is flammable and has a fairly low ionic conductivity. Therefore, in order to reduce the cost and improve safety of carbon supercapacitors, it is imperative to replace the organic electrolyte with a less expensive and safer alternative. A good choice maybe aqueous electrolytes due to their low cost and environmentally friendly energy storage applications.[5] Because of their high ionic conductivity, aqueous electrolytes have the capability to not only increase the capacitance, but also enhance the power density of carbon-based supercapacitors. The major disadvantage of an aqueous electrolyte is the low operating voltage window dictated by the thermodynamic decomposition of water at 1.23 V.[6] Recently, a number of aqueous supercapacitors have demonstrated higher voltages by utilizing asymmetric designs instead of conventional two symmetric carbon electrodes. This configuration takes advantage of the large hydrogen evolution overpotential of carbon negative electrodes and the large specific capacitance of metal oxide positive electrodes for extending the operating voltage window beyond the thermodynamic breakdown voltage of water. This has enabled aqueous supercapacitors that can store and deliver the charge at voltages as high as 2.0 V.[7,8] However, this system has several drawbacks. First, the charge of the positive and negative electrodes (Q) must be balanced to ensure maximum cycling stability. Second, carbon-

metal oxide composites often require complicated synthetic procedures that adds to the cost. Third, unlike traditional carbon supercapacitors which can be used for millions of cycles, asymmetric devices often suffer from stability issues resulting from the rapid degradation of metal oxide-based electrodes.

Instead of using an asymmetric design, the voltage of symmetric aqueous-based ECs can be increased by modifying the physicochemical properties of the electrolyte or surface chemistry of the electrode materials. In this way, the overpotential for hydrogen and oxygen evolution can be tuned to avoid the decomposition of water at low voltages.[6] Several examples from the recent literature demonstrate the feasibility of this approach. For instance, Boettcher, Stucky and co-workers discovered a unique redox electrolyte based on methyl viologen that not only increases the voltage window of an activated carbon supercapacitor, but also its specific capacitance.[9] This system, however, is limited to 1.4 V, so that further improvements are still needed. Fic and co-workers extended the voltage of symmetric carbon supercapacitors up to 2.2 V, using a 1.0 M Li_2SO_4 aqueous electrolyte.[10] However, such an impressive voltage was obtained using expensive gold current collectors, whereas practical systems use aluminum in which parasitic and corrosion reactions are difficult to avoid. Besides, this set-up can only store charge in electric double layers, whose limited specific capacitance is the reason behind the low energy density of carbon-based supercapacitors.

Herein, we demonstrate that laser scribing of standard activated carbon electrodes results in the formation of macroporous electrodes, allowing for a new generation of carbon supercapacitors with improved power density. Furthermore, the introduction of a 0.1 M ferricyanide/ferrocyanide redox couple into the electrolyte enables supercapacitors with an 8-fold increase in capacitance compared with a control supercapacitor without the redox electrolyte. In

addition, the redox electrolyte enables the operation of the supercapacitor at an enhanced voltage of 2.0 V. We also note that the micro-channels formed in the electrode can facilitate charge transport and enable charge storage at high rates. The combination of this unique architecture with a redox electrolyte leads to synergetic effects and produces high areal capacitance (up to 379 mF cm^{-2}), specific power (up to 5.26 W cm^{-3}), specific energy (up to 9.05 mWh cm^{-3}) and low ESR (1.6 Ω cm^2). Note that these supercapacitor cells can be assembled in air without using any special dry rooms or glove boxes. In addition, the laser irradiation was performed using standard laser cutting tools that are widely utilized in industry.[11,12] This interesting performance was achieved with industrial grade active materials, current collectors and separators and may, thus, have potential for real-world applications.

3.3. Results and Discussion

3.3.1. Fabrication of laser scribed activated carbon (LSAC) electrodes

Today, activated carbons are the most popular materials used for the manufacturing of supercapacitors due to their high surface area (up to 3033 m^2 g^{-1}),[13] low cost and high packing density (0.5-0.8 g/cm^3). However, activated carbons contain some micrometer size particles with complex porosity that leads to slow ion diffusion and low power density. Additionally, most of the surface area resides within small micropores that are inaccessible to the electrolyte ions, leading to significant dead mass and low specific capacitance. To overcome these problems, researchers have suggested graphene as an alternative electrode material because of its outstanding surface area that is readily accessible to the electrolyte ions. Graphene electrodes with very high gravimetric capacitance (~300 F g^{-1}) have already been demonstrated, but low packing density values (~0.1 g cm^{-3}) have limited the performance of these devices when considering the mass of a fully packaged cell.[14] There have been some efforts made to increase the packing density of

garphene electrodes,[15] however, this approach is very challenging because of the tendency of graphene sheets to restack. This suggests that low packing density materials like graphene and other forms of nanocarbons may not be sufficient for commercial applications. Therefore, here we undertake a unique approach to improve the power density of activated carbon while keeping the high electrode packing density needed for practical devices.

High packing density (0.60 g cm^{-3}) activated carbon electrodes were fabricated on carbon coated aluminum current collectors using a standard doctor blade coating technique. Exposure of the electrodes to a CO_2 laser results in the formation of microscale size trenches as illustrated in Figure 3.1A. Figure 3.1B-G show SEM images of a top view (B,C) and a cross-sectional view (D-G) of the film after exposure to the laser. The pattern with widths of 120.3 µm and depths of 33.2 µm were confirmed through Figures 3.1B, D and E. These results are further established by optical microscopy indicating the appearance of macro-pores in the structure of the electrode following laser irradiation, (Figure. 3.2). Similar results were obtained when processing the electrodes from an organic system with a PVDF binder and an aqueous system with a CMC/SBR binder. Figures 3.1C, F and G show obvious changes to the microstructure of the electrode before (Figure 3.1G) and after (Figure 3.1F) laser irradiation. Zooming in on the laser treated electrode reveals its macro-porous nature with less binder. Basically, electrode texturing takes place as a result of a photo-thermal process in which the binder is burned off leaving behind the electrode with a macro-porous structure. The intense photo-energy delivered by the laser is converted into thermal energy causing the thermal degradation of the binder in part. The binder is a mixture of carboxymethyl cellulose, CMC (the sodium salt) and styrene butadiene rubber (SBR). Figure 3.3, presents thermo-gravimetric analysis (TGA) of activated carbon, binder and an activated carbon/binder electrode. According to Figure 3.3B the binder is thermally annealed

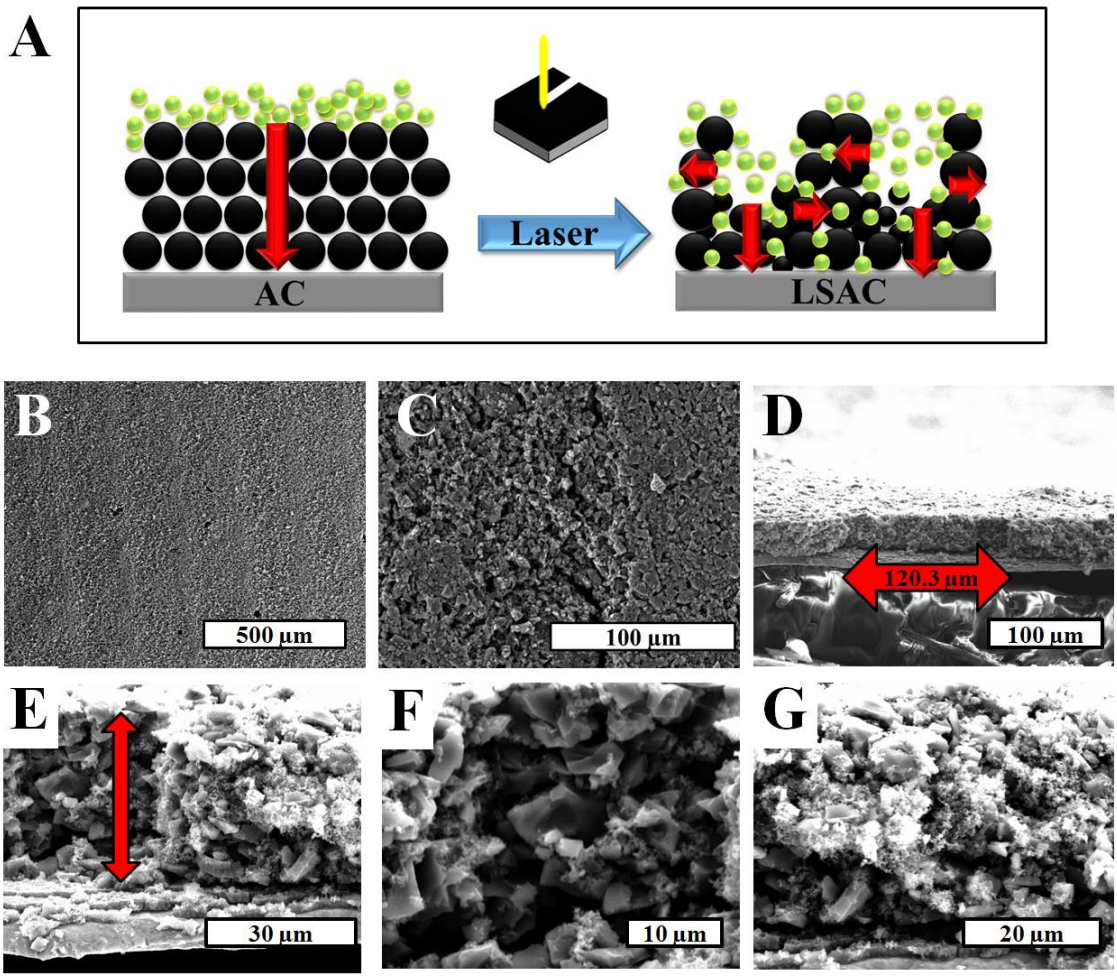

Figure 3.1 Design, structure and characterization of the laser scribed activated carbon (LSAC) electrodes. (A) Schematic illustration showing the fabrication process of laser scribed activated carbon (LSAC) electrodes. The laser treated electrodes contain trenches that serve as electrolyte reservoirs, enabling better interaction between the electrolyte ions and the electrode surfaces. (B) An overview SEM image showing activated carbon after exposure to 7-W laser. (C) A magnified view illustrating the macroporous structure created by laser etching of the activated carbon. Cross sectional view of the SEM showing (D) 120.3 µm spacing laser pattern with (E) 33.2 µm depth. A magnified cross-sectional view of (F) laser treated film in comparison to the (G) pristine film before scribing.

in two steps where CMC is burned off in the first step at 250-300 ºC followed by a second step at around 600 ºC. The CO_2 laser can increase the local temperature to 300-400 ºC, which is sufficient to burn off the CMC binder as CO_2 gas without affecting the activated carbon particles. This opens new macro-pores in the structure of the electrode, leading to enhanced ion transport kinetics. This unique electrode architecture makes a high surface area and porous structure, allowing the electrolyte to interact with the entire surface of the activated materials. In addition, microscale trenches allow for the rapid transport of ions and provide ionic connections between the interior pores of the activated carbon particles and the external electrolyte. These trenches can also reduce the distance over which the ions must move during charge and discharge processes. An additional advantage of this technique is that the electrode maintains its high packing density after laser irradiation (0.54 g cm^{-3}). Therefore, the laser irradiation technique demonstrated in this work enables the direct fabrication of high power/high energy density activated carbon electrodes without compromising their outstanding volumetric performance. In addition, the microscale trenches may help alleviate the stress and strain between particles during charge and dishcarge and leading to improved cycling stability of the supercapacitor.

3.3.2. Electrochemical properties of LSAC electrodes in traditional acetonitrile electrolyte

We investigated the electrochemical properties of the laser scribed activated carbon (LSAC) electrodes in CR2032 coin cell devices using 1.0 M tetraethylammonium tetrafluoroborate ($TEABF_4$) in acetonitrile as the electrolyte. Figure 3.4A shows the cyclic

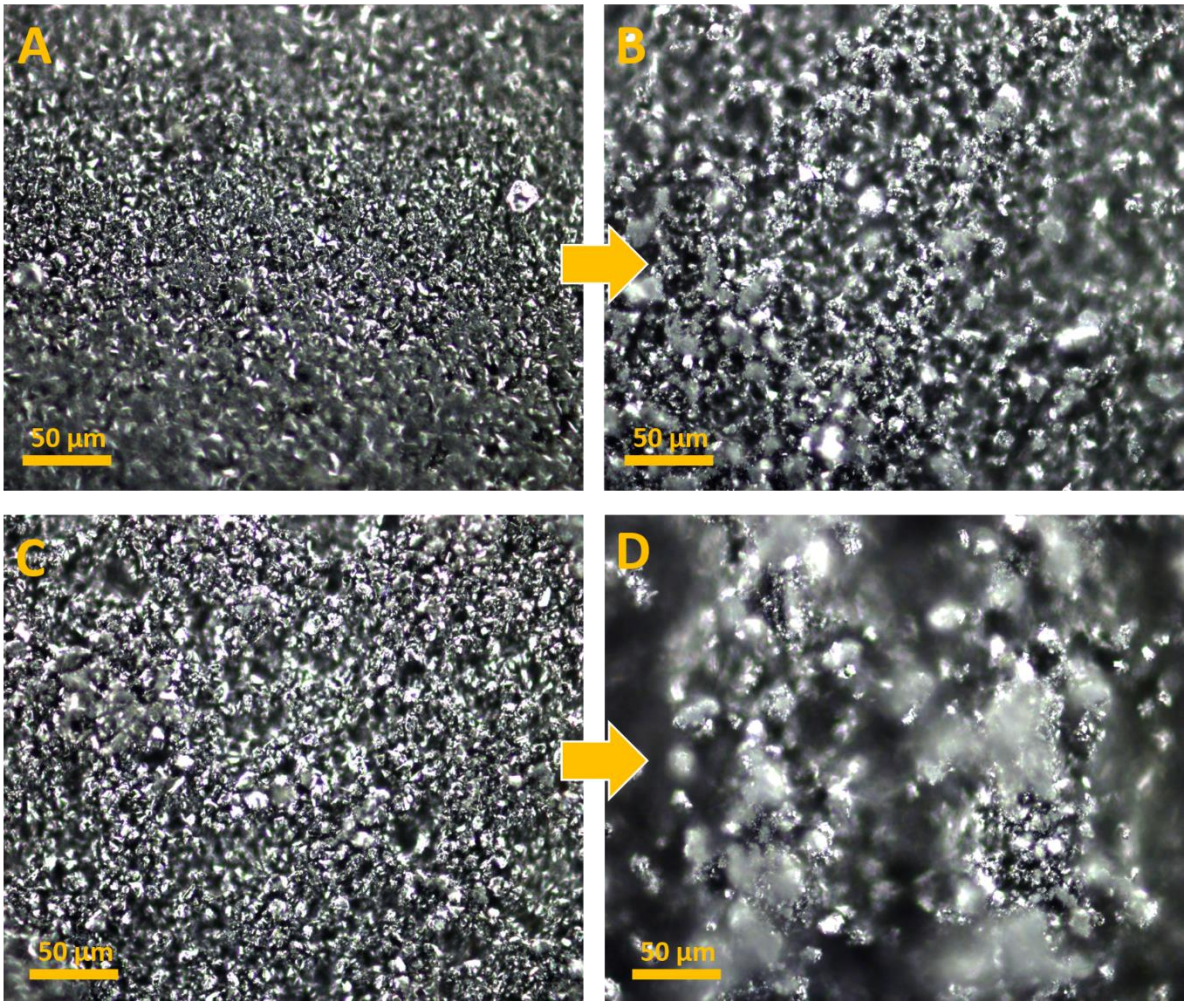

Figure 3.2 Optical microscope images showing the microstructure of the electrode before and after laser scribing. Pictures on the left are for the as-made electrodes and on the right after laser irradiation. Electrodes in (A) and (B) are processed with a PVDF binder whereas electrodes in (C) and (D) use a CMC/SBR binder. The results reveal the appearance of macropores in the structure of the electrode following the laser treatment.

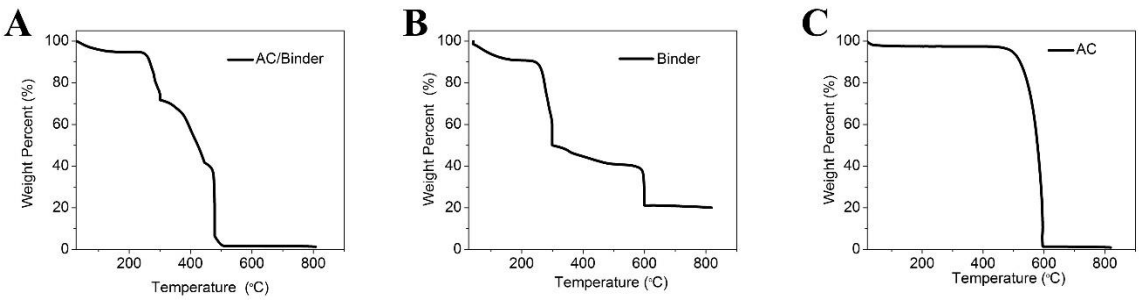

Figure 3.3 Thermo-gravimetric analysis (TGA) of activated (A) carbon/binder composite, (B) binder and (C) activated carbon only. All measurements were performed under air.

voltammetry (CV) of the electrode before and after laser irradiation. In comparison with a non-scribed electrode, the LSAC shows an enhanced capacitance with a nearly textbook rectangular CV curve at 50 mV s^{-1}, suggesting a nearly textbook electric double layer capacitance behavior. This nearly textbook rectangular CV shape of the LSAC supercapacitor is retained even when tested at high scan rates up to 300 mV s^{-1} (Figure 3.4B). In addition, Figure 3.4C shows nearly textbook triangular charge/discharge (CC) curves that can be maintained with a very small IR drop at increasing current densities. Based on these measurements, we calculated the areal capacitances (Figure 3.4D) and gravimetric capacitances (Figure 3.4E) of the electrode at different current densities. Although some active materials were lost during the laser scribing of the microscale trenches, LSAC shows improved capacitance on both a high gravimetric and an areal basis. In addition, LSAC exhibits excellent rate capability with high capacitance retention up to a current density of 25 A g^{-1} at which point the LSAC electrode delivers a 6 times larger capacitance compared to the non-scribed electrode.

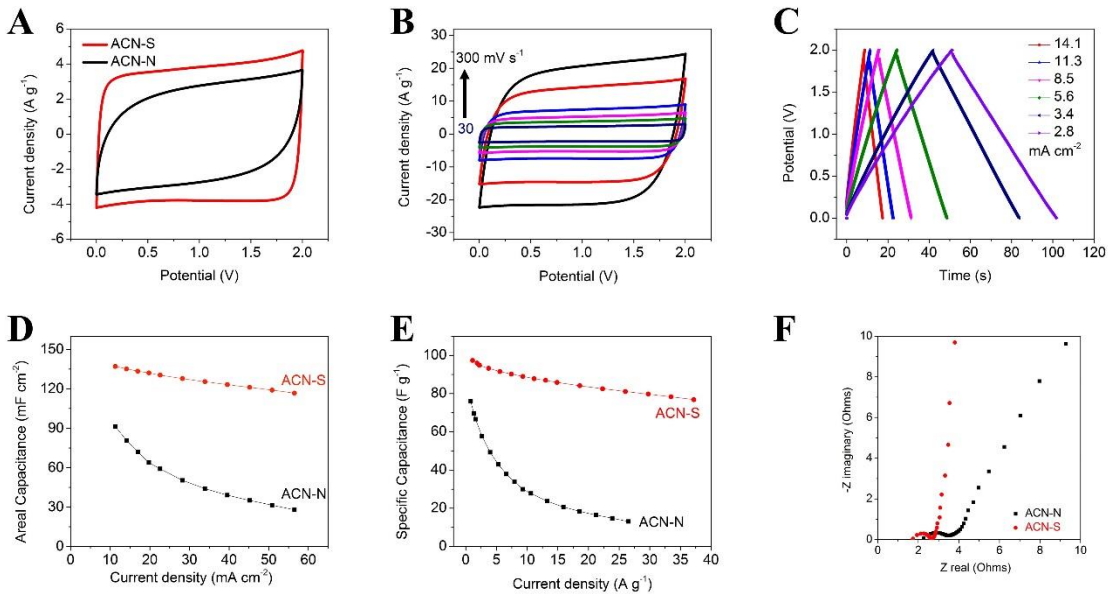

Figure 3.4 Evaluation of the electrochemical performance of laser scribed activated carbon (LSAC) supercapacitors in a traditional 1.0 M tetraethylammonium tetrafluoroborate ($TEABF_4$) in acetonitrile (ACN) electrolyte. (A) Cyclic voltammetry (CV) curves of supercapacitors before (black) and after (red) laser treatment, obtained at a scan rate of 50 mV s^{-1}. (B) CV profiles of an LSAC supercapacitor at different scan rates of 30, 50, 70, 100, 200, and 300 mV s^{-1}. (C) Charge/discharge (CC) curves at different current densities of 1.7, 2.8, 3.4, 5.6, 8.5, 11.3, 14.1 and 16.9 mA cm^{-2}. (D) The areal capacitance retention and (E) gravimetric capacitance retention before (black) and after (red) laser treatment as a function of the applied current density. All the values were measure from the full cell and calculated based on the electrode. (F) Nyquist plots of the LSAC supercapacitor (red) and non-scribed (black) supercapacitor over a frequency range of 0.2 MHz to 0.1 Hz.

Excellent rate capability of LSAC electrodes was further verified from electrochemical impedance measurements. The results indicate that the LSAC electrode show lower equivalent series resistance (ESR) as small as 1.66 Ω, as obtained from the intercept of the Nyquist plot

(Figure 3.4F) on the real axis. In addition, the Nyquist plot of the LSAC electrode is nearly a straight vertical line in the low frequency region, indicating essentially ideal capacitive behavior. These results imply low charge transfer resistance at the electrode/electrolyte interface and suggest rapid electron and ion transport within the LSAC electrode. This can be ascribed to the large macroporous surfaces of the electrode that are easily accessible to the electrolyte ions.

3.3.3. Role of the redox active electrolyte (RE)

While traditional supercapacitors consist of activated carbons as the only electrochemically active material in the cell, redox supercapacitors have now shifted this paradigm. In addition to the active electrode material, more charge can be added by using redox active electrolytes and may, thus, increase the overall capacitance of the cell. For example, Wu *et al.* [16] reported an increase in capacitance of about 4 times by adding p-phenylenediamine (PPD) into a KOH electrolyte; however, this system runs at 1.0 V necessitating further improvements for real world applications. Similarly, Mai *et al.*[17] added cupric chloride ($CuCl_2$) into a HNO_3 electrolyte to increase the capacitance from 440 F g^{-1} to 4700 F g^{-1}. However, such an impressive value was measured in a three electrode system using a very limited voltage window (-0.1 V to 0.4 V). Integration of this electrode into an asymmetric cell (1.35 V) is associated with a huge reduction of the capacitance down to 294 F g^{-1}, likely because of the charge imbalance between the positive and negative electrodes. Here, we propose a ferricyanide/ferrocyanide electrolyte, which adds more capacitance to the cell while at the same time enabling the operation of the cell at a high voltage of up to 2.0 V in an aqueous electrolyte. Unlike most aqueous supercapacitors that use precious metal current collectors (gold, platinum, etc.), this redox supercapacitor employs aluminum current collectors which are widely used today in the manufacturing of supercapacitors and lithium ion batteries.

Aluminum is the preferred current collector in industry because of its high conductivity, light weight and low cost. In addition, it has excellent electrochemical stability in organic electrolytes, but often experiences corrosion in aqueous systems. To confirm that aluminum current collectors are safe to use in our redox electrolyte system, we first built a supercapacitor coin cell consisting of activated carbon electrodes coated on Al using an aqueous 1.0 M Na_2SO_4 electrolyte without any redox additives. Electrochemical testing acquired in this system (Figure 3.5,) shows rapidly changing CV profiles associated with an increase of the ESR after each cycle, which suggests that corrosion of aluminum occurs in the 1.0 M Na_2SO_4. However, surprisingly after we introduce the [$Fe(CN)_6^{3-}$/$Fe(CN)_6^{4-}$] Redox electrolyte (RE) into 1.0 M Na_2SO_4, the electrochemical performance is very stable even at the higher voltage of 2.0 V. A possible explanation is that [$Fe(CN)_6^{3-}$/$Fe(CN)_6^{4-}$] works as a solution buffer and maintains a neutral pH (7.1) while charging and discharging. Note that 1.0 M Na_2SO_4 has a pH of 6. It is also possible that the redox additive acts as a sacrificial anode and thus protects Al from corrosion.

Figure 3.6 shows the electrochemical performance of coin cell supercapacitors containing activated carbon tested at different concentration of the redox additive in 1.0 M Na_2SO_4, denoted as *x* M RE, where *x* is the molar concentration of the additive. Figure 3.6a present CV profiles collected with 0.1 M RE at an increasing voltage window from 1 V to 2 V with an interval of 0.2 V and a scan rate 50 mV s^{-1}. The CV profiles show no significant increase in the current especially in the high voltage end, which signifies that there is no decomposition of the electrolyte and suggests that 2.0 V can be safely applied for a supercapacitor operating in this electrolyte. It was reported that both Na^+ and SO_4^{2-} ions have strong solvation energy which stems from the fact that sulfate ions can be surrounded by 12-16 molecules of water.[10] Therefore, it is possible to assume that the energy that causes the decomposition of water in traditional

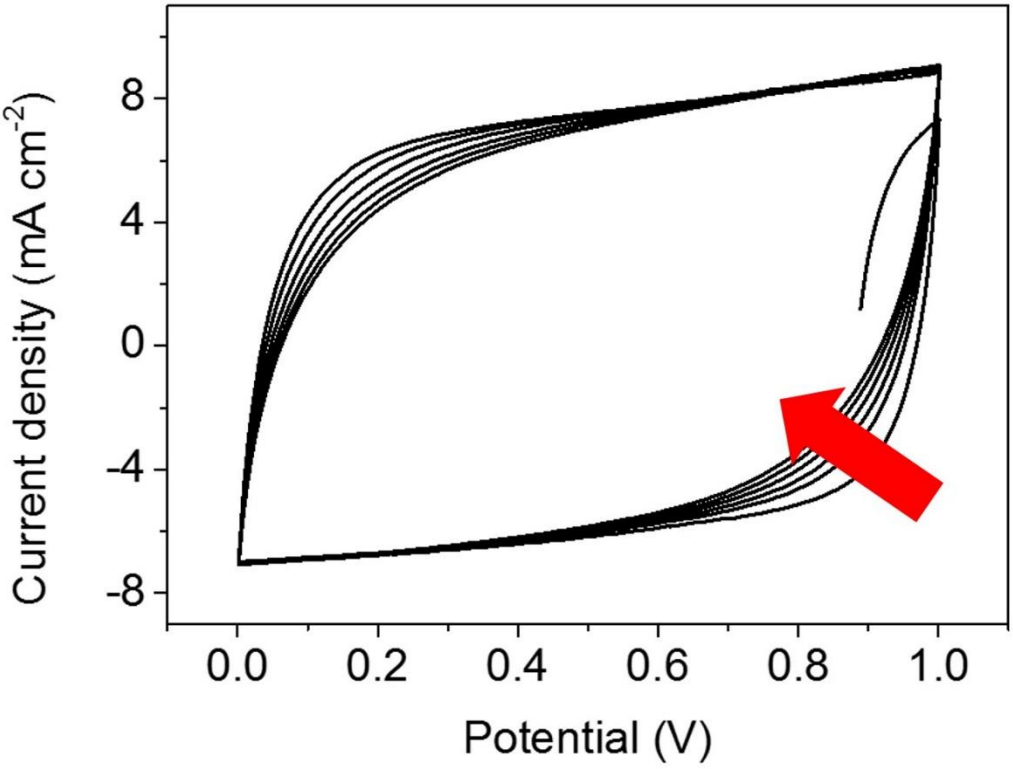

Figure 3.5 Cyclic voltammetry (CV) of an activated carbon electrode (prepared on an aluminum current collector) in 1.0 M Na_2SO_4 measured at 50 mV s^{-1} and repeated for 6 cycles. The device was assembled and tested in a CR 2032 coin cell.

aqueous electrolytes is now used to break the bonds in the solvation shell of Na^+ and SO_4^{2-} ions or even to drive redox reactions of the redox electrolyte. Therefore, we believe that the combination of the ferrocyanide/ferricyanide redox couple with an electrolyte possessing high solvation energy is the reason behind the electrochemical stability of the supercapacitor even when tested at 2.0 V where water molecules would normally decompose.

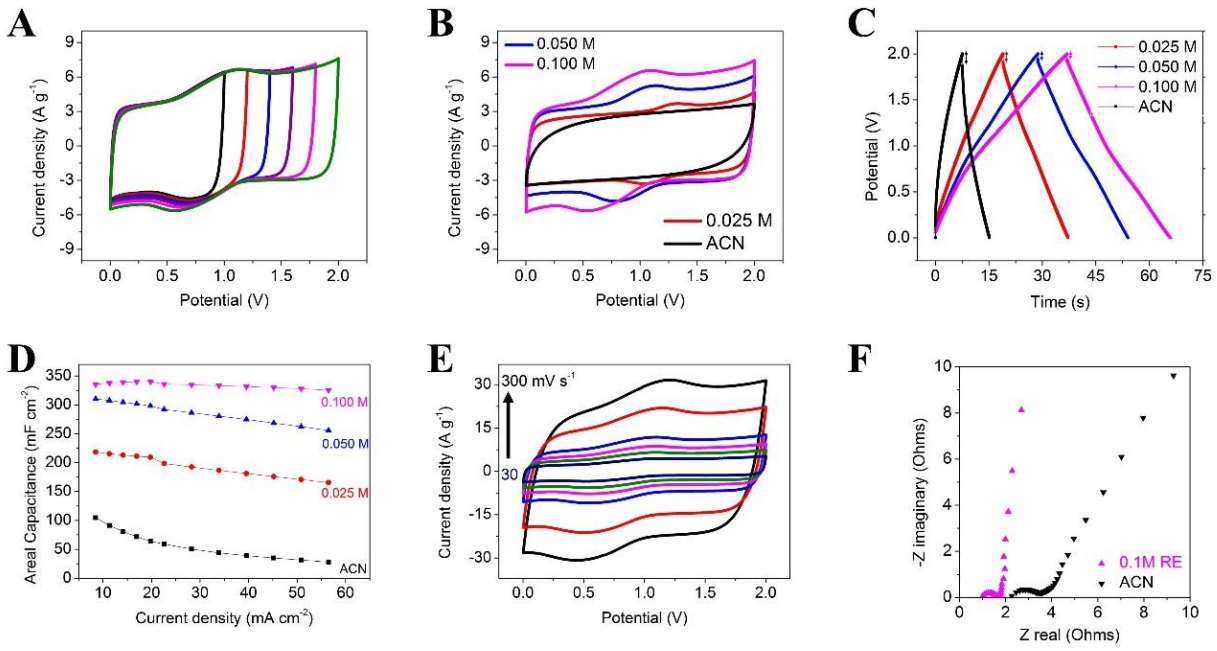

Figure 3.6 Electrochemical performance of a high voltage supercapacitor (SC) in a $[Fe(CN)_6^{3-}/Fe(CN)_6^{4-}]$ redox-active aqueous electrolyte (RE). (A) CV curves of the supercapacitor at an increasing voltage window from 1.0 V to 2.0 V in 0.1 M RE at 50 mV s^{-1}. (B) CV curves collected at increasing concentrations of the redox additive, tested at a scan rate of 50 mV s^{-1}, (C) the corresponding CC curves collected at a current density of 11.3 mA cm^{-2}, (D) specific capacitance by area vs. current density for an activated carbon electrode in a 1.0 M Na_2SO_4 electrolyte containing different concentrations (0, 0.025, 0.050, and 0.100 M) of the redox additive. (E) CV profiles of 0.1M RE-SC at different scan rates of 30, 50, 70, 100, 200, and 300 mV s^{-1}. (F) Nyquist plots of the 0.1 M RE aqueous electrolyte and 1.0 M $TEABF_4$ in acetonitrile supercapacitors over a frequency range of 0.2 MHz to 0.1 Hz. All the electrochemical experiments were measured in a CR2032 coin cell.

Moreover, Figure 3.6A shows a reversible redox couple (between 0.6 V and 1.1 V) which can be attributed to the redox additive. This reaction is described in the following equation 3.1:

$$Fe(CN)_6^{4-} \leftrightarrow Fe(CN)_6^{3-} + e^- \qquad (3.1)$$

At the positive electrode, the electrolyte undergoes an oxidation process from $Fe(CN)_6^{4-}$ to $Fe(CN)_6^{3-}$ during charging, i.e. Fe^{2+} going to Fe^{3+}, conversely at the negative electrode, the discharge process induces reduction from $Fe(CN)_6^{3-}$ to $Fe(CN)_6^{4-}$, i.e. Fe^{3+} going to Fe^{2+}.

We also studied the performance of the supercapacitor at various concentrations of RE, namely 0.025 M, 0.05 M, and 0.1 M and the results are presented in Figure 3.6 B and C, where the results of a traditional acetonitrile-based electrolyte is provided for comparison. With increasing concentration of RE ions, the area under the CV curves (Figure 3.6B) and discharge time of the CC curves (Figure 3.6C) increase, indicating that the specific capacitance increases. By increasing the concentration to 0.2 M, the cell exhibited a 1.2 times increase in capacitance compared to 0.1 M, but the coulombic efficiency dropped to 58% (Figure 3.7). The high leakage current at this high concentration causes the device to take a longer time to reach 2.0 V during charging. Based on these results, the 0.1 M RE system was down selected for further optimization of the overall supercapacitor performance. Not only does the 0.1 M RE system show the highest capacitance, but also it exhibits the best rate capability. Figure 3.6D shows the areal capacitance values extracted from the CC curves obtained at various current densities in the different electrolytes. The 0.1 M RE system shows an ultrahigh areal capacitance of 335 mF cm^{-2} at 8.5 mA cm^{-2} and still retained 325.2 mF cm^{-2} at a higher current density of 56.5 mA cm^{-2}; this is 11.6 times larger than a standard activated carbon system with 1.0 M $TEABF_4$ in ACN electrolyte (Figure 3.6D). Note in Figure 3.6E that the 0.1M RE device maintains a nearly ideal CV shape with increasing scan rate up to 300 mV s^{-1}. More importantly, the curves show distinct and reversible redox peaks at all scan rates, indicating rapid charge transfer between the electrodes and the redox electrolyte. In addition, this redox supercapacitor continues to provide

A

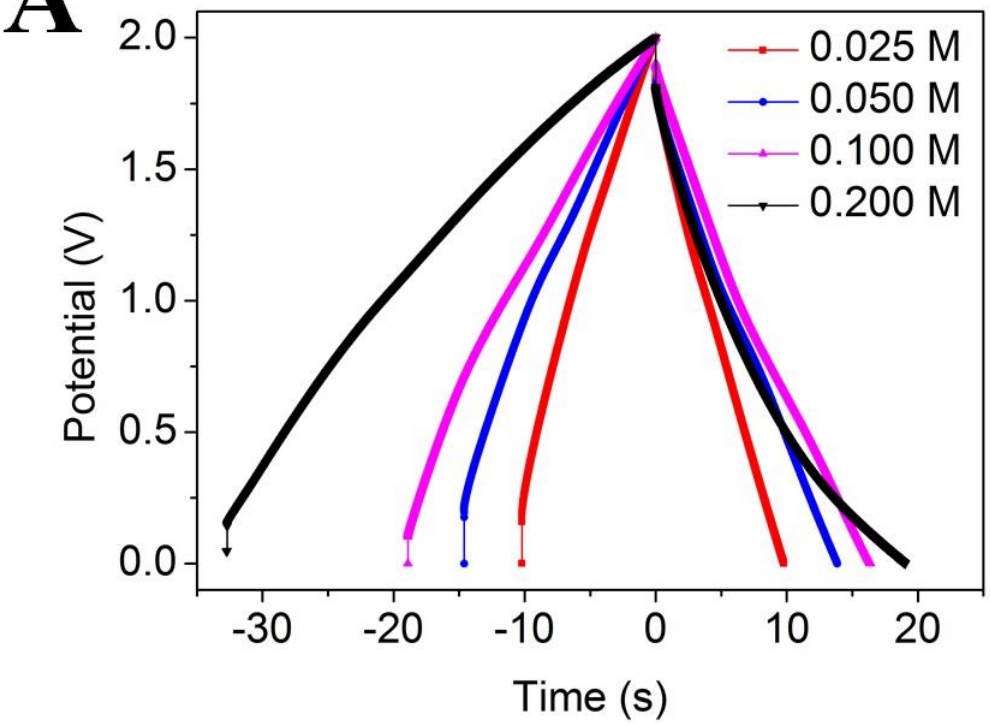

B

Concentraion of RE	Areal capacitance mF cm^{-2}	Coulombic efficiency %
0.025	105	96
0.050	149	95
0.100	170	87
0.200	207	58

Figure 3.7 (A) Charge/discharge (CC) curves at 20 mA cm^{-2} of an activated carbon supercapacitor with 0.025 M (red), 0.050 M (blue), 0.100 M (pink) and 0.200 M (black) of the redox-active electrolyte [$Fe(CN)_6^{3-}/Fe(CN)_6^{4-}$] in 1.0 M Na_2SO_4. (B) Areal capacitance of the device and Coulombic efficiency as listed at different concentrations of redox-active electrolyte are calculated based on the CC results at 20 mA cm^{-2}.

high discharge currents with small IR drops (Figure 3.8 a,b,). These results imply that the 0.1 M RE electrolyte promotes rapid electron transfer and improved rate capability. This fast electron transfer was further confirmed by a Nyquist plot (Figure 3.6F), in the 0.1 M RE-SC system, where the ESR is much lower (1.61 Ω) than in an ACN electrolyte (3.52 Ω). One can conclude that the addition of the RE electrolyte brings about the following advantages: (1) It acts as a solution buffer to maintain neutral pH, allowing the operation of this electrolyte with widely used aluminum current collectors. (2) It extends the operating voltage window up to 2 V in an aqueous electrolyte and effectively increases the energy density. (3) It increases the areal capacitance of the device through fast and reversible Faradaic reactions. (4) It enables fast electron transfer and increased ion conductivity, allowing for higher rate capability and (5) It produces a low ESR.

3.3.4. Synergetic effects from combining laser scribed activated carbon with a redox-active electrolyte

Combining a macro patterned LSAC electrode with ferricyanide/ferrocyanide redox electrolyte produces a synergistic enhancement of the electrochemical performance. The macroporous structure of LSAC allows easy access of the RE ions to the surface of the activated carbon particles and enables fast and reversible redox reactions as well as rapid absorption and desorption as illustrated in Figure 3.9A. Therefore, the combination of a 0.1 M RE electrolyte with the LSAC electrodes is expected to not only boost the energy and power density, but also stabilize the cycle life allowing the operation of the device at a high voltage up to 2.0 V. Note that the 0.1 M RE system exhibits an essentially ideal CV profile with a rectangular shape and distinct redox peaks, whereas the ACN electrolyte system only shows EDLC properties as expected (Figure 3.9B). Furthermore, compared with the 0.1 M RE with non-scribed activated

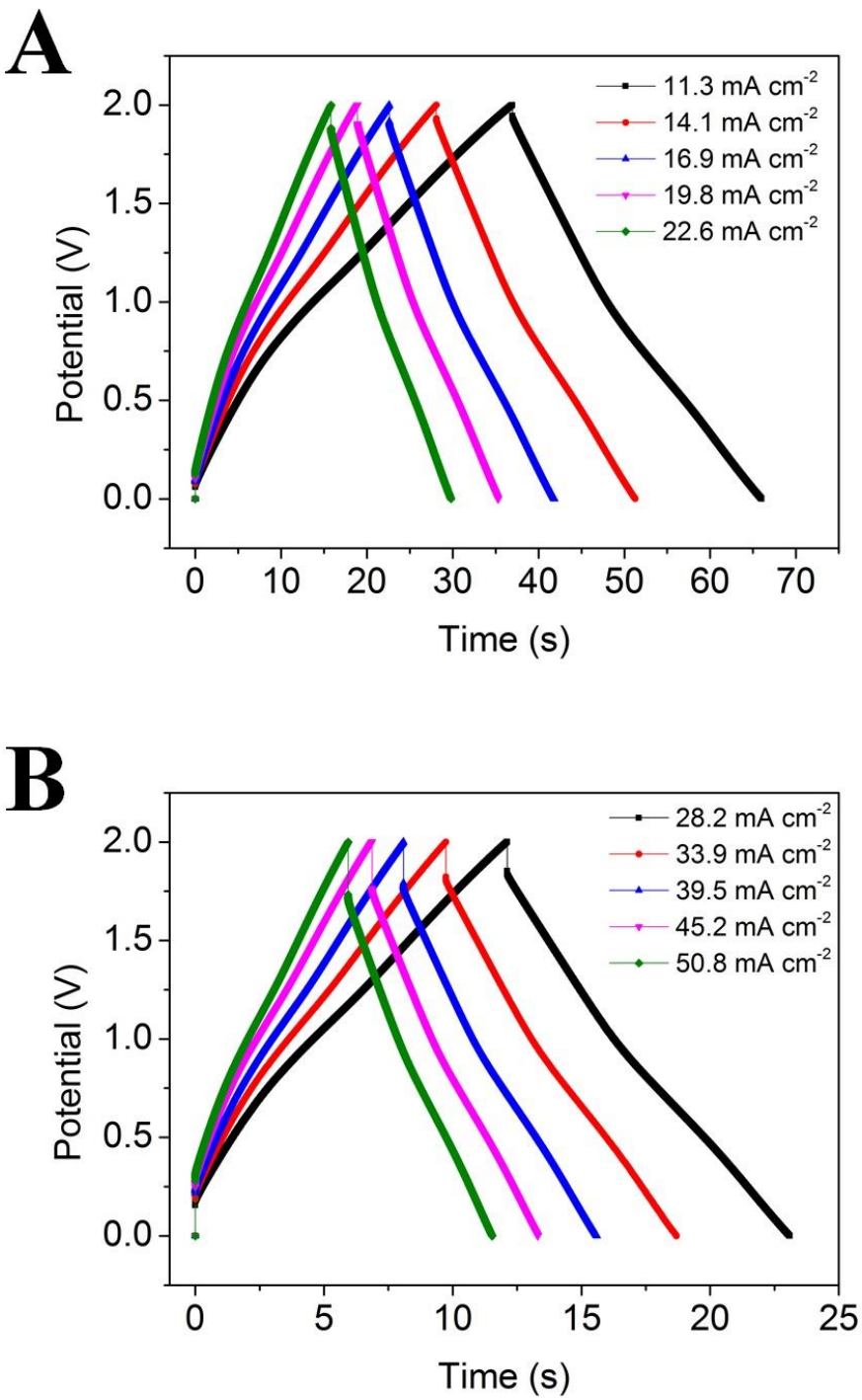

Figure 3.8 CC curves of an activated carbon supercapacitor with 0.10 M redox-active electrolyte at current densities of (A) 11.3, 14.1, 16.9, 19.8 and 22.6 mA cm^{-2}, and (B) 22.8, 33.9, 39.5, 45.2 and 50.8 mA cm^{-2}.

carbon electrodes, the 0.1 M RE-LSAC system shows about a 30% increase in the area of the CV. This suggests that the combination of LSAC electrode with RE can enhance the capacitance through the porous architecture of the electrode, allowing for better exposure of the active materials to the RE ions. Again, both CV and CC curves were collected with an increasing voltage window up to 2 V, tested at a scan rate of 50 mV s^{-1} for CV curves and a current density of 11.3 mA cm^{-2} for CC curves (Figure 3.10 a,b,). This new hybrid (0.1 M RE-LSAC) system was also tested over a wide range of scan rates from 30 to 1000 mV s^{-1} (Figure 3.9C and Figure 3.10C,) and current densities 8.5 to 56.5 mA cm^{-2} (Figure 3.9D and Figure 3.10D,). This hybrid system shows very clear redox peaks up to a high scan rate of 1000 mV s^{-1}, indicating excellent charge storage through ultrafast redox reactions. Changes in the areal capacitances (Figure 3.9E) and gravimetric capacitances (Figure 3.10E,) for all four systems were calculated as a function of the current density for comparison. Not only does the ACN with the non-scribed electrode system show lower capacitance, but the capacitance rapidly drops off at higher rates. Nevertheless, no significant changes can be observed in the capacitance of the hybrid system even at high charge-discharge rates. In order to get a glimpse of the difference between the two cases, the capacitance of the two devices are compared at a relatively high current density of 56.5 mA cm^{-2}. The hybrid system can deliver 364.6 mF cm^{-2}, which is 13 times larger than the capacitance of a traditional supercapacitor using non-scribed activated carbon electrodes and an acetonitrile-based electrolyte (28 mF cm^{-2}). Again, this confirms the improved ion diffusion kinetics within the laser scribed electrodes and the excellent Faradaic capacitance contribution from the redox electrolyte.

The superior synergetic interactions between the laser scribed macroporous electrodes and the 0.1 M RE was further confirmed from electrochemical impedance spectroscopy measurements, showing a low ESR of 0.9 Ω (Figure 3.9F) and a short response time of 1.96 s (Figure 3.10F,)

compared with 1.61 Ω and 3.33 s for a supercapacitor consisting of non-scribed AC electrodes and a 0.1 M RE and 2.6 Ω and 2.07 s for a supercapacitor consisting of LSAC electrodes without a redox additive (not shown).

The impedance of the RE-LSAC supercapacitor reveals a nearly vertical line in the low-frequency region (0.01 Hz), which indicates ideal capacitive behavior of the supercapacitor (Figure 3.10G, Supporting Information). Apparently, the laser scribed electrodes work together with the redox additive towards improving both the ESR of the cell and the response time, which is consistent with the CV and CC results. Our RE-LSAC supercapacitor demonstrated a 1/2 V_{max} (1.0 V) open-circuit voltage that can be maintained for 7 h after being fully charged (to 2.0 V) for 7 hr and also exhibited a low leakage current of 15 μA. This is equivalent to 1.33 μA mg^{-1} of active materials (Figure 3.10H,I,) indicating excellent energy storage performance. This experiment was carried out by applying a direct current of 2.0 V across the supercapacitor and measuring the current required to retain that voltage.

Therefore, the 0.1 M RE-LSAC system shows excellent performance in a Ragone plot when compared with commercially available energy storage devices (Figure 3.9G). This Ragone plot was normalized based on the volume of the full device that included the active material, current collector, separator, and electrolyte. The 0.1 M RE-LSAC supercapacitor can demonstrate 6.2 mWh cm^{-3}, which is about 9 times higher energy density than commercially available activated carbon electrochemical capacitors with an ACN electrolyte. Furthermore, the 0.1 M RE-LSAC can deliver ultrahigh power densities up to 3.6 W cm^{-3}, which is about 700 times faster than a lithium thin-film battery.[18] Therefore, the LSAC electrodes in combination with a 0.1 M RE electrolyte could be an ideal candidate for future energy storage applications.

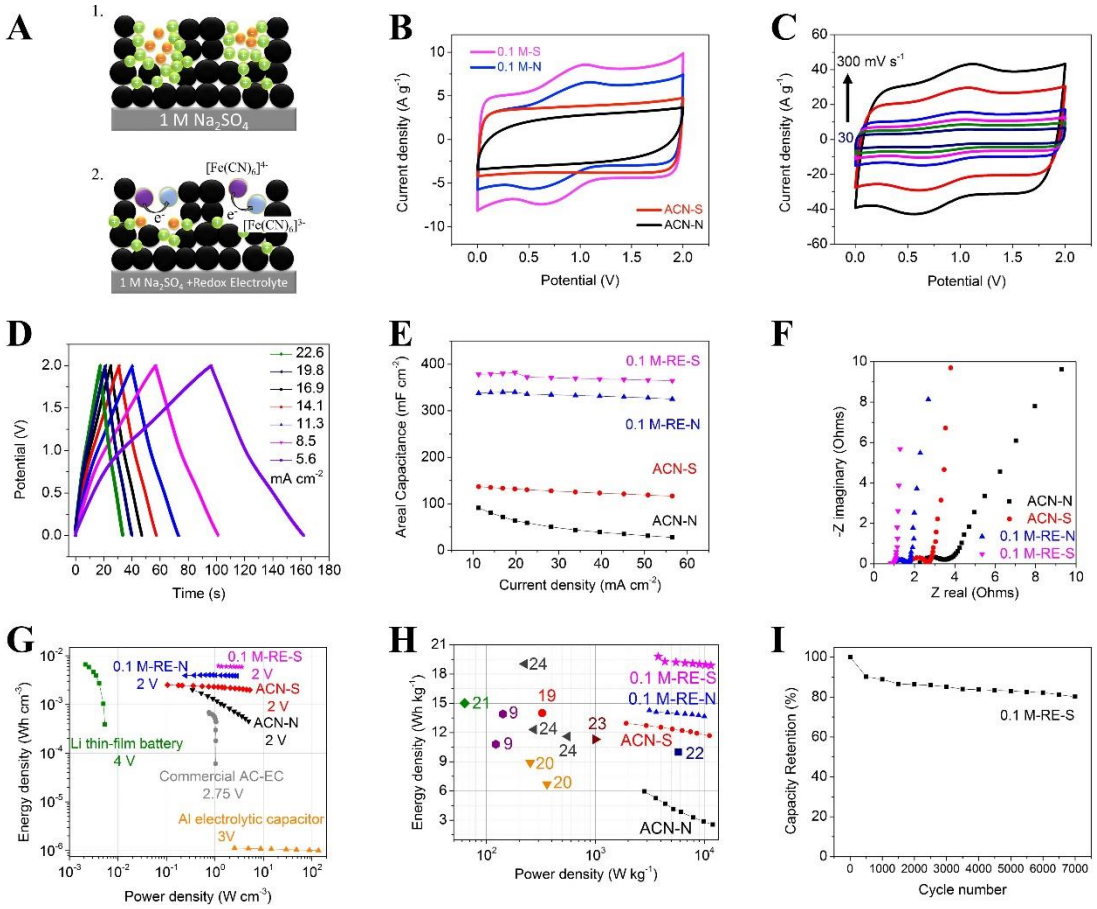

Figure 3.9 Electrochemical performance a supercapacitor combining laser scribed activated carbon (LSAC) electrodes and [$Fe(CN)_6^{3-}$/$Fe(CN)_6^{4-}$] redox-active electrolyte (RE). (A) Illustration of the charge storage mechanism in an LSAC electrode using a 1.0 M Na_2SO_4 electrolyte (1) in the absence, and (2) in the presence of a redox additive. (B) CV profiles comparing the electrochemical performance of activated carbon electrodes before and after laser scribing tested in a traditional 1.0 M acetonitrile electrolyte and in a 0.1 M redox electrolyte with data collected at a scan rate of 50 mV s^{-1}. (C) Evolution of the electrochemical performance of an LSAC supercapacitor using 0.1 M RE at different CV scan rates at 30, 50, 70, 100, 200 and 300 mV s^{-1}, (D) corresponding CC curves at different current densities of 5.6, 8.5, 11.3, 11.4, 16.9, 19.8, 22.6 mA cm^{-2}. (E) Areal capacitance vs. current density and (F) Nyquist plots comparing the

performance of four different cases. (G) Ragone plot comparing the volumetric energy density and power density of the 0.1 M RE-LSAC supercapacitor with commercially available energy storage devices.[18,25] (H) Another Ragone plot showing the gravimetric energy density and power density of the 0.1 M RE-LSAC system and other RE-based supercapacitors reported in the literature.[9,19-24] (I) Long-term cycling stability of 0.1 M RE-LSAC supercapacitor at 2.0 V.

Another Ragone plot based on the total mass of the active materials (Activated carbon and RE electrolyte) was made to compare with previously published RE-based electrolyte supercapacitors (Figure 3.9H).[9,19-24] When compared to previously published data, our supercapacitors lie in the upper-right side of the plot, meaning that both power and energy density are outstanding. Even at a very high power density of 11.5 kW kg^{-1}, our 0.1 M RE-LSAC maintains 95 % (18.9 Wh kg^{-1}) of its original energy density measured at low rates (19.8 Wh kg^{-1}). Since the redox electrolyte contributes to charge storage just like the active electrode material, the mass of the electrolyte was also considered in the calculations. Here, the specific power achieved for a 0.1 M RE-LSAC supercapacitor is 11,516 W kg^{-1} which is 70 times larger than previous reports for an RE-EC.[9] Table S1 provide a summary of the electrochemical data for previously published redox supercapacitors with aqueous electrolytes, the data indicate that the hybrid 0.1 M RE-LSAC system shows a higher voltage window as well.

Good cycle life is an important fundamental property of supercapacitors. In our case, we studied the cycle life of our 0.1 M RE-LSAC supercapacitor by charging and discharging at a current density 30 mA cm^{-2} for 7000 cycles (Figure 3.9I). Compared with a supercapacitor utilizing 1.0 M Na_2SO_4 which loses most of its capacitance in the first 10 cycles, the 0.1 M RE-LSAC supercapacitor maintains 80 % of its original capacity after 7000 cycles at 2.0 V. This

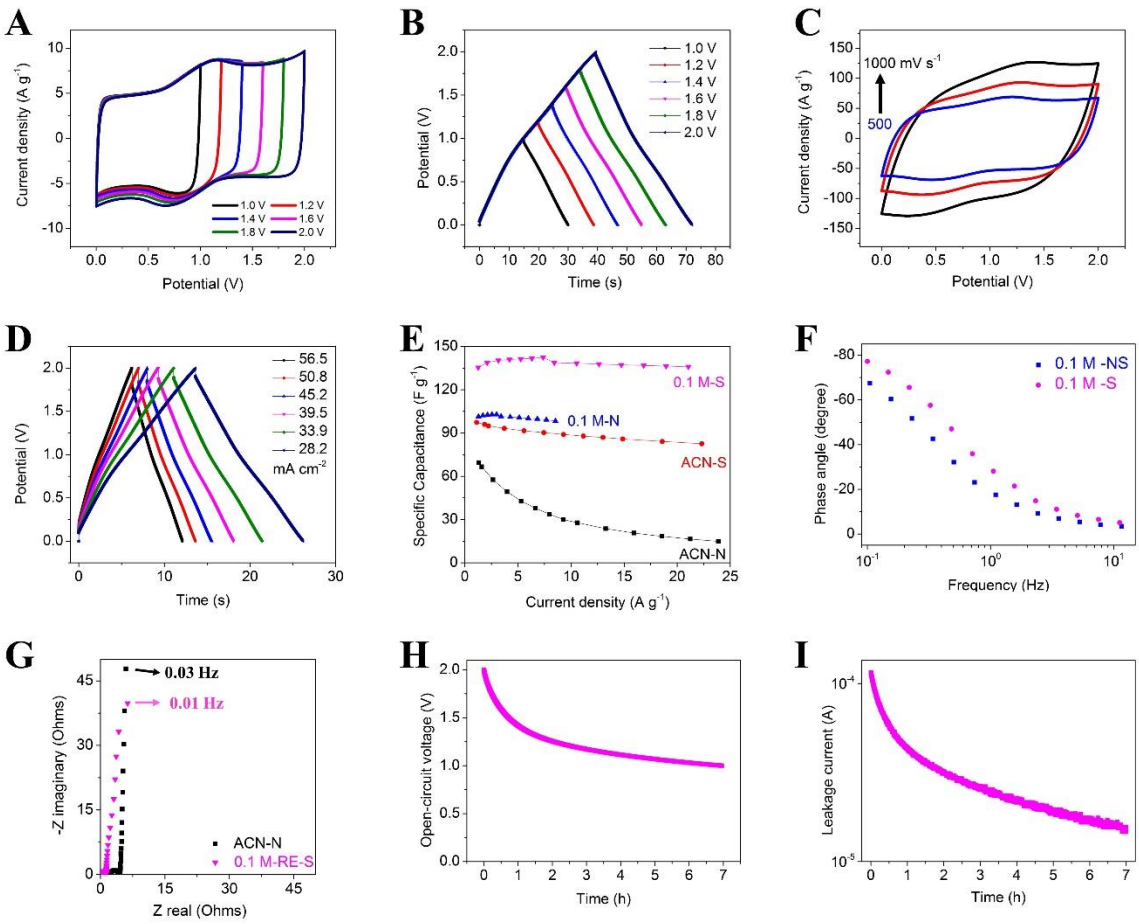

Figure 3.10 Evaluation of the electrochemical performance of laser scribed activated carbon (LSAC) electrodes in a 0.10 M redox-active electrolyte (RE) (A) CV curves at 50 mV s^{-1}, (B) Galvanostatic charge/discharge (CC) curves at a current density of 11.3 mA cm^{-2} with an increasing voltage window from 1.0 V to 2.0 V. (C) CV curves at high scan rates of 500, 700, and 1000 mV s^{-1}. (D) CC curves at current densities of 11.3, 14.1, 16.9, 19.8 and 22.6 mA cm^{-2}. (E) Comparison of gravimetric capacitance per electrode for activated carbon before and after laser scribing, with and without a redox active electrolyte normalized by the active materials (activated carbon + 0.1 M RE). (F) Bode plots of the redox active electrolyte-based supercapacitors before and after laser scribing (i.e. RE-AC and RE-LSAC). (G) Nyquist plots of the RE-LSAC over a frequency range of 0.8 MHz to 0.01 Hz and an activated carbon electrode with acentonitrile

electrolyte over a frequency range of 0.3 MHz to 0.03 Hz. (H) Testing the self-discharge of an RE-LSAC supercapacitor. (I) Leakage current measurement of an RE-LSAC supercapacitor.

outstanding electrochemical stability can be attributed to the redox-electrolyte that not only adds Faradaic capacitance to the cell, but also stabilizes the cycle life of the cell even when operated at an ultrahigh voltage of 2.0 V. These results confirm the synergy between the macroporous activated carbon electrode made by laser scribing and the redox electrolyte through improved ion migration and fast and reversible redox reactions. The microscale channels act as electrolyte reservoirs and tend to reduce the inernal resistance and increase capacitance simultaneously.

3.4 Experimental Section

Preparation and Fabrication of LSAC electrode

Activated carbon electrodes were prepared by making a slurry consisting of activated carbon (MTI Corp, AB-520), a ratio of carboxymethyl cellulose/styrene-butadiene rubber (MTI Corp) as a binder and carbon black (MTI Corp, *TIMICAL SUPER C65*) in deionized water with a weight ratio of 80:10:10, respectively. The slurry was then cast to carbon coated aluminum foil (Exopack, 16 µm), using a doctor blade. This film was dried for 12 h under ambient conditions. The dried film was then exposed to a 7-W CO_2 laser (Full Spectrum Laser H-series) to create an LSAC film. Etching the electrodes with a laser is very fast, reliable and reproducible process.

Fabrication of LSAC Supercapacitor Devices (CR 2032)

The electrodes were assembled in standard CR2032 coin cells using electrode discs (15 mm in diameter) and Celgard 3501 polymer separators. Two different types of electrolytes were utilized the standard 1.0 M tetraethylammonium tetrafluoroborate ($TEABF_4$) in acetonitrile (ACN)

or variable concentrations of [$Fe(CN)_6^{3-}$/$Fe(CN)_6^{4-}$] in 1.0 M Na_2SO_4 solution. All the coin cells were assembled in air. The loading masses of the activated carbon film before and after scribing were 3.9 and 3.2 mg cm^{-2}, respectively. This indicates the increased porosity of the electrode upon laser etching.

3.5 Conclusion

A new method is described to produce macroporous electrodes using a simple laser scribing technique. These electrodes when combined with an aqueous ferrocyanide/ferricyanide redox electrolyte, they create supercapacitors with enhanced energy density enabled by both higher capacitance and a larger potential window. The LSAC has a macro-patterned architecture and improved ion diffusion pathways, which enable the efficient electric double layer capacitance from the active material and Faradaic capacitance from the electrolyte. The synergy between the laser scribed electrodes and the redox electrolyte produce for supercapacitors with 8 times larger capacitance than traditional supercapacitors utilizing non-scribed activated carbon electrodes with an acetonitrile-based electrolyte. In addition, the RE-LSAC system exhibits high rate capability, low ESR, and excellent cycling stability. The new supercapacitor utilizes commercial grade active materials, current collectors and separators and may, thus, have potential for real world applications.

3.6 Appendix to Chapter 3

Supplementary Table S3.1 Comparison of the Voltage Window of 0.1 M redox-activeelectrolyte (RE) with laser scribed activated carbon electrode (LSAC) with other published article using aqueous based redox-active electrolyte

Redox Couple	Based Electrolyte	Voltage	Reference
0.1 M Potassium ferrocyanide ($FeCN_6^{3+}$ /$FeCN_6^{4+}$)	1.0 M Na_2SO_4	2.0 V	This work
0.38 M hydroquinone (Q/HQ)	1.0 M H_2SO_4	1.0 V	3.1
0.3 g $VOSO_4$ (VO^{2+}/VO_2^{+})	1.0 M H_2SO_4	0.8 V	3.2
0.050 g p-phenylenediamine (p-phenylenediamine /p-phenylenediimine)	2.0 M KOH	1.0 V	3.3
0.08 M KI (I^-/I_3^-)	1.0 M H_2SO_4	1.0 V	3.4
0.08 M KI (I^-/I_3^-)	1.0 M Na_2SO_4	1.0 V	
0.08 M KBr (Br^- /Br_3^-)	1.0 M H_2SO_4	1.0 V	
0.06 M $CuCl_2$ (Cu^{2+}/Cu)	1.0 M HNO_3	1.35 V	3.5
0.4 M hydroquinone (Q/HQ)	1.0 M H_2SO_4	0.8 V	3.6
0.4 M $CuSO_4$ (Cu^{2+}/Cu)	1.0 M H_2SO_4	0.8 V	
1 M KI and 1 M $VOSO_4$ (I^-/I_3^- and VO^{2+}/VO_2^{+})		0.8 V	3.7
0.4 M KBr/0.1 M $HVBr_2$ (Br^- /Br_3^- and HV^{2+}/HV^{+})		1.2 V	3.8
1 M KBr/0.5 M $MVCl_2$ (Br^- /Br_3^- and MV^{2+}/MV^{+})		1.4 V	

Calculations

The specific capacitance, energy density and power density of the full device were calculated from the charge/discharge curves at different current densities.

First, the specific capacitance of the device was calculated, and the time and the voltage were measured from the discharge curve:

$$\text{Specific C}_{\text{device}}\,(\text{F g}^{-1}) = \frac{2*\text{I (A)}*\int U(\text{t})\text{dt(Volt)(sec)}}{U^2*Mass(g)}$$

Mass refers to the mass of the active materials (activated carbon + 0.1 M potassium ferrocyanide)

$$\text{Specific C}_{\text{device}}\,(\text{F cm}^{-3}) = \frac{2*\text{I (A)}*\int U(\text{t})\text{dt(Volt)(sec)}}{U^2*Volume\ (cm^3)}$$

Volume refers to the volume of the stack device including the active materials, substrates and separator.

Second, the specific capacitance of the electrode was calculated from the full cell.

$$\text{Specific C}_{\text{electrode}}\,(\text{F g}^{-1}) = 4*\text{C}_{\text{device}}\,(\text{F g}^{-1})$$

Third, the specific energy density of the device was calculated from:

$$\text{Specific E}_{\text{device}}\,(\text{Wh kg}^{-1}) = \frac{\text{I(A)}\int U(\text{t})\text{dt(Volt)(hr)}}{Mass(kg)}$$

Mass refers to the mass of active materials (activated carbon + 0.1 M potassium ferrocyanide)

$$\text{Specific E}_{\text{device}}\,(\text{Wh cm}^{-3}) = \frac{\text{I(A)}\int U(\text{t})\text{dt(Volt)(hr)}}{volume(cm^3)}$$

Volume refers to the volume of the stack device including the active materials, substrates and separator.

Fourth, the specific power density of device was calculated from:

$$\text{Specific P}_{\text{device}}\,(\text{W kg}^{-1}) = \frac{\text{Energy density}(Wh/kg)}{Time(\text{hr})}$$

$$\text{Specific P}_{\text{device}}\ (\text{W cm}^{-3}) = \frac{\text{Energy density}(Wh/cm^3)}{Time(\text{hr})}$$

3.7 References

(1) El-Kady, M. F.; Shao, Y.; Kaner, R. B. Graphene for batteries, supercapacitors and beyond *Nat. Rev. Mater.* **2016**, *1*, 16033.

(2) Weinstein, L.; Dash, R. Supercapacitor carbons. *Mater. Today* **2013**, *16*, 356-357.

(3) Miller, J. R. Valuing reversible energy storage *Science* **2012**, *335*, 1312-1313.

(4) Dura, H.; Perry, J.; Lecacou, T.; Markoulidis, F.; Lei, C.; Khalil, S.; Decker, M.; Weil, M. International Conference on Clean Electrical Power (ICCEP), Alghero, Italy, June, **2013**.

(5) Burke, A. R&D considerations for the performance and application of electrochemical ca pacitors. *Electrochim. Acta* **2007**, *53*, 1083-1091.

(6) He, M.; Fic, K.; Frckowiak, E.; Novak, P.; Berg, E. J. Ageing phenomena in high-voltage aqueous supercapacitors investigated by in situ gas analysis. *Energ. Environ. Sci.* **2016**, *9*, 623-633.

(7) El-Kady, M. F.; Ihns, M.; Li, M.; Hwang, J. Y.; Mousavi, M. F.; Chaney, L.; Lech, A.T.; Kaner, R. B. Engineering three-dimensional hybrid supercapacitors and microsupercapaci tors for high-performance integrated energy storage. *Proc. Natl. Acad. Sci. U.S.A.* **2015**, *1 12*, 4233-4238.

(8) Hwang, J.Y.; El-Kady, M.F.; Wang, Y.; Wang, L.; Shao, Y.; Marsh, K.; Ko, J.M.; Kaner, R.B. Direct preparation and processing of graphene/RuO_2 nanocomposite electrodes for high-performance capacitive energy storage. *Nano Energy* **2015**, *18*, 57.

(9) Chun, S.E.; Evanko, B.; Wang, X.; Vonlanthen, D.; Ji, X.; Stucky, G.D.; Boettcher, S.W. Design of aqueous redox-enhanced electrochemical capacitors with high specific energies and slow self-discharge. *Nat. Commun*. **2015**, *6*.

(10) Fic, K.; Lota, G.; Meller, M.; Frackowiak, E. Novel insight into neutral medium as

electrolyte for high-voltage supercapacitors. *Energ. Environ. Sci.* **2012**, *5*, 5842-5850.

(11) Lee, D.; Patwa, R.; Herfurth, H.; Mazumder, J. High speed remote laser cutting of electrodes for lithium-ion batteries: Anode. *J. Power Sources* **2013**, *240*, 368-380.

(12) El-Kady, M.F.; Kaner, R.B. Direct laser writing of graphene electronics. *ACS Nano* **2014**, *8*, 8725-8729.

(13) Maciá-Agulló, J.A.; Moore, B.C.; Cazorla-Amorós, D.; Linares-Solano, A. Activation of coal tar pitch carbon fibres: physical activation vs. chemical activation. *Carbon* **2004**, *42*, 1367-1370.

(14) Gogotsi, Y.; Simon, P. True performance metrics in electrochemical energy storage. *Science* **2011**, *334*, 917-918.

(15) Yang, X.; Cheng, C.;Wang, Y.,; Qiu, L.; Li, D. Liquid-mediated dense integration of graphene materials for compact capacitive energy storage. *Science* **2013**, *341*, 534-537.

(16) Wu, J.; Yu, H.; Fan, L.; Luo, G.; Lin, J.; Huang, M. A simple and high-effective electrolyte mediated with p-phenylenediamine for supercapacitor. *J. Mater. Chem.* **2012**, *22*, 19025-19030.

(17) Mai, L.Q.; Minhas-Khan, A.; Tian, X.; Hercule, K.M.; Zhao, Y.L.; Lin, X.; Xu, X. Synergistic interaction between redox-active electrolyte and binder-free functionalized carbon for ultrahigh supercapacitor performance.*Nat. Commun*. **2013**, *4,* 2923.

(18) Pech, D.; Brunet, M.; Durou, H.; Huang, P.; Mochalin, V.; Gogotsi, Y.; Taberna, P.L.; Simon, P. Ultrahigh-power micrometre-sized supercapacitors based on onion-like carbon. *Nat. Nanotechnol.* **2010**, *5*, 651-654.

(19) Senthilkumar, S.T.; Selvan, R.K.; Ponpandian, N.; Melo, J.S.; Lee, Y.S. Improved performance of electric double layer capacitor using redox additive (VO^{2+}/VO_2^{+}) aqueous

electrolyte. *J. Mater. Chem. A* **2013**, *1*, 7913-7919.

(20) Chen, L.; Bai, H.; Huang, Z; Li, L. Mechanism investigation and suppression of self-discharge in active electrolyte enhanced supercapacitors. *Energ. Environ. Sci.* **2014**, *7*, 1750-1759.

(21) Tomai, T.; Mitani, S.; Komatsu, D.; Kawaguchi, Y.; Honma, I. Metal-free aqueous redox capacitor via proton rocking-chair system in an organic-based couple. *Sci. Rep.* **2014**, *4*, 3591.

(22) Yu, H.; Fan, L.; Wu, J.; Lin, Y.; Huang, M.; Lin, J.; Lan, Z. Redox-active alkaline electrolyte for carbon-based supercapacitor with pseudocapacitive performance and excellent cyclability. *RSC Adv.* **2012**, *2*, 6736-6740.

(23) Yu, H.; Wu, J.; Fan, L.; Lin, Y.; Xu, K.; Tang, Z.; Cheng, C.; Tang, S.; Lin, J.; Huang, M.; Lan, Z. A novel redox-mediated gel polymer electrolyte for high-performance supercapacitor. *J. Power Sources* **2012**, *198*, 402-407.

(24) Senthilkumar, S.T.; Selvan, R.K.; Lee, Y.S.; Melo, J.S. Electric double layer capacitor and its improved specific capacitance using redox additive electrolyte. *J. Mater. Chem. A* **2013**, *1*, 1086-1095.

(25) El-Kady, M.F.; Strong, V.; Dubin, S.; Kaner, R.B. Laser scribing of high-performance and flexible graphene-based electrochemical capacitors. *Science* **2012**, *335*, 1326-1330.

(26) Roldán, S.; Blanco, C.; Granda, M.; Menéndez, R.; Santamaría, R. Towards a Further Generation of High-Energy Carbon-Based Capacitors by Using Redox-Active Electrolytes.*Angew. Chem. Int. Ed.* **2011**, *50*, 1699-1701.

(27) Frackowiak, E.; Fic, K.; Meller, M.; Lota, G. Electrochemistry Serving People and Nature: High-Energy Ecocapacitors based on Redox-Active Electrolytes. *ChemSusChem*. **2012**, *5*, 1181-1185.

CHAPTER 4

Integration of a Porous PVDF Separator for a Self-charging Supercapacitor

4.1 Abstract

Due to the miniaturization in the electronics industry, there has been an increasing demand for reliable portable power sources. Among all the power systems, self-charging power units comprised of piezoelectric materials and energy storage devices have attracted a lot of attention due to their ability to convert and store human biomechanical energy. Although piezoelectric materials with good performance are used as the separator for the power units, there is not much effort to improve the electrochemical performance of the energy-storage part. Nonporous piezoelectric films without pore structure are utilized, hindering the ion diffusion process in the cell, resulting in poor cell performance. In this work, we used zinc oxide nanoparticles as the sacrifice template to fabricate porous piezoelectric film for applications as supercapacitor separators. Thanks to the well-designed pore structure and pore volume, the film shows a dramatic decrease in ion diffusion resistance compared to a nonporous film, while retaining its good piezoelectric properties. Attributed to the interconnected pore structure, the performance of our separator is even comparable to a commercial polyethylene (PE) separator. With a conducting polymer as the electrode material and polyvinyl alcohol (PVA)/H_2SO_4 as the gel electrolyte, the self-charging power unit is able to go over 0.2 V simply by palm pressing.

4.2 Introduction

The global market for small electronic devices such as phones, biomedical devices[1-2] and light-emitting diodes (LEDs)[3] has grown rapidly in recent years. Due to the downsizing of devices, reliable supplies of light weight and sustainable power sources are in urgent demand. As a result,

there have been numerous research efforts on self-powered units that integrate energy conversion and energy storage components[4-6] into a single device. Piezoelectric materials such as ZnO,[7] GaN[8] and polyvinylidene fluoride (PVDF)[9] are promising candidates for energy harvesting since they are capable of generating electricity from the ambient environment. As long as there are deformations or vibrations on a piezoelectric material, there will be ion displacement in the crystal structure, leading to electric polarization of the unit cell.[10] Since the crystal structure is periodic, the polarization will accumulate and a potential difference between certain crystal faces will appear. In this way, the materials can scavenge energy from fluid flow or even human biomechanical movements. Among all the materials, PVDF has a high piezoelectric[11] coefficient and is flexible in nature, which is ideal for use in these devices. Meanwhile, lithium ion batteries and supercapacitors are well studied as the energy storage part of the self-powered device. Xue *et al*.[12] from Zhong Lin Wang's group proposed a novel hybrid system based on a conventional lithium ion battery and a PVDF separator. For the typical self-charging process, a piezopotential will be generated by a compressive strain, driving the lithium ion migration and redox reaction on the electrodes. In this way, the mechanical energy can be saved in the lithium ion battery electrochemically for further use in nanoscale or microscale devices. To overcome the inherent low power density and poor cycle life of lithium ion batteries, the same group used an MnO_2 supercapacitor as the energy storage part for another project.[13] By replacing the regular polyethylene (PE) separator with the PVDF-ZnO film, the device can be charged to 110 mV with palm pressing.

Although the PVDF based films from the group showed decent piezoelectric performance, there was little attention paid to the porosity of the separator film. The cyclic voltammetry (CV) curves of the MnO_2 supercapacitor[13] did not display an ideal rectangular shape, indicating a slow

ion migration process. This is because nonporous separators were utilized, which caused the poor ion diffusion in the energy storage devices, leading to poor electrochemical performance of the cells. In order to improve the performance of the device, a piezoelectric separator with well-aligned pore structure should be applied instead.

Herein, we propose the idea of synthesizing a porous PVDF separator to enhance the performance of energy storage devices. The film can be fabricated via blade casting a mixture of PVDF and ZnO onto the substrate, followed by removal of the metal oxide using acid etching. The ZnO particles function as a sacrificial template to enable the formation of the pore structure in the separator film. With well controlled pore volume and pore size, the ion diffusion performance of our PVDF films are comparable with commercial PE separators, which is desirable for applications in supercapacitors. Another advantage to using ZnO rather than other metal oxides is its ability to improve the piezoelectric performance of the PVDF film. Wurtzite type ZnO itself is a piezoelectric material, which has intrinsic polar surfaces.[14] It could interact with the polymer and induce the formation of the β-phase of PVDF, which is piezoelectrically active. Thanks to ZnO, the PVDF films we fabricated showed good piezoelectric responses. With polyaniline (PANI) as the electrodes and (PVA)/H_2SO_4 as the electrolyte, our power unit was able to be charged to 0.2 V by palm pressing, which is promising for real world applications.

4.3 Results and Discussion

4.3.1 Fabrication of PVDF films with diverse pore sizes

In order to get the optimal electrochemical performance from the PVDF separator, it is of great significance to control the pore size of the polymer film. Since the dimensions of a pore is defined by the size of the sacrificial template, we utilized ZnO particles with three distinct sizes to

synthesize PVDF with different pore structures. The largest ZnO particle has a size around several micrometers (Micro), the medium one is about 100 nm (Sigma), while the smallest particle is less than 50 nm (Nanomat). Because one important role of the ZnO is to induce the β phase of PVDF, the crystal structure of all three types of ZnO were studied in advance by X-ray diffraction (XRD) as shown in Figure 4.1. The XRD patterns of the ZnO particles not only share the same peak positions, but also have similar intensity ratios with the standard ZnO JSPDS pattern[15], confirming that the piezoelectric active material is wurtzite type. Interestingly, a peak broadening phenomenon is also observed with decreasing particle size.

According to the scheme in Figure 4.2A, the PVDF and ZnO powders are dispersed in N,N-dimethylformamide (DMF) under heat with a weight ratio of 2 to 1. When a homogeneous polymer/metal oxide composite is approached, it is cast onto a glass substrate and dried in an oven. The digital image of a PVDF/ ZnO mixture is shown in Figure 4.3B, the white color is due to the metal oxide added. An acid etching method is applied afterwards to remove the metal oxide and leave the porous structure in the PVDF film. Since the pores in the film will reflect light in all directions, an opaque film is observed for the porous PVDF as displayed in Figure 4.3C, which is different from the transparent nonporous PVDF film in Figure 4.3A. Figure 4.2C and 4.2F are the top-view and cross-sectional SEM images of the PVDF/micro-sized ZnO mixture before acid processing. A rough texture of the composite can be observed clearly due to the addition of the inorganic sacrificial template. This is clearly different from Figure 4.2B and 4.2E which are the SEM images of the pure PVDF films that were made by dissolving the polymer into DMF. Without the ZnO particles, the pure PVDF films display a smooth appearance in both top-view and cross-sectional pictures. Figure 4.2D and 4.2G are the images of the porous PVDF after acid etching. Pores can be seen on the surface of the separator Figure 4.2D, while the pore structure is even

clearer from the cross-section image. Figure 4.2G exhibits an interconnected pore network in the PVDF film, which provides efficient diffusion pathways for the electrolyte ions, leading to improved ion migration in the supercapacitor.

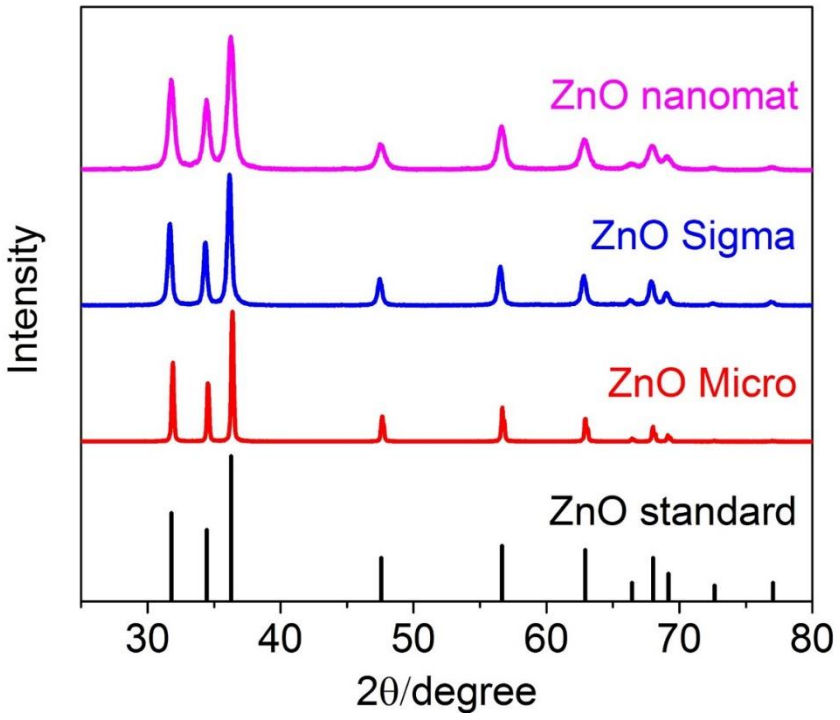

Figure 4.1 X-ray diffraction patterns comparing three different ZnO powders with diverse particle sizes. All the ZnO particles are of the wurtzite structure, which is piezoelectric. The peak width broadening phenomenon is also observed with decreasing size of the ZnO particles.

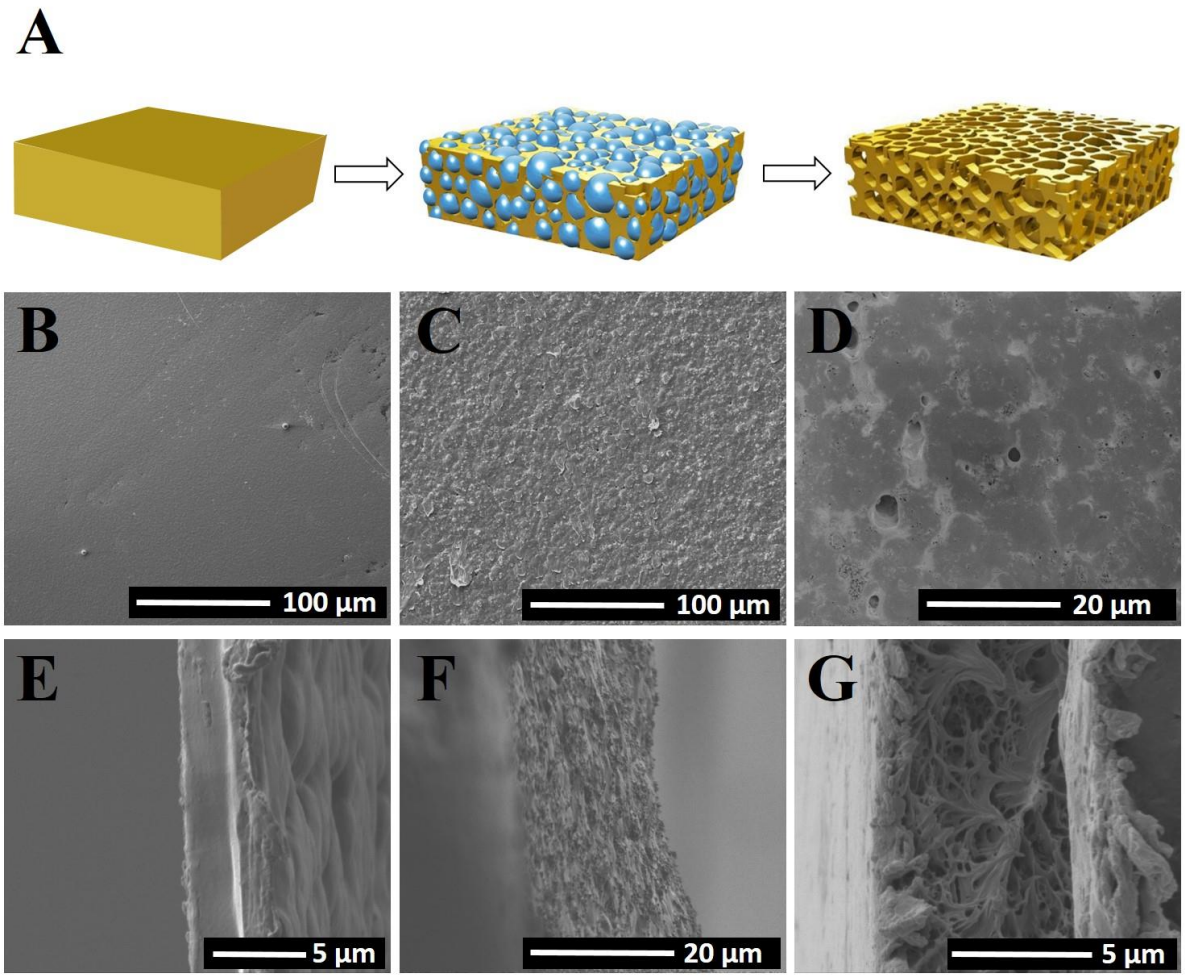

Figure 4.2 (A) Schematic illustration showing the synthesis of a porous PVDF separator: ZnO particles are added into the PVDF matrix and afterwards etched away by acid to create the pore structure. (B) Top-view and (E) cross-sectional SEM images of pure PVDF film with a smooth surface. No pore structure is observed. (C) Top-view and (F) cross-sectional SEM images of the PVDF imbedded with ZnO particles. The particles increase the roughness of the composite film. (D) Top-view and (G) cross-section SEM images of the porous PVDF films after the removal of ZnO particles, displaying a well-aligned pore structure.

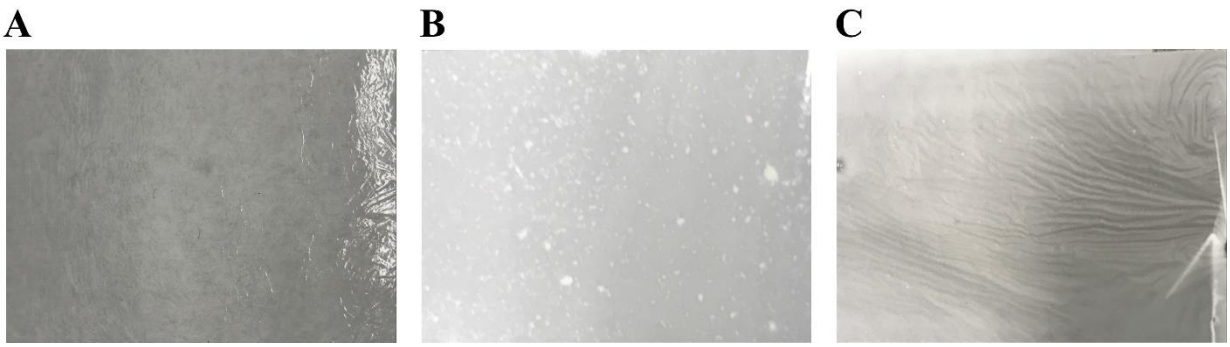

Figure 4.3 Digital images of (A) nonporous PVDF, (B) PVDF embedded with ZnO particles and (C) porous PVDF after the ZnO is etched away. As the images show, the nonporous PVDF is transparent, while PVDF with ZnO is white due to the color of the added ZnO particles. After removal of the ZnO, the porous PVDF film is semitransparent.

The electrochemical properties of the porous films were evaluated without active material as presented in Figure 4.4. Figure 4.4A is the electrochemical impedance spectroscopy (EIS) comparing the porous PVDF separators made from three ZnO powders with different particle sizes. It is apparent that the separator film made with the largest ZnO has the lowest equivalent series resistance (ESR) when compared with the other two in the figure. This can be explained using Figure 4.5. Figure 4.5A and 4.5D are of PVDF made with 50 nm ZnO, while 4.5B and 4.5E are made with 100 nm ZnO. All these films show a segregated pore structure, which could prevent the electrolyte ions from diffusing freely and cause the poor electrochemical performance of the supercapacitors. It is because nanosized ZnO has a large surface area, the particles tend to aggregate to minimize their surface energy, leading to an inhomogeneous embedding in the polymer matrix. Some of the ZnO particles are even isolated and they will then be difficult to etch away. As a result, it is very hard to get the desired pore structure with the current amount of

nanosized metal oxides. When the size of the ZnO increases, they are then able to distribute more evenly and form an interconnected pore network as Figure 4.5C and 4.5F demonstrate. In addition, the electrochemical performance of the three different films are studied using activated carbon electrodes. Similar results are achieved in Figure 4.6 showing that the microporous PVDF not only exhibits better ESR, but also shows improved cyclic voltammetry (CV) and capacitance compared to the other two films. Besides, we carried out EIS measurements on pure PVDF and commercial PE separators to compare with our best porous PVDF film in Figure 4.4B. The pure PVDF film displays a poor ESR performance, while our porous film is comparable to the commercial PE separator thanks to its well-aligned pore structure, which is ideal for separator applications.

Since the piezoelectric performance of the PVDF is the driving force for the self-charging power unit, it is critical for the film to have good potential response to mechanical deformation. The electromechanical properties of the film are measured by using a sandwich configuration as Figure 4.7A reveals. Copper tape is used both on the top and the bottom of the PVDF film as a current collector. The open circuit voltage of the device is record by a potentiostat when mechanical forces are applied through palm impact. The results of the PVDF made with ZnO Nanomat, ZnO Sigma and ZnO Micro are plotted in Figure 4.8A, 4.8B and 4.8C, respectively. The potential generated by 50 nm ZnO is 6 V, which is superior to the other two

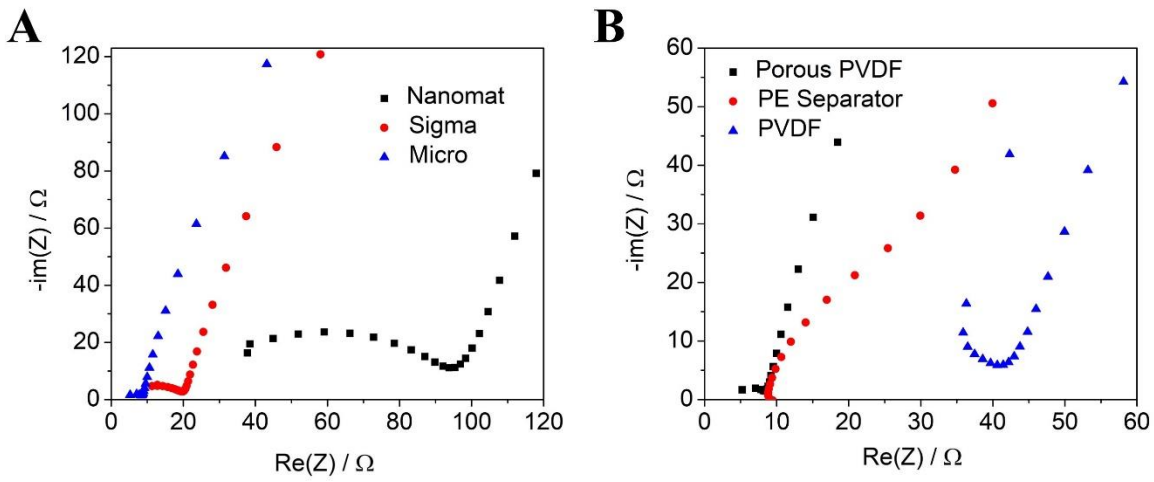

Figure 4.4 (A) Electrochemical impedance spectra (EIS) of the porous PVDF films, indicating that a lower resistance is achieved when ZnO with larger particle sizes are utilized. The experiment is carried out in a coin cell with porous PVDF as the separator. No active material is used. (B) The EIS performance of the porous PVDF made from micro-sized ZnO is comparable with commercial PE separators and is much better when compared with nonporous PVDF film. This indicates that the pore structure in the PVDF film is of great importance for separator applications.

films (3 V for ZnO Sigma and 1 V for ZnO Micro). Besides, this value is also better than many published literature values for PVDF, such as PVDF nanofibers[16] PVDF mats[17] and porous PVDF[18]. The piezoelectric performance is closely related to the amount of β phase PVDF in the polymer film. Although all three films contain the β phase PVDF as the 20° peak[19] indicates in the XRD spectra in Figure 4.9, the ratio of the piezoelectric active content is not the same. The PVDF derived from ZnO Nanomat in the Fourier transform infrared spectroscopy (FTIR) in

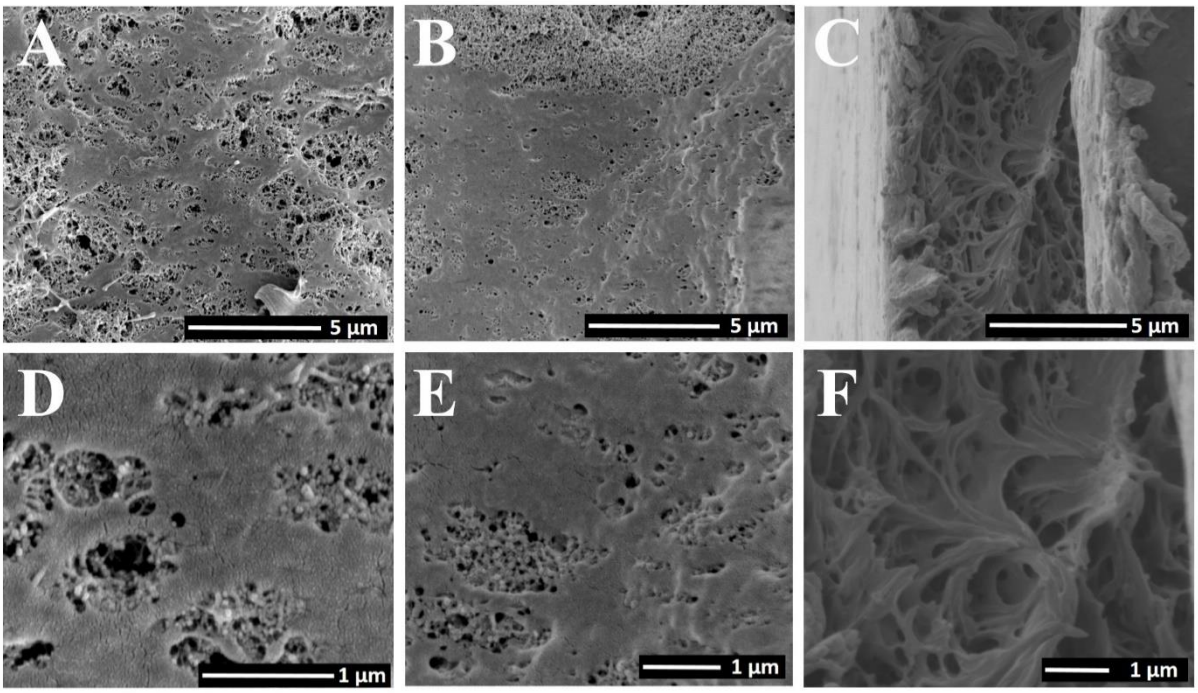

Figure 4.5 (A) and (D) Cross-section SEM images of the PVDF film made from ZnO particles with sizes less than 50 nm. (B) and (E) Cross-section SEM images of the PVDF film made from ZnO particles with sizes less than 100 nm. A disconnected pore structure is seen from the films made with nano-sized ZnO, which will hinder the ion diffusion process through the separator. (C) and (F) Cross-section SEMs image of the PVDF film made from ZnO particles with sizes less than 5 µm. An interconnected pore structure is created which allows electrolyte to diffuse freely through the network.

Figure 4.8D exhibits higher and sharper characteristic peaks[20-21] for the β phase around 510, 840, and 1280 cm^{-1} than the other two films (Figure 4.8E and 4.8F), which is proof that smaller ZnO particles are capable of inducing more β phase PVDF. The mechanism of the β phase PVDF formation is called surface charge induced crystallization.[22-23] More specifically, according to

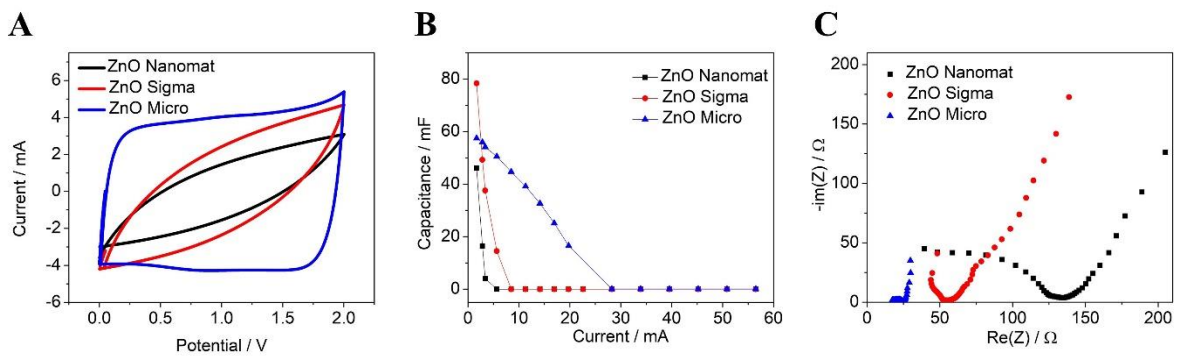

Figure 4.6 (A) CV curves comparing porous PVDF separators made with different sizes of ZnO (50%). The shape of the CV becomes more rectangular with increasing size of ZnO added. This is because there will be a more open pore structure with larger ZnO templates which facilitate the ion diffusion processes. (B) Similar with CV performance, the areal capacitance retention ratio is higher with a more interconnected pore structure at larger current densities. (C) The resistance of the cell decreases when larger ZnO particles are used.

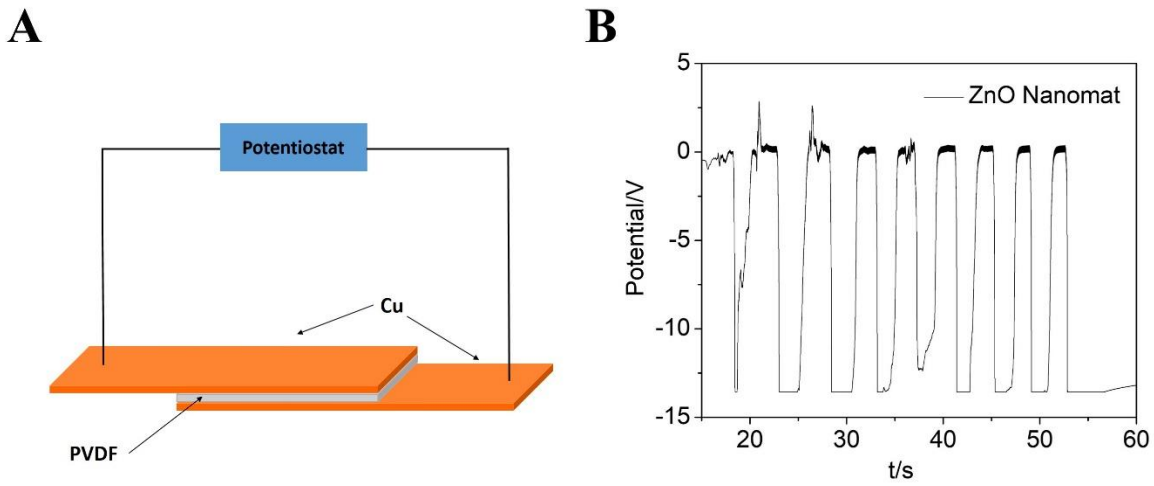

Figure 4.7 (A) Copper tape was used both on the top and the bottom current collectors to test the piezoelectric performance. (B) The piezoelectric performance of the porous PVDF is not hindered when the ratio of ZnO is increased from 50% to 100%.

Wang *et al*.,[24] Zn^{2+} on the (0001) face of the wurtzite type ZnO causes it to be positively charged while the oxygen dominated $(000\bar{1})$ face is negatively charged. The surface charges from the ZnO will interact with the dipoles from PVDF and lead to the formation of the β phase of PVDF. Owing to the small particle size of the ZnO Nanomat, it has a large surface area to interact with PVDF which enables the production of piezoelectric active β phase PVDF. This explains the good piezoelectric performance of the PVDF film made from 50 nm ZnO.

4.3.2 Improving the ion diffusion process of PVDF separators by rational design of the pore volume

For application of the self-charging supercapacitor, both good piezoelectric and ion migration characteristics are needed from the separator. However, we've learned from the previous section that ZnO of larger size is beneficial for creating an interconnected pore structure to provide efficient ion pathways, while the smaller sized metal oxide is able to induce more piezoelectric active β phase PVDF due to its larger surface area. To achieve good piezoelectric and ion diffusion performance simultaneously, we investigated the possibility to enhance the performance of PVDF films made from ZnO Nanomat through increasing its pore volume.

More pore volume in the polymer film can be realized by raising the percentage of ZnO in the PVDF/ZnO mixture. Instead of a weight ratio of 2:1, we utilized an equal amount of the metal oxide and the polymer to make the film (Nanomat 100%). The new film exhibits a much low ESR than the former one (Nanomat 50%) as shown in Figure 4.10A while its piezoelectric performance is not impaired (Figure 4.7B). The ESR drops sharply from over 90 Ω to around 10

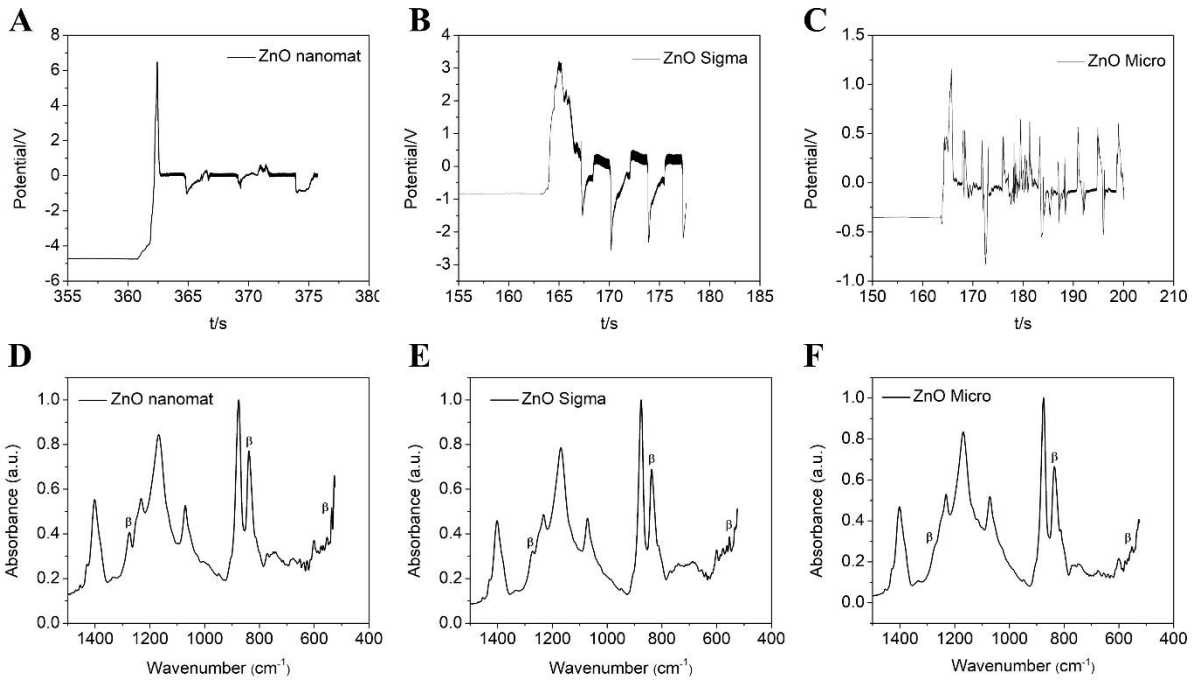

Figure 4.8 (A), (B), (C) Piezoelectric response of the PVDF films made with different-sized ZnO particles. A higher response voltage is acquired from the one made with nano-sized particles. (D), (E), (F) FTIR spectra of the three films made with different ZnO's. It shows that the smaller the ZnO particle is, the more β form the film will get, which is beneficial for good piezoelectric performance.

Ω simply by introducing more sacrificial reagents. Since there are more ZnO nanoparticles in the composite, they are less likely to be isolated by the polymer and will form a connected metal oxide network. When the acid is applied, the ZnO can be etched away easily and leave an interconnected pore structure in the PVDF separator.

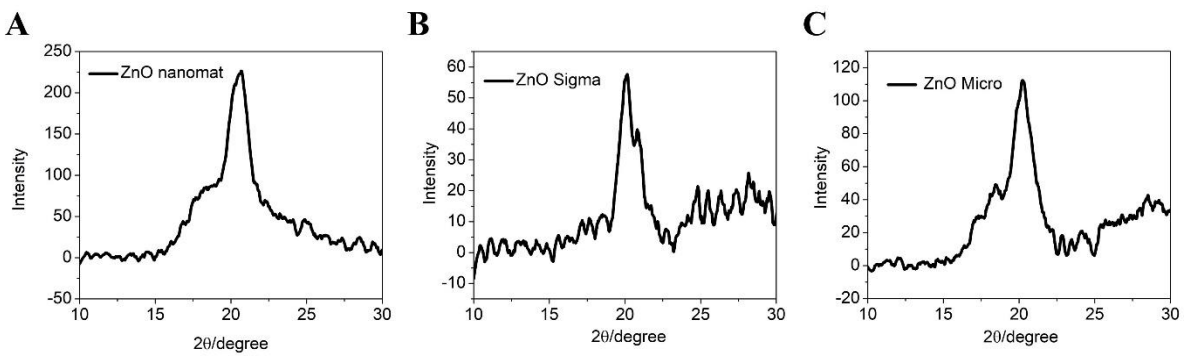

Figure 4.9 XRD patterns of the porous PVDF films made from three different types of ZnO particles: (A) ZnO with particle sizes less than 50 nm, (B) ZnO with particle sizes less than 100 nm and (C) ZnO with particle sizes less than 5 μm. The peak for β form PVDF at 20 degrees is observed in all three spectra.

Consistent with its ion diffusion performance, the porous PVDF also shows improved electrochemical properties in an activated carbon supercapacitor (Figure 4.10B-4.10D). Similarly, the ESR of the cell with Nanomat 100% separator is as low as 8 Ω as seen from the inset in Figure 4.10B because of the increased pore volume, which is much smaller than the device with Nanomat 50%. Moreover, its CV profile displays a more rectangular shape, indicating an ideal double layer capacitance in Figure 4.10C. As a result, more capacitance can be extracted from the cell and it exhibits better rate capability under large current densities as the red curve in Figure 4.10D illustrates. There is barely any capacitance for the cell with Nanomat 50% above the current density of 5 mA/coin cell. That's because it will be very difficult for electrolyte ions to diffuse through the separator without the network of the connected pores, leading to the slow ion adsorption and desorption process, which results in the poor capacitance behavior. It is worth noting that the enhanced electrochemical performance with increased pore volume is not a special case for the 50 nm ZnO. We observed similar results from the microsized ZnO as Figure 4.11 demonstrates.

In addition, electrochemical comparisons of the porous PVDF film (Nanomat 100%), nonporous PVDF sheet and commercial PE separator was conducted in a coin cell with activated carbon electrodes. The results are listed in Figure 4.12. Both CV curves with porous PVDF and PE separators display nearly textbook rectangular shapes suggesting good capacitive behavior, while the red curve representing the cell with nonporous PVDF film does not show a rectangular shape likely due to the lack of the pore structure (Figure 4.12A). On the other hand, our porous PVDF film presents similar capacitance (Figure 4.12B) and ion diffusion performance (Figure 4.12C) with the commercial PE separator, which is promising for real world applications.

4.3.3 Choice of the electrode materials for the self-charging supercapacitor

With decent piezoelectric and electrochemical properties, the porous PVDF film (Nanomat) is confirmed to be a good candidate as a separator for self-charging power units. In order to make a full cell, suitable electrode materials with good electrochemical performance are needed to work with the PVDF separators. We tested two different kinds of materials in the following section to seek the best electrodes for our porous separator.

Single walled carbon nanotubes (SWCNTs)/laser scribed graphene (LSG)

Carbon nanotubes (CNT) and graphene are attractive double layer materials[25] for supercapacitor thanks to their high surface area (1315 m^2/g[26] for SWCNT and 2630 m^2/g[27] for graphene), low resistance[28-29] and electrochemical stability.[25] The charges are stored

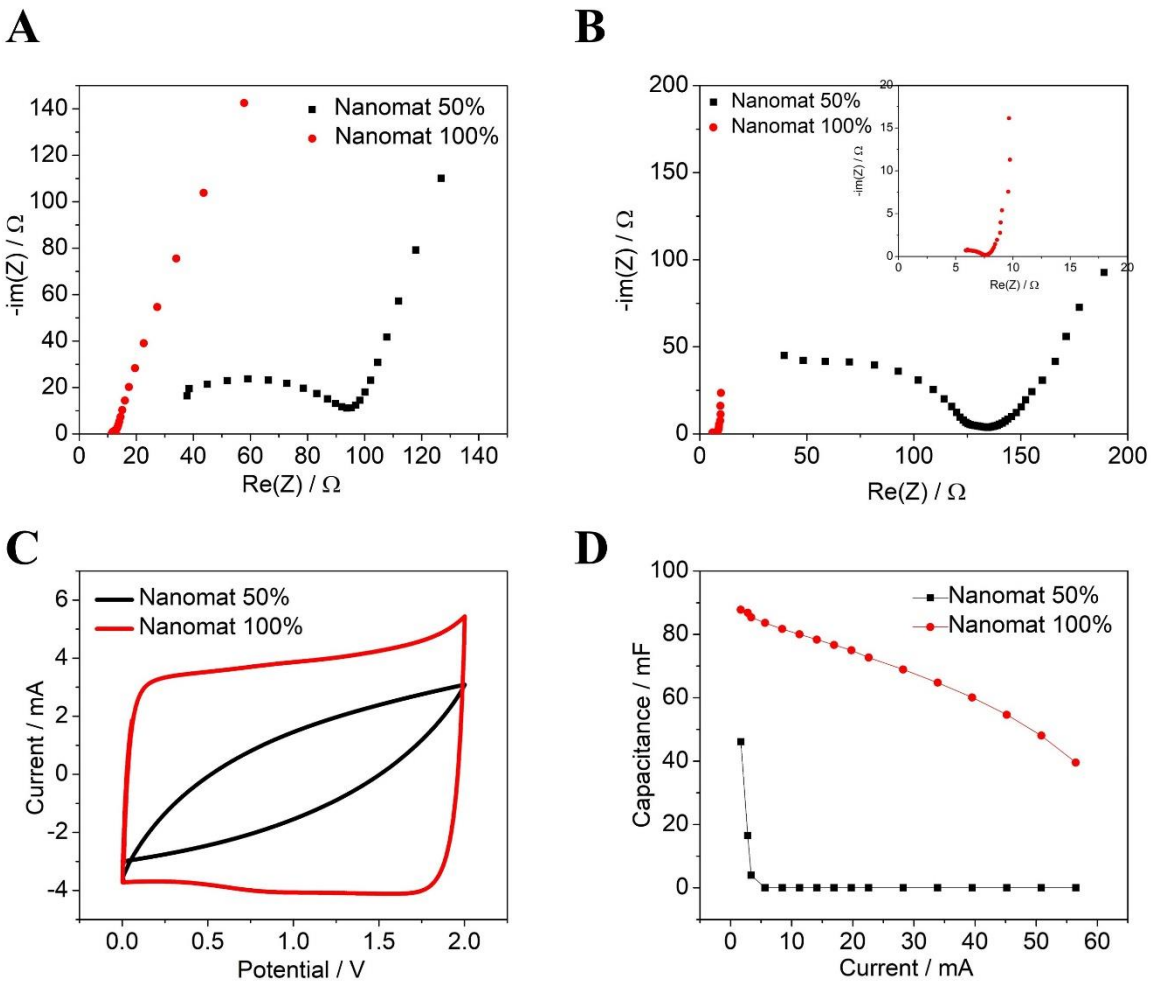

Figure 4.10 Electrochemical performance comparison of porous PVDF separators made with different ratios of nano-sized ZnO. The ratio of the ZnO is calculated by dividing the weight of the ZnO added with the weight of the PVDF used. (A) A dramatic decrease in cell resistance is observed in EIS when the ratio of the ZnO to PVDF is increased from 50% to 100%. The pore volume will increase with more ZnO particels, resulting in more interconnecting pore structures, which facilitates the ion diffusion process in the cell. (B) Similar results are achieved when the porous PVDF separators with different pore volumes are put into coin cells with activated carbon as the active material. The resistance of the cell is much less when more ZnO is used. (C) A more rectangular CV shape is seen with porous PVDF made with 100% ZnO due to better ion diffusion.

The current with 100% ZnO is also much higher than the one with 50% Zno. (D) The 100% one shows higher capacitance when compared with the 50% one, which is in consistent with the CV results. Better rate capabilities are also observed with porous PVDF made with the higher ratio of ZnO.

electrostatically through fast ion adsorption and desorption on the electrode surfaces. Unfortunately, carbon nanotubes are likely to bundle, while graphene sheets tend to restack because of strong van der Waals forces.[30-31] This causes a significant decrease in their surface area, hindering the harvesting of the maximum capacitance. To solve this problem, many scientists have proposed fabricating a mixture of the two carbon materials.[32-34] In the resulting composite, carbon nanotubes function as a spacer to prevent the graphene sheets from restacking, while graphene prevents the nanotubes from aggregation. Because of the synergetic effects between the two materials, the composite usually displays higher electrochemical performance than cells with a single component[32].

The method we used to make the CNT/graphene mixture is shown in Figure 4.13A. Single walled carbon nanotubes and graphite oxide (GO) are dispersed and cast onto a substrate, dried overnight, followed by laser scribing to convert the GO content into LSG. The laser scribing technique is inexpensive, convenient and has high output, which is beneficial for potential commercialization. The morphology of the as-prepared SWCNT/LSG composite is displayed in the SEM images in Figure 4.14. Interestingly, the carbon nanotubes are vertically

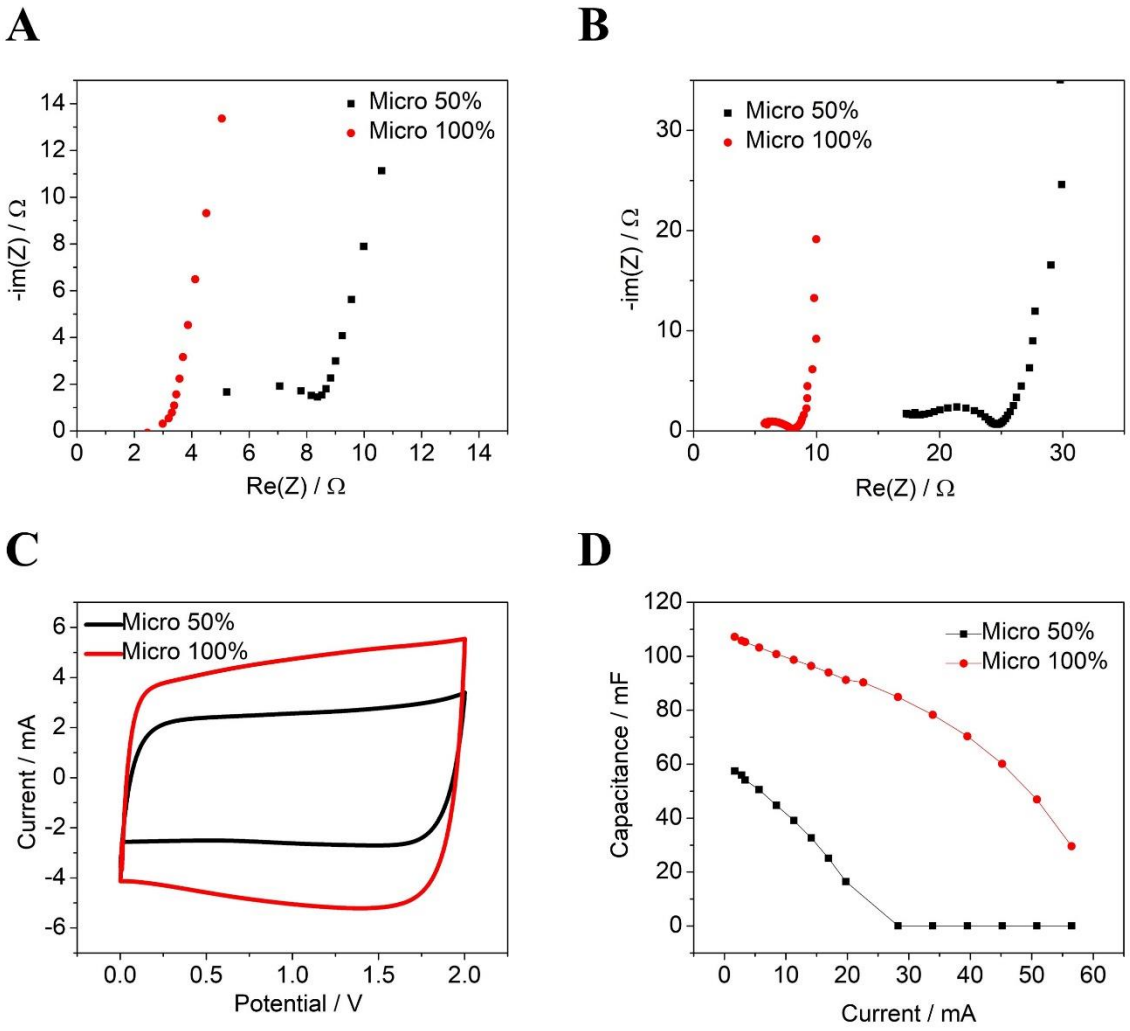

Figure 4.11 Electrochemical performance of porous PVDF made from 50% and 100% micro-sized ZnO, respectively. (A) There is an apparent resistance drop in the EIS when the ratio of the ZnO is increased. (B) Similar EIS results were observed when the porous PVDF film was used as a separator between activated carbon electrodes. (C) Although both cells exhibit rectangular shapes, the one with more ZnO shows higher current density in the CV. (D) A higher capacitance and better retention ratio were obtained in PVDF made with a higher ZnO ratio.

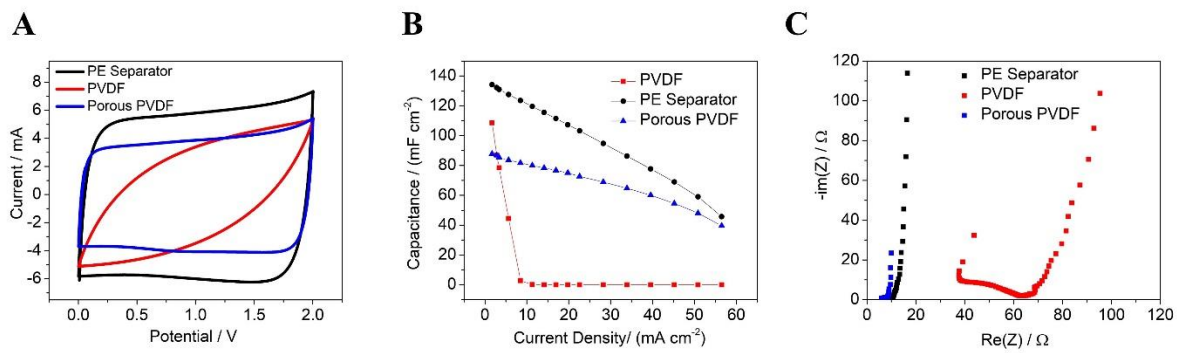

Figure 4.12 Electrochemical performance comparing nonporous PVDF, porous PVDF (100% nanomat ZnO) and a commercially available PE separator. The experiments are in a coin cell setup with activated carbon. (A) Cyclic voltammetry using different separators. Both CVs of PE and porous PVDF separator show almost ideal rectangular shapes. (B) Areal capacitance comparison of three different separators. Apparently, the PVDF separator without the porous structure is not good for ion diffusion and thus has poor capacitance performance. (C) EIS plots of PVDF, porous PVDF and the commercial PE separator. It can be observed that our porous PVDF separator has similar performance with the commercial one, which has low active material, charge transfer and ion diffusion resistance.

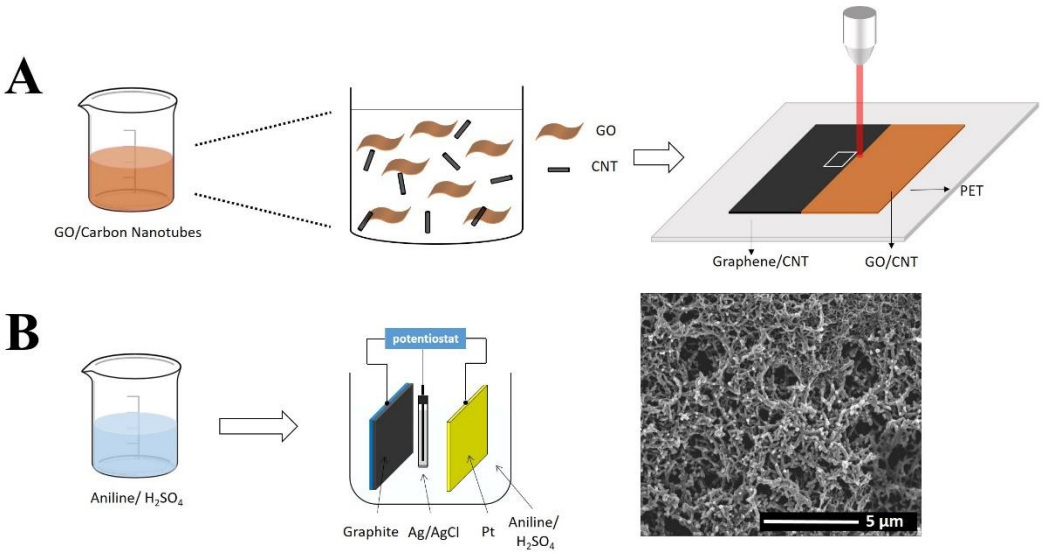

Figure 4.13 (A) A schematic diagram showing the synthesis of a carbon nanotube/LSG composite. Graphite oxide (GO) and carbon nanotubes were dispersed homogenously in water first by stirring and then sonication. The solution was cast onto a PET substrate, dried overnight and scribed with a laser to turn GO into graphene. (B) A diagram illustrating the electrochemical deposition of PANI onto the graphite substrate. A select amount of aniline dimer was dispersed in H_2SO_4 solution as the precursor. A three-electrode setup was used for deposition where graphite was used as the working electrode, Pt as the counter electrode and Ag/AgCl as the reference. The PANI as fabricated exhibits a nanowire morphology.

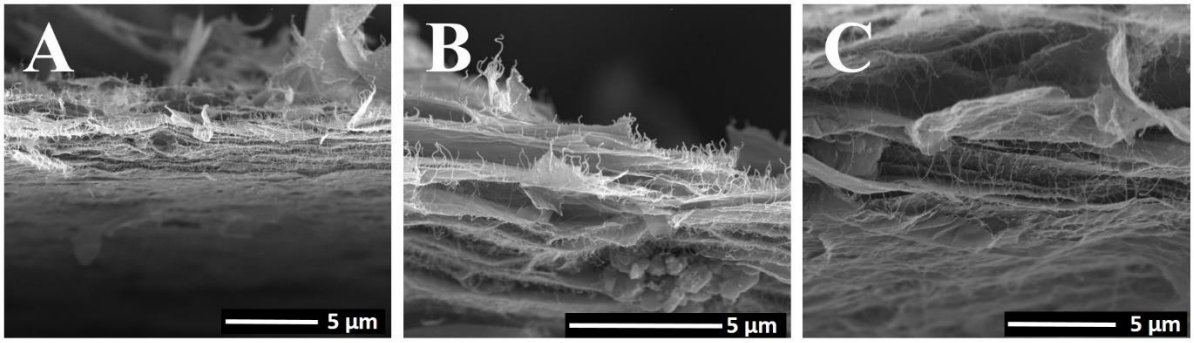

Figure 4.14 (A)-(C) SEM images showing the interconnected network formed from carbon nanotube and laser scribed graphene (LSG) composites. The nanotubes are vertically aligned between graphene sheets, improving the overall conductivity of the hybrid material.

aligned between graphene sheets to form a vermiculite-like architecture. The unique structure is produced through the laser scribing process during which a large amount of gas is generated by the laser, expanding the distance between graphene sheets. As a result, the carbon nanotubes are pulled upright by the moving force of the LSG sheets. In such a structure, carbon nanotubes

connect to the graphene sheets, which could provide more efficient electron pathways between the planar sheets of LSG, further enhancing the conductivity of the composite.

After the SWCNT/LSG electrodes are synthesized, they are assembled into a sandwich device with a porous PVDF separator in between as illustrated in Figure 4.15A. A series of electrochemical characterizations were conducted on the cell, revealing good performance of the device. The cyclic voltammetry curves in Figure 4.15B under diverse scan rates show an almost identical rectangular shape, which is an indication of ideal double layer capacitive behavior. The constant current charging/discharging curves (CC) of the device in Figure 4.15C exhibit similar charging and discharging times, suggesting good Coulombic efficiency. In addition, there is no apparent IR drop at the beginning of the discharge curve, which indicates good conductivity for the entire cell. The low resistance of the device can be confirmed by electrochemical impedance spectroscopy (Figure 4.15D) and attributed to the conductive nature of the SWCNT/LSG composite and the interconnected pore network in the PVDF separator. Since the carbon mixture has very high surface area, the areal capacitance of the cell is over 20 mF/cm^2 (Figure 4.15E).

Although the cell displays good electrochemical properties, its self-charging performance is not as good as expected as demonstrated in Figure 4.15F. The supercapacitor is only charged to 0.03 V with palm pressing. A possible explanation is that the SWCNT/LSG electrodes show a fluffy texture which could withstand most of the deformation during palm impact. Therefore, there is not much distortion in the PVDF film, leading to a low piezopotential on the separator surface. Thus, the supercapacitor does not charge up to a high voltage. The LSG electrodes are therefore not good candidates for self-charging supercapacitors due to their same fluffy morphology (Figure 4.16).

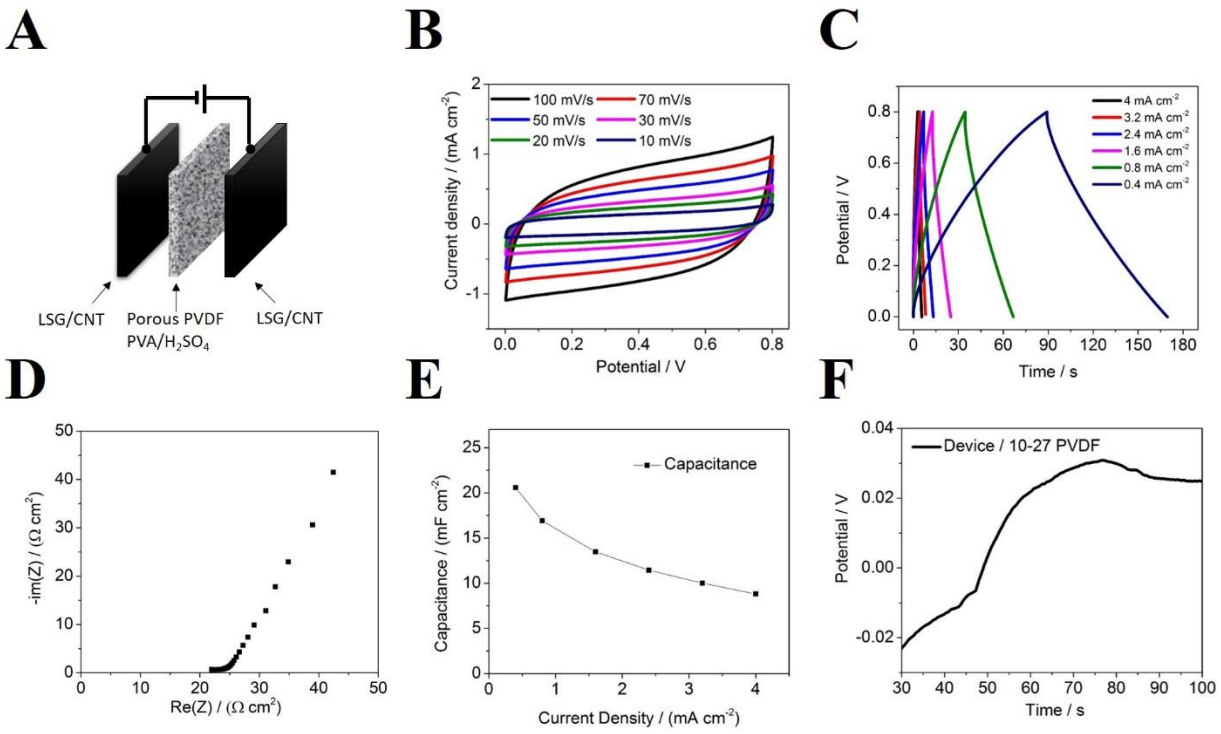

Figure 4.15 (A) a schematic diagram showing the sandwich structure of the cell: LSG/CNT composites are applied as both positive and negative electrodes with a porous PVDF separator in between. PVA/H_2SO_4 is used as a gel electrolyte. (B) Cyclic voltammetry tests of the hybrid cell. The CV profiles under different scan rates all exhibit a fairly rectangular shape, indicating good power performance of the cell. (C) Triangular shapes without significant IR drops are observed in constant current charging/discharging curves, indicating that the cell has low resistance. (D) Areal capacitance of the LSG/CNT electrodes. (E) EIS plots of the cell with porous PVDF as the separator. No apparent ion diffusion resistance is seen in the spectra. (F) Cell charging performance during palm pressing. An increase of only 0.03 V is observed. This is probably due to the fluffy texture of the LSG/CNT electrodes. When force is applied, the deformation takes place mainly in the electrode rather than in the separator, which induces a very limited potential increase.

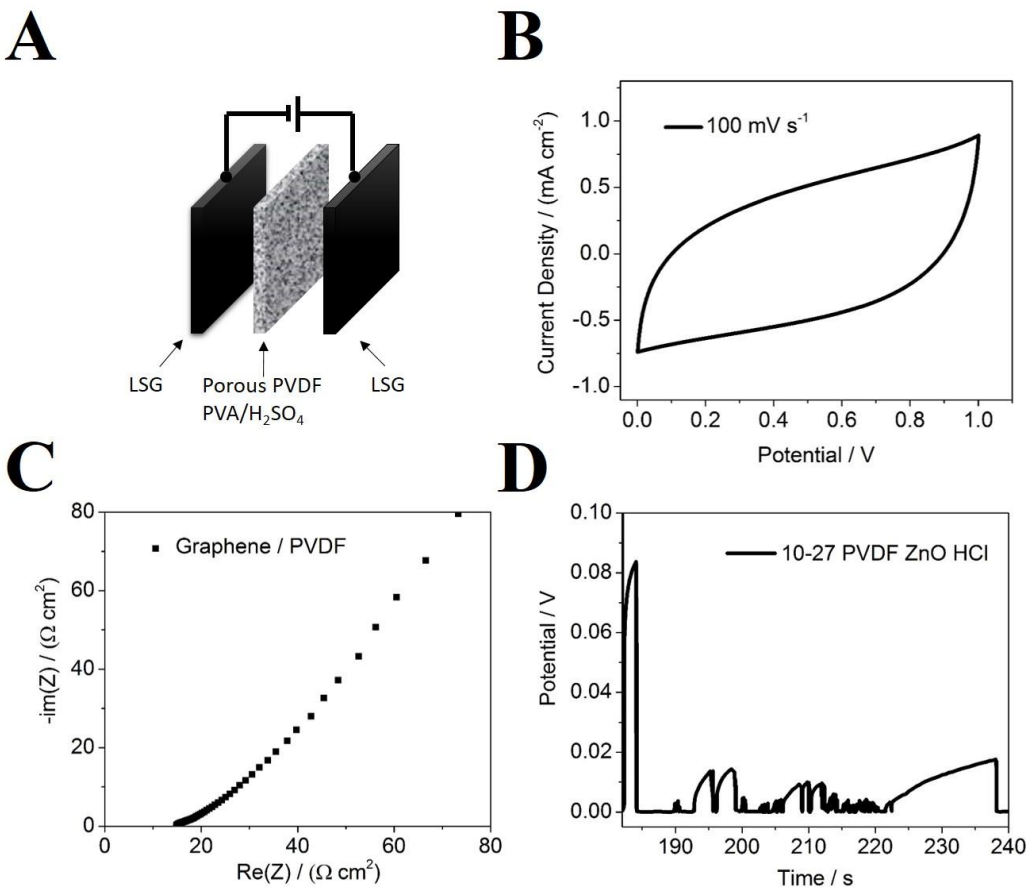

Figure 4.16 (A) A schematic diagram of the LSG/PVDF/LSG cell. PVA/H_2SO_4 gel is used as the electrolyte. (B) Cyclic voltammetry of the supercapacitor composed of LSG and a porous PVDF separator. (C) Electrochemical impedance spectra of the cell. The overall resistance is less than 20 ohms. (D) The potential response of the cell is only 0.08 V with palm pressing, which is believed to be due to the porous structure of the LSG. The deformation occurring in the LSG, rather than in the PVDF separator, results in the small potential increase.

PANI as the supercapacitor electrodes

In order to have a good piezoelectric response, most of the deformation needs to occur on the PVDF film. Polyaniline is a good candidate as the electrode material for the self-charging

supercapacitor owing to its good conductivity,[35] capacity[36] and perhaps most importantly, it is not fluffy in nature. An electrodeposition method was selected to produce the polyaniline on a graphite substrate in a three-electrode setup, during which an aniline monomer/H_2SO_4 solution was used as the electrolyte, platinum foil functioned as the counter electrode and an Ag/AgCl electrode was utilized as a reference electrode (Figure 4.13B). From the same image, it can be seen that the PANI electrode exhibits a compact network composed of interconnected nanowires when we look at the morphology through SEM.

The self-charging device is packed as demonstrated in Figure 4.17A. Two identical polyaniline electrodes form a sandwich surrounding the porous PVDF and the PVA/H_2SO_4 gel electrolyte. Figure 4.17B is the CV curves of the device under diverse scan rates. Although we increased the scan rate from 10 mV/s to 100 mV/s, there is no change in the shape of the CV at all, indicating that our material can undergo very high charging/discharging speeds. Two pairs of peaks are observed in the CV curve around 0.2 V and 0.4 V due to the redox reactions in the polyaniline when potential is increased. Since the PANI we fabricated are made of a nanowire structure, most of the reaction takes place on the surface of the material, displaying indistinct redox peaks. In addition, the huge amount of surface area brings large double layer capacitance, which makes the redox peaks even harder to be noticed.

The constant current charging/discharging curves of the device are shown in Figure 4.17C. No apparent IR drop is seen in any of the triangular curves, which implies low resistance in the system. This assumption is confirmed by the Nyquist impedance plot in Figure 4.17D. The curve has an intercept with the X axis at around 13.4 Ω which means the resistance from the active material, electrolyte and the interfacial contact resistance are as low as 13.4 Ω. This is really beneficial for supercapacitor applications. Besides, the PANI electrodes show good capacitance as

can be seen in Figure 4.17E. Their areal capacitance is over 35 mF/cm^2, higher than the 20 mF/cm^2 of the SWCNT/LSG composite. Moreover, our PANI material is able to maintain over 85% of its original capacitance when the scan rate was increased by 10 times, which indicates good rate capabilities. When we tried to charge the device with palm impact, the open circuit potential of the self-charging unit increased to over 0.2 V as displayed in Figure 4.17F. This value is higher than the 0.11 V reported in the literature[13] and is promising for future applications.

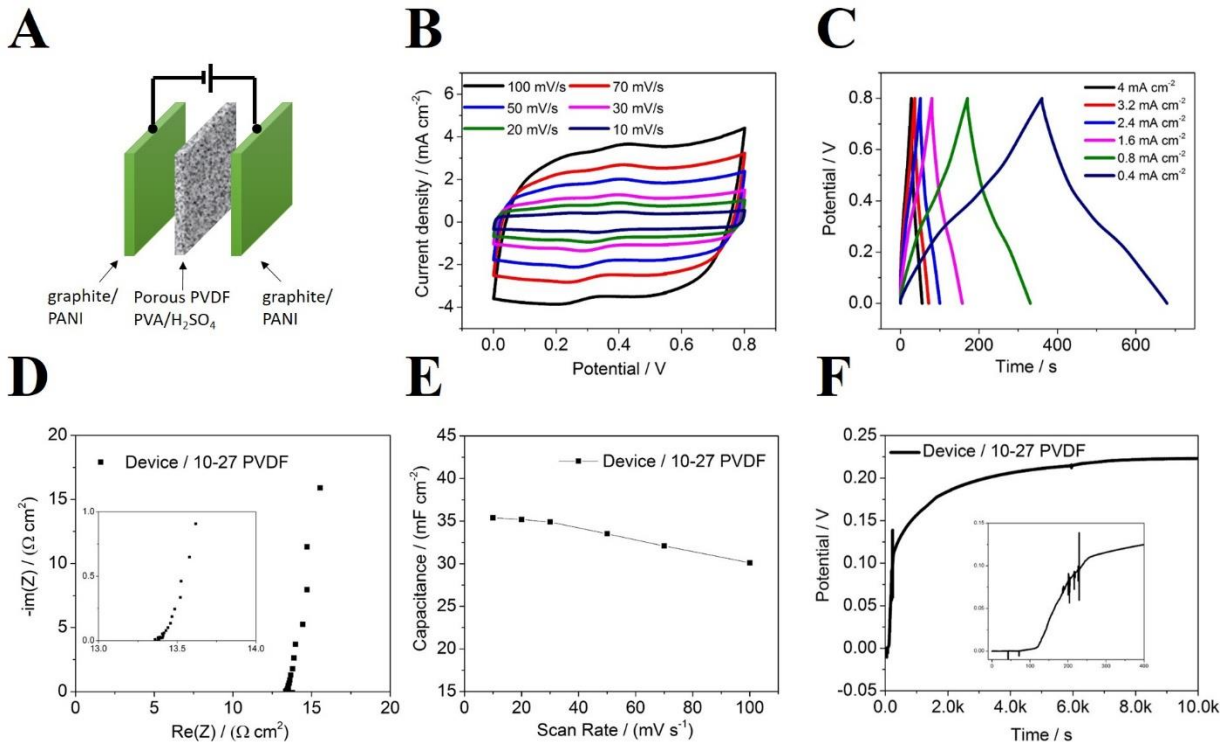

Figure 4.17 (A) Diagram of the PANI/PVDF/PANI sandwich cell. PVA/H_2SO_4 is utilized as a gel electrolyte. (B) CV curves of the 2-electrode device. Even when the scan rate is increased to 100 mV/s, the CV shape is still identical to those of slower scan rates, which indicates good conductivity of the cell. Slight redox peaks are also observed in the CVs. (C) Constant current charging/discharging curves of the cell. (D) Areal capacitance for the PANI electrode at different

scan rates. The capacitance retention is over 85% when the scan rate is increased 10 times. (E) EIS data show that the resistance of the cell is less than 15 ohms and no apparent ion diffusion resistance is seen. (F) The device is charged to 0.2 V by palm pressing.

4.4 Experimental Section

4.4.1 Synthesis of nonporous PVDF film.

In a typical experiment, 5 g of the PVDF powder (from Sigma Aldrich) was added into 45 g of the N,N-dimethylformamide (DriSolv, DMF Anhydrous) and the mixture was stirred and heated to 65 °C until a transparent solution was formed. The solution was cooled down naturally to room temperature and cast onto glass by a doctor blade. The film was then dried in an oven at 75 °C.

4.4.2 Fabrication of porous PVDF separators.

5 g of the PVDF powder was added into 40 g of DMF to form a transparent solution as described before[14]. A select amount of ZnO (US Research Nanomaterials, Inc., particle size: 35–45 nm; Sigma Aldrich, particle size <100 nm; Sigma Aldrich, particle size <5 μm. The ratio of the ZnO is determined by dividing ZnO's weight by PVDF's) was dispersed homogeneously into 5 g of DMF via stirring and sonication. The ZnO dispersion was then poured into the PVDF solution and stirred to form a milky-white suspension. After the suspension was cooled to room temperature, a doctor blade was used to cast the film on glass, followed by drying in an oven at 75 °C.

The film was peeled off and immersed in hydrochloric acid (Fisher Scientific, HCl, 36.5-38.0%) solution overnight to remove the ZnO template. DI water was utilized to wash the film thoroughly and the film was dried in air without heating.

4.4.3 Synthesis of Carbon Nanotube/LSG electrodes.

A select ratio of single-walled carbon nanotube (SWCNT, Carbon Solutions, Inc P2-SWCNT) and graphite oxide (GO) were mixed in DI water, followed by stirring and sonication to get a homogeneously dispersed SWCNT/GO suspension. The dispersion was then drop-cast onto the PET substrate (3M, PP250) and dried overnight in air. A laser scribing process was conducted afterwards using a CO_2 laser (Full spectrum laser, MLE-40, 10.6 μm) to convert the SWCNT/GO into a SWCNT/LSG composite.

4.4.4 Synthesis of polyaniline (PANI) electrodes.

PANI electrodes were fabricated by an electrochemical deposition method.[37] A three-electrode setup was utilized where a graphite substrate functions as the working electrode, a platinum foil serves as the counter electrode and an Ag/AgCl is the reference electrode. A 100 mM aniline monomer solution was made by dispersing aniline into 1 M H_2SO_4 and was used as the electrolyte. A constant potential of 0.78 V was applied to deposit the PANI on the graphite substrate.

4.4.5 Electromechanical property measurement of the PVDF films

The PVDF films were cut into 1 cm × 2 cm pieces and copper tape was applied on both sides for conducting purposes. The Cu/PVDF/Cu was connected to the potentiostat (Biologic VMP3 electrochemical workstation) to record the potential changes during palm pressing.

4.4.6 Electrochemical measurements

The ion diffusion process of the PVDF films and PE separators were conducted in coin cells (CR2032), where the films were placed between two stainless separators and no active material was used. The electrochemical performance of diverse separators with activated carbon was also evaluated in the same coin cell setup. The electrochemical properties of SWCNT/LSG, LSG and PANI with the porous PVDF separator was tested in a sandwich cell. All the electrochemical tests including cyclic voltammetry (CV), galvanostatic charge/discharge cycles and electrochemical impedance spectroscopy (EIS) were measured using a Biologic VMP3 electrochemical workstation.

4.4.7 Characterization

The pore structure of the PVDF and morphology of the PANI electrodes were characterized using a Scanning Electron Microscope (Nova 230 NanoSEM). The β-phase of the PVDF was detected by using Fourier-transform infrared spectroscopy (Jasco FT/IR-6300) and the crystal structure was determined by X-ray diffraction (XRD, Bruker DUO Apexll CCD-single crystal X-ray Diffractometer).

4.5 Conclusions

Based on our study, we discovered that wurtzite type ZnO with a small size is beneficial for induction of the β type PVDF, enhancing the piezoelectric performance. In contrast, large ZnO particles help build an interconnected pore structure in the polymer film, which will facilitate ion diffusion in the supercapacitor and improve its electrochemical properties. With rational design of the pore size and pore volume, we were able to achieve a PVDF film with both decent piezoelectric and electrochemical performance. Amazingly, the porous PVDF even shows similar ion diffusion

behavior to a commercial PE separator. The self-charging cell we assembled with the porous PVDF separator and PANI electrodes showed outstanding supercapacitor performance. The device can be charged to 0.2 V with palm impact, which is superior to previous published values and promising for future applications.

4.6 Appendix to Chapter 4

Calculations:

The areal capacities of the CNT/LSG and LSG sandwich devices were calculated based on constant current charging/discharging curves at different current densities.

Areal Capacitance C (F cm^{-2}) = $\frac{Idt}{VS}$ (I *(A)* is the current used, dt *(s)* is the discharge time, V *(Volt)* is the potential window, $S(cm^2)$ is the electrode area)

The capacitances of the PANI devices were calculated from Cyclic Voltammetry at different scan rates:

Areal Capacity $\mathrm{C}\ (C\ cm^{-2}) = \frac{\int_{V_1}^{V_2} idV}{v\ S}$ ($V_1(Volt)$ and $V_2(Volt)$ are the potential range, i (A) is the current, $v(Volt\ sec^{-1})$ is the scan rate, $S(cm^2)$ is the electrode area)

The capacitance relation between device and electrodes are as follows:

Areal Capacitance of the electrode (F cm^{-2}) = 2 * Areal Capacitance of the device (F cm^{-2})

4.7 References

(1) Zhang, X.S.; Han, M.D.; Wang, R.X.; Zhu, F.Y.; Li, Z.H.; Wang, W.; Zhang, H.X. Frequency-multiplication high-output triboelectric nanogenerator for sustainably powering biomedical microsystems. *Nano Lett.* **2013**, *13*, 1168-1172.

(2) Yang, P.K.; Lin, L.; Yi, F.; Li, X.; Pradel, K.C.; Zi, Y.; Wu, C.I.; He Jr, H.; Zhang, Y.; Wang, Z.L. A Flexible, Stretchable and Shape‐Adaptive Approach for Versatile Energy Conversion and Self‐Powered Biomedical Monitoring. *Adv. Mater.* **2015**, *27*, 3817-3824.

(3) Gu, L.; Cui, N.; Cheng, L.; Xu, Q.; Bai, S.; Yuan, M.; Wu, W.; Liu, J.; Zhao, Y.; Ma, F.; Qin, Y. Flexible fiber nanogenerator with 209 V output voltage directly powers a light-emitting diode. *Nano Lett.* **2012**, *13*, 91-94.

(4) Yi, F.; Wang, J.; Wang, X.; Niu, S.; Li, S.; Liao, Q.; Xu, Y.; You, Z.; Zhang, Y.; Wang, Z.L. Stretchable and waterproof self-charging power system for harvesting energy from diverse deformation and powering wearable electronics. *ACS Nano*, **2016**, *10*, 6519-6525.

(5) Niu, S.; Wang, X.; Yi, F.; Zhou, Y.S.; Wang, Z.L. A universal self-charging system driven by random biomechanical energy for sustainable operation of mobile electronics. *Nat. Commun.* **2015**, *6*, 8975.

(6) Guo, W.; Xue, X.; Wang, S.; Lin, C.; Wang, Z.L. An integrated power pack of dye-sensitized solar cell and Li battery based on double-sided TiO_2 nanotube arrays. *Nano Lett.* **2012**, *12*, 2520-2523.

(7) Wang, Z.L.; Song, J. Piezoelectric nanogenerators based on zinc oxide nanowire arrays. *Science*, **2006**, *312*, 242-246.

(8) Wang, Z.L. and Wu, W., Piezotronics and piezo-phototronics: fundamentals and applications. *Natl. Sci. Rev.* **2013**, *1*, 62-90.

(9) Zhu, H.; Mitsuishi, M.; Miyashita, T. Facile Preparation of Highly Oriented Poly (vinylidene fluoride) Langmuir–Blodgett Nanofilms Assisted by Amphiphilic Polymer Nanosheets. *Macromolecules*, **2012**, *45*, 9076-9084.

(10) Damjanovic, D. Ferroelectric, dielectric and piezoelectric properties of ferroelectric thin films and ceramics. *Rep. Prog. Phys*. **1998**, *61*, 1267.

(11) Broadhurst, M.G.; Davis, G.T.; McKinney, J.E.; Collins, R.E. Piezoelectricity and pyroelectricity in polyvinylidene fluoride—A model. *J. Appl. Phys.* **1978**, *49*, 4992-4997.

(12) Xue, X.; Deng, P.; He, B.; Nie, Y.; Xing, L.; Zhang, Y.; Wang, Z.L. Flexible Self‐Charging Power Cell for One‐Step Energy Conversion and Storage. *Adv. Energy Mater*. **2014**, *4*, 1301329.

(13) Ramadoss, A.; Saravanakumar, B.; Lee, S.W.; Kim, Y.S.; Kim, S.J.; Wang, Z.L. Piezoelectric-driven self-charging supercapacitor power cell. *ACS Nano*, **2015**, *9*, 4337-4345.

(14) Mao, Y.; Zhao, P.; McConohy, G.; Yang, H.; Tong, Y.; Wang, X. Sponge‐Like Piezoelectric Polymer Films for Scalable and Integratable Nanogenerators and Self‐Powered Electronic Systems. *Adv. Energy Mater*. **2014**, *4*, 1301624.

(15) Özgür, Ü.; Alivov, Y.I.; Liu, C.; Teke, A.; Reshchikov, M.; Doğan, S.; Avrutin, V.C.S.J.; Cho, S.J.; Morkoc, H. A comprehensive review of ZnO materials and devices. *J. Appl. Phys.* **2005**, *98*, 11.

(16) Dae-Yeong, L.; Hyunjin, K.; Hua-Min, L.; Jang, A. R.; Yeong-Dae, L.; Seung Nam, C.; Young Jun, P.; Dae Joon, K.; Won Jong, Y. Hybrid energy harvester based on nanopillar solar cells and PVDF nanogenerator. *Nanotechnology*, **2013**, *24*, 175402.

(17) Dhakras, D.; Borkar, V.; Ogale, S.; Jog, J. Enhanced piezoresponse of electrospun PVDF mats with a touch of nickel chloride hexahydrate salt. *Nanoscale.* **2012**, *4*, 752.

(18) Cha, S.; Kim, S. M.; Kim, H.; Ku, J.; Sohn, J. I.; Park, Y. J.; Song, B. G.; Jung, M. H.; Lee, E. K.; Choi, B. L.; Park, J. J.; Wang, Z. L.; Kim, J. M.; Kim, K. Porous PVDF as effective sonic wave driven nanogenerators. *Nano Lett*. **2011**, *11*, 5142.

(19) Bae, S.H.; Kahya, O.; Sharma, B.K.; Kwon, J.; Cho, H.J.; Ozyilmaz, B.; Ahn, J.H. Graphene-P(VDF-TrFE) multilayer film for flexible applications. *ACS Nano*, **2013**, *7*, 3130-3138.

(20) Salimi, A.; Yousefi, A.A. Analysis method: FTIR studies of β-phase crystal formation in stretched PVDF films. *Polym Test*, **2003**, *22*, 699-704.

(21) Zheng, J.; He, A.; Li, J.; Han, C.C. Polymorphism control of poly(vinylidene fluoride) through electrospinning. *Macromol. Rapid Commun*. **2007**, *28*, 2159-2162.

(22) Shah, D.; Maiti, P.; Gunn, E.; Schmidt, D.F.; Jiang, D.D.; Batt, C.A.; Giannelis, E.P. Dramatic enhancements in toughness of polyvinylidene fluoride nanocomposites via nanoclay‐directed crystal structure and morphology. *Adv. Mater*. **2004**, *16*, 1173-1177.

(23) Priya, L. and Jog, J.P., 2002. Poly (vinylidene fluoride)/clay nanocomposites prepared by melt intercalation: crystallization and dynamic mechanical behavior studies. *J. Polym. Sci. B Polym Phys.* **2002**, *40*, 1682-1689.

(24) Wang, Z.L.; Kong, X.Y.; Zuo, J.M. Induced growth of asymmetric nanocantilever arrays on polar surfaces. *Phys. Rev. Lett.* **2003**, *91*, 185502.

(25) Simon, P.; Gogotsi, Y. Materials for electrochemical capacitors. *Nat. Mater.* **2008**, *7*, 845.

(26) Peigney, A.; Laurent, C.; Flahaut, E.; Bacsa, R.R.; Rousset, A. Specific surface area of carbon nanotubes and bundles of carbon nanotubes. *Carbon*, **2001**, *39*, 507-514.

(27) Zhu, Y.; Murali, S.; Stoller, M.D.; Ganesh, K.J.; Cai, W.; Ferreira, P.J.; Pirkle, A.; Wallace, R.M.; Cychosz, K.A.; Thommes, M.; Su, D. Carbon-based supercapacitors produced by activation of graphene. *Science*, **2011**, *332*, 1537-1541.

(28) Geim, A.K.; Novoselov, K.S. The rise of graphene. *Nat. Mater.* **2007**, *6*, 183.

(29) Lekawa‐Raus, A.; Patmore, J.; Kurzepa, L.; Bulmer, J.; Koziol, K. Electrical properties of carbon nanotube based fibers and their future use in electrical wiring. *Adv. Funct. Mater*. **2014**, *24*, 3661-3682.

(30) El-Kady, M.F.; Strong, V.; Dubin, S.; Kaner, R.B. Laser scribing of high-performance and flexible graphene-based electrochemical capacitors. *Science*, **2012**, *335*, 1326-1330.

(31) Futaba, D.N.; Hata, K.; Yamada, T.; Hiraoka, T.; Hayamizu, Y.; Kakudate, Y.; Tanaike, O.; Hatori, H.; Yumura, M.; Iijima, S. Shape-engineerable and highly densely packed single-walled carbon nanotubes and their application as super-capacitor electrodes. *Nat. Mater*. **2006**, *5*, 987.

(32) Pham, D.T.; Lee, T.H.; Luong, D.H.; Yao, F.; Ghosh, A.; Le, V.T.; Kim, T.H.; Li, B., Chang, J.; Lee, Y.H. Carbon nanotube-bridged graphene 3D building blocks for ultrafast compact supercapacitors. *ACS Nano*, **2015**, *9*, 2018-2027.

(33) Jung, N.; Kwon, S.; Lee, D.; Yoon, D.M.; Park, Y.M.; Benayad, A.; Choi, J.Y.; Park, J.S. Synthesis of chemically bonded graphene/carbon nanotube composites and their application in large volumetric capacitance supercapacitors. *Adv. Mater*. **2013**, *25*, 6854-6858.

(34) Jha, N.; Ramesh, P.; Bekyarova, E.; Itkis, M.E.; Haddon, R.C. High energy density supercapacitor based on a hybrid carbon nanotube–reduced graphite oxide architecture. *Adv. Energy Mater.* **2012**, *2*, 438-444.

(35) Li, D.; Huang, J.; Kaner, R.B. Polyaniline nanofibers: a unique polymer nanostructure for versatile applications. *Acc. Chem. Res*. **2008**, *42*, 135-145.

(36) Wang, K.; Huang, J.; Wei, Z. Conducting polyaniline nanowire arrays for high performance supercapacitors. *J. Phys. Chem. C*, **2010**, *114*, 8062-8067.

(37) Johnson, B.J.P.S.M.; Park, S.M. Oxidation of aniline at bare and polyaniline modified platinum electrodes studied by electrochemical impedance spectroscopy. *J. Electrochem. Soc.* **1996**, *143*, 1269-1276.

CHAPTER 5

A Monolithically Integrated Self charging Power Pack Consisting of Silicon Nanowires Array PEDOTPSS Hybrid Solar Cell and Laser scribed Graphene Supercapacitor

5.1 Abstract

Due to the demand for portable and sustainable energy sources and the need for miniaturization and multi-functionalization in the electronics industry, the study of integrated self-charging power packs has attracted increasing attention. A new self-charging power pack consisting of a silicon nanowire array/PEDOT:PSS hybrid solar cell and a laser-scribed graphene supercapacitor has been fabricated. The Si nanowire array/PEDOT:PSS hybrid solar cell structure exhibited a high power conversion efficiency (PCE) of 12.37%. The laser-scribed graphene (LSG) demonstrated excellent energy storage capability for the power pack, with high current density, energy density and cyclic stability when compared to other supercapacitor electrodes such as active carbon and conducting polymers. The overall efficiency of the power unit is 2.92%.

5.2 Introduction

Smartphones, electric vehicles, intelligent household electrical appliances, and many other smart electronic products have increasingly blended into our daily lives. However, the energy supply issue remains a key technical challenge. Specially, the demand for sustainable and rapid charging/discharging energy sources is rapidly increasing, and hybrid devices integrating energy harvesting and storage functions have been investigated as an attractive solution.[1-7] For energy harvesting, solar cells are a good choice among all the power supply systems due to their

sustainable and environmentally friendly characteristics.[8,9] For energy storage, lithium ion batteries offer among the highest energy densities,[10-12] but they present environmental hazards, and suffer from low power density and a limited number of charge/discharge cycles. On the other hand, supercapacitors can make up for these shortfalls with high power density, long cycle life, and long-term stability.[13-15] However, the low energy density necessitates frequent recharging. Therefore, supercapacitors integrated with solar cells for self-charging could be an ideal solution to meet the energy demands of portable devices.

Many research efforts have reported on the development of integrated power systems based on solar cells and supercapacitors.[16-23] Dye-sensitized solar cells (DSSCs), organic solar cells (OSCs)[20,21] and perovskite solar cells have all been investigated as the energy harvesting part of integrated power systems.[22] However, achieving a PCE of over 10% is still challenging for a single DSSC or OSC.[24-26] Furthermore, the fabrication of DSSCs requires high temperature processing which can be rather energy consuming. OSCs employ air-sensitive compounds and require hermetic sealing that incurs high costs. Recently, hybrid solar cells (HSCs) made up of an inorganic semiconductor and an organic conducting polymer have attracted a lot of attention due to their potential to produce high efficiency solar cells by a simple low cost process. In particular, a hybrid structure consisting of n-type crystalline Si with surface nanostructures and an organic poly(3,4-ethylenedioxythiophene):polystyrenesulfonate (PEDOT:PSS) hole-transporting layer was fabricated in air with a power conversion efficiency (PCE) above 10%.[27-29] This HSC architecture has the potential to combine the broadband optical absorption capability of nanostructured silicon with low-cost solution-based production processes.

Used in a power pack, a stable power storage and supply would be a significant characteristic. On the other hand, the primary purpose of using a supercapacitor is for its high

charge/discharge rates. At this point, the ability to operate at both high rate and high stability is an important metric when choosing the energy storage component of a power pack. Carbon and conducting polymer-based supercapacitors have previously been integrated into solar cells.[18,22,23,30] However, so far, excellent charge/discharge rates and stability have not been reported. Specifically, to the best of our knowledge, there are no reports showing ideal capacitance characteristics with cyclovoltammetric (CV) scan rates up to 200 mV/s. Liu *et al*.[23] and Wang *et al*.[30] have used a polypyrrole-based supercapacitor for energy storage in a power pack. However, just like other conducting polymer materials, polypyrrole shows high capacitance, but suffers from low charging/discharging rates and short cycle lifetimes. In general, the capacitance retention drops to only 30% after 2000 cycles.[31,32] In contrast to conducting polymers, carbon-based materials can often be used for millions of cycles. For example, Liu *et al*.[22] employed an activated carbon-based supercapacitor for energy storage in a power pack and good stability was obtained. However, the CV test showed low charge/discharge rates. Moreover, the insulating binders used lowered conductivity, and the presence of micropores that are inaccessible to the electrolyte led to a limited double layer capacitance.[18,22]

An outstanding carbon material is graphene. Graphene's planar structure gives rise to fast charging and discharging because the electrolyte ions can readily access the large surface area of the sheets. However, the strong sheet-to-sheet van der Waals interactions among graphenes during its processing often cause restacking of the graphene sheets, leading to a reduction in the specific surface area of graphene, a lowering of its capacitance and low charge/discharge rates[33-36]. Scalia *et al*.[17] reported a power pack based on a DSSC with graphene nanoplatelets. The graphene electrode showed only a moderate surface area of 500-700 m^2/g. As a result, only mediocre CV test results wer obtained. El-Kady, *et al*. used a standard LightScribe DVD optical drive to convert

initially stacked graphite oxide (GO) sheets into well-exfoliated laser-scribed graphene (LSG) sheets.[34] The resulting LSG films showed a high specific surface area (1520 m^2/g) and high electrical conductivity (1738 S/m). The LSG film can be directly used as EC electrodes without the need for any additional binders. Supercapacitors made with these electrodes exhibited ultra-high energy density values, while maintaining high power density and excellent cycle stability.[34] Therefore, an LSG supercapacitor should be an excellent choice as the energy storage component of a power pack.

Here we report a self-charging power pack integrating a high performance silicon nanowire (SiNW)/PEDOT:PSS solar cell with an LSG supercapacitor. A dual-functional gold film was employed as an adjunct electrode to connect the energy harvesting and storage parts. The solar power conversion efficiency obtained was 12.37%. The LSG supercapacitor demonstrated excellent energy storage capabilities for the power pack. A nearly rectangular CV curve was obtained even when the scan rate was ramped up to 1500 mV/s. Over 90% capacitance retention was observed after 10,000 consecutive cycles demonstrating excellent stability. The integrated power system yielded a total energy conversion and storage efficiency of 2.92%.

5.3 Experimental

5.3.1 Silicon nanowire fabrication

Vertically aligned SiNW arrays were fabricated on n-type Si (100) wafers (University Wafer, 1-10 Ω.cm) by a simple, low-cost metal-assisted chemical etching process[37] in a solution of 0.46 M hydrofluoric acid (HF) and 0.01 M silver nitrate ($AgNO_3$). The substrates were ultrasonically cleaned for 10 min successively in acetone and isopropyl alcohol and rinsed with DI water. The substrate was then cleaned with a piranha solution (4:1 H_2SO_4/H_2O_2) at 80 °C for 10

min and rinsed with DI water. Finally, each sample was dried in a stream of N_2. To deposit silver nanoparticles onto the substrate by a galvanic displacement reaction, the Si substrate was immersed in a solution consisting of 4.8 M hydrofluoric acid (HF) and 0.01 M silver nitrate ($AgNO_3$). After immersion for 30 s, the substrate was transferred to a mixture of 4.8 M HF, 0.6 M H_2O_2 and DI water. With the dissolution of silicon atoms underneath the Ag nanoparticles, the particles sank into the Si substrate, resulting in SiNWs on the top of the substrate. After that, the silicon substrate was soaked in 30 wt. % nitric acid for 30 min to remove the Ag nanoparticles.

5.3.2 Si/PEDOT:PSS hybrid solar cell fabrication

Following the SiNW fabrication, 1.5 nm ultra-thin Al_2O_3 film was deposited on the SiNW arrays by atomic layer deposition for interfacial passivation. A 100-nm-thick aluminum was deposited onto the backside of the Si wafer by thermal evaporation to form the rear contact. Highly conductive PEDOT:PSS (Clevios PH1000) mixed with 7 wt% ethylene glycol (EG) and 0.25 wt % FS-300 (fluorosurfactant) was dropped onto the SiNW arrays and left for 1 min before it was spin coated at 2000 RPM. It was then annealed at 130°C for 30 min. Finally, silver grids of 100 nm thickness were deposited on the surface of PEDOT:PSS as the top electrode through a shadow mask. Planar Si/PEDOT hybrid cells were also fabricated using the same process for comparison.

5.3.3 Integrated power unit fabrication

Fig. 1A shows a schematic illustration of the structure of the self-charging power pack. A gold film was employed as a dual-functional electrode, connecting the energy harvest part with the storage part. The fabrication of laser-scribed graphene supercapacitors is illustrated in Fig. 3A. First, a thin film of GO dispersed in water was drop-cast onto each substrate, i.e. a rear electrode of the solar cell and polyethylene terephthalate (PET). Second, the GO film was scribed with a

10.6 μm infrared laser to reduce the GO to LSG, as indicated by a change in film color from golden brown to black. Then, the energy-storage part was made by sandwiching an ion porous separator [Celgard 3501 (Celgard, Charlotte, NC)] between two identical LSG electrodes. An aqueous electrolyte of 1.0 M H_2SO_4 was added. The fabrication of the energy harvesting part was processed using the method mentioned above for the standalone solar cells.

5.3.4 Characterization

Morphology of the SiNW arrays and LSG sheets was imaged with a Nova 230 Scanning Electron Microscope. The reflectance spectra of the different Si structures were measured using an integrating sphere by a PerkinElmer Lambda system. Transmittance spectra of PEDOT:PSS were recorded on a Shimadzu UV-1700 spectrophotometer. The photovoltaic characterization was conducted using a Keithley 2400 sourcemeter, under 100 mW/cm^2 AM 1.5 G illumination from a SF-300-B solar simulator (Sciencetech). The electrochemical properties of the supercapacitors were characterized on a Biologic VMP3 electrochemical workstation.

5.4 Results and Discussion

Figure 5.1 shows the structure of the hybrid power pack. The gold film serves as the shared common electrode combining a solar energy harvesting unit on the top and a supercapacitor energy storage unit on the bottom. Under light illumination, electron–hole pairs are generated in the n-type monocrystalline silicon. The photo-generated electron–hole pairs diffuse into the built-in electric field at the interface between the PEDOT:PSS and Si, which results in splitting of the electron–hole pairs. Moving through the Au layer, the photo-generated electrons are collected by the graphene electrode which is the negative terminal of the energy storage unit. Simultaneously, photo-generated holes are released from the PEDOT:PSS and then flow toward the positive

terminal of the energy storage unit through the external circuit. This operating mechanism demonstrates the harvesting and storage of solar energy, and self-charging of the integrated power pack.

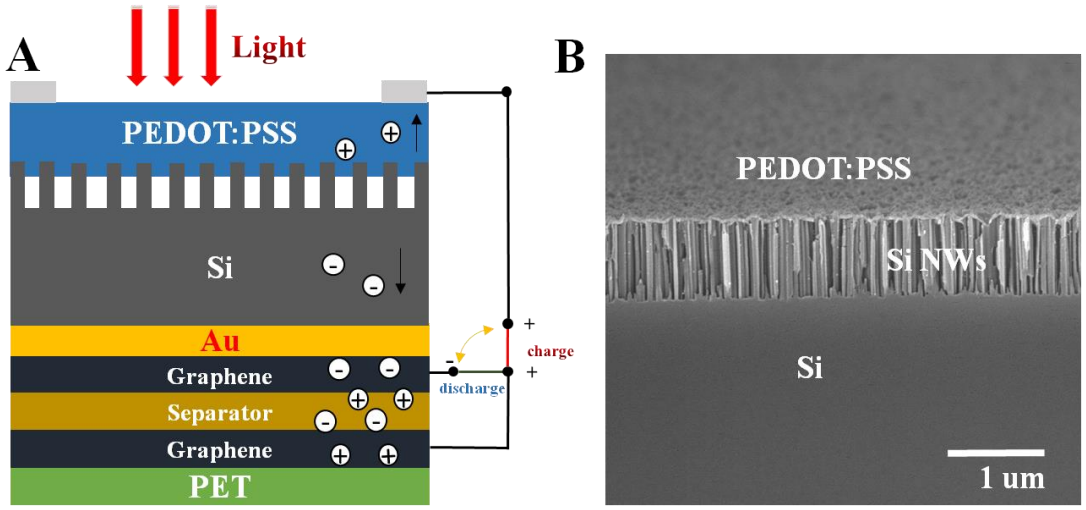

Figure 5.1 (A) A schematic illustration of the structure of a self-charging power pack consisting of a SiNW/PEDOT:PSS solar cell and a LSG supercapacitor. (B) Cross-sectional SEM image of a Si nanowire array with a PEDOT:PSS film coated on top.

A co-solvent and surfactant were usually added to the PEDOT:PSS to increase its wettability and conductivity. The solar cell performance is also critically influenced by the choice and proportion of these chemicals. Thomas and Leung[27] studied the effect of co-solvent on cell performance systemically. They demonstrated that the addition of 7 wt% EG and 0.25 wt% FS-300 in PEDOT:PSS provided a record high PCE among PEDOT:PSS/planar-Si cells. The high PCE is due to the reduction in the number and size of the micropore defects present at the interface. Based on their research, we made the PEDOT:PSS film with 7 wt % EG and 0.25 wt% FS-300. The transmission spectrum in Figure 5.2A shows that most of the incident light will not be

absorbed by the PEDOT:PSS film. Meanwhile, the sheet resistance is about 220 Ω sq^{-1}. The current density–voltage characteristics of the planar Si cell is shown in Figure 5.2B. A PCE of 7.76% was obtained as listed in Table 1.

To further improve the performance, an antireflection coating is needed. As we know, Si acts as the light harvesting material and electron hole pairs are produced inside Si, while light hits the Si through the PEDOT:PSS. However, a large portion of the incident light will be reflected by the polished surface of Si, sharply decreasing the efficiency of the solar cell. With the help of Si nanowires on the surface, the smooth surface of the Si will turn this into a rough surface. As a result, the reflection loss will be suppressed (Figure 5.2A). Figure 5.1B exhibits the tilted cross-sectional SEM images of the SiNW arrays after coating with PEDOT:PSS solution. It shows that PEDOT:PSS forms a continuous canopy above the vertically aligned SiNW arrays, demonstrating a good contact between PEDOT:PSS film and the SiNW array.

Figure 5.2B displays the current density-voltage (J-V) curves of the hybrid solar cell under AM 1.5 G (100 mW/cm^2) illumination. The SiNW/PEDOT:PSS cell shows higher short circuit current that a flat Si/PEDOT:PSS cell, consistent with the lower reflection on the SiNW surface.

The FF has also increased from 50.3% to 55.0%, which could result from enhanced carrier separation caused by increased junction area, as well as the shorter diffusion distance of minority carriers to the junction along the nanoscale diameter of the SiNWs. The change from flat Si into Si NWs caused the increase in Si surface area, leading to the increase of leakage current that was demonstrated from the dark J-V test in Figure 5.2C. There is a minute decrease of the V_{oc} from 0.53 V to 0.52 V, which could result from increased leakage current at the surface of the Si nanowires as the V_{oc} is determined by:

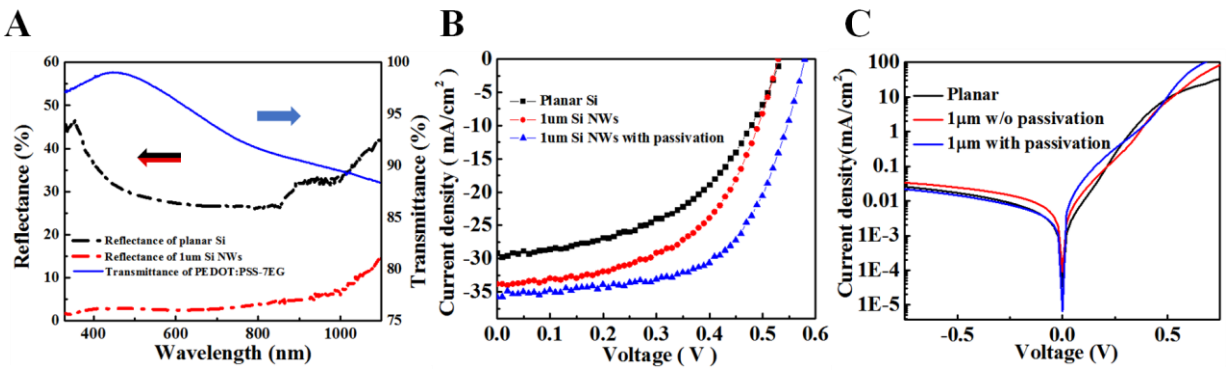

Figure 5.2 (A) Reflectance spectra of a planar Si wafer and a SiNW array, and transmittance spectrum of a PEDOT:PSS layer obtained with 7 wt% of EG and 0.25 wt% of fluorosurfactant (FS-300). (B) Current density–voltage (J–V) characteristics of the planar Si cell and a SiNW cell with and without passivation under AM 1.5 G illumination. (C) Dark current density–voltage (J–V) characteristics of the planar Si cell and a SiNW cell with and without passivation.

Table 5.1. Photovoltaic Characteristics of Si/PEDOT:PSS Solar Cells*

	V_{oc} (V)	I_{sc} (mA/cm^2)	FF	PCE
Planar	0.53	29.15	50.3%	7.77%
1um Si	0.52	33.79	55.0%	9.66%
Passivation	0.58	35.73	59.8%	12.39%

*The parameters include the short-circuit current density (I_{sc}), the open-circuit voltage (V_{oc}), the fill factor (FF), and the power conversion efficiency (PCE).

$$V_{oc} = \frac{nkT}{q} \ln\left(\frac{I_{photo}}{I_0} + 1\right) \quad (5.1)$$

where q, n, k, T, I_{photo}, and I_0 stand for electron charge, ideality factor, Boltzmann constant, temperature, photocurrent and the leakage current, respectively. A high leakage current diminishes the V_{oc}.

To overcome the leakage current issue, we used an ultrathin Al_2O_3 film for the interface passivation. As Figure 5.2C shows, with passivation of the Al_2O_3 film, the leakage current density decreased from 0.04 mA/cm^2 to 0.02 mA/cm^2. As a result, both I_{sc} and V_{oc} were significantly increased. The photovoltaic properties of the resulting cells are shown in Table 5.1. The PCE is enhanced to exceed 12%.

As mentioned above, stability and fast charge/discharge rates are crucial to the energy storage component of the power pack. So far, many supercapacitor materials have been used for energy storage in power packs.[18,22,23,30] However, among these, few can meet the requirements needed both in stability and in fast charge/discharge rates. Currently, there are no reports showing a good charge/discharge performance under a high scan rate. Generally speaking, a long cycle-life and a fast charge/discharge rate require a physical rather than a chemical energy storage mechanism. Unlike conducting polymers, an LSG supercapacitor works on pure physical processes and incurs no chemical reactions. What is more, compared to normal graphene materials, LSG sheets have no restacking problems due to their well-exfoliated surfaces. Based on these considerations, we chose the LSG supercapacitor for the energy storage component.

The fabrication and architecture of the LSG supercapacitor is shown in Figure 5.3A. With laser scribing, the brown GO film turned into a black LSG film. The LSG supercapacitor was made by sandwiching an ion porous separator [Celgard 3501 (Celgard, Charlotte, NC)] between two identical LSG electrodes. An aqueous electrolyte of 1.0 M H_2SO_4 was added. Figure 5.3C shows a top view scanning electron microscope picture of a GO film and an LSG film, respectively. The smooth plane of the GO film was converted into a rough surface composed of well-exfoliated LSG sheets, which provides large surface area for ion adsorption, leading to large double layer capacitance.

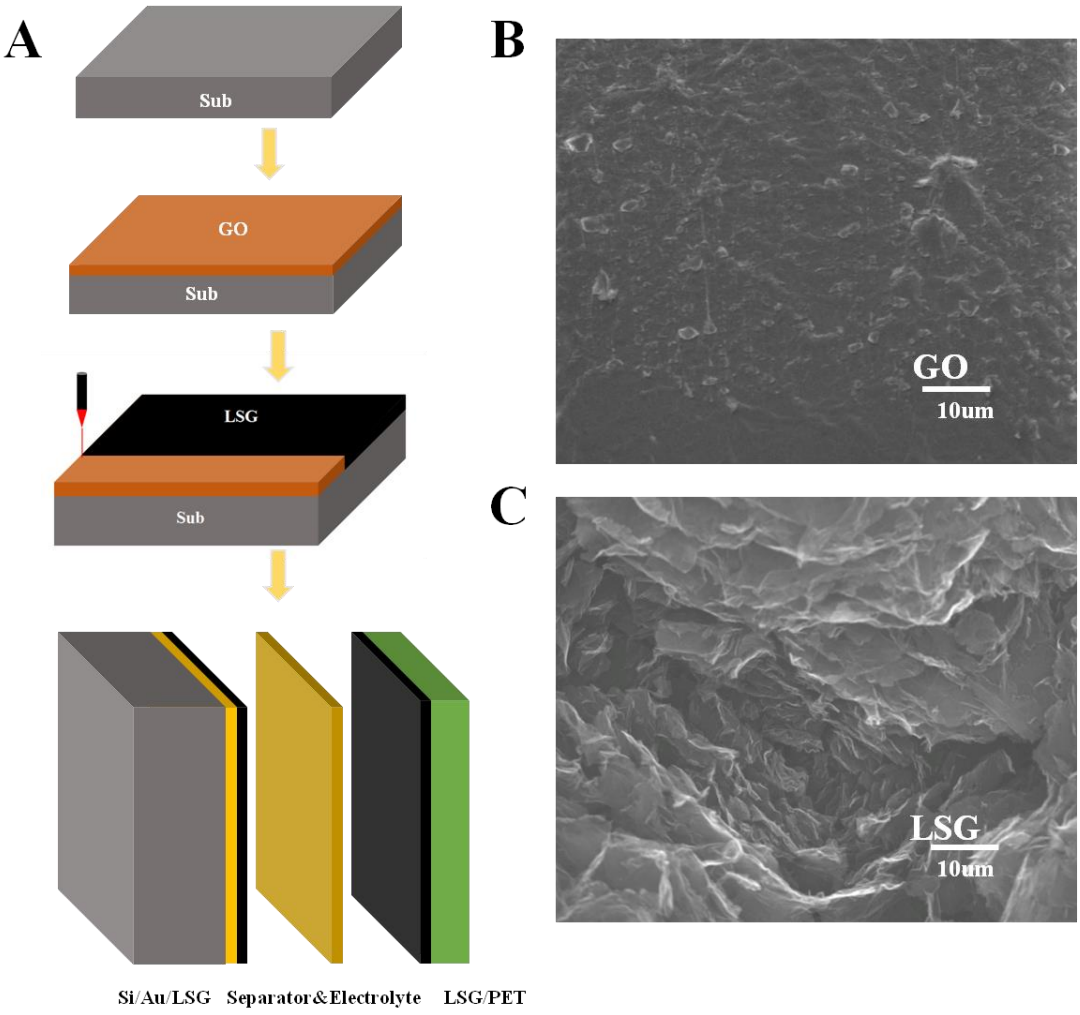

Figure 5.3 (A) A schematic illustration showing the fabrication of a laser-scribed graphene (LSG) supercapacitor. (B) SEM images of a graphene oxide (GO) film and (C) an LSG film.

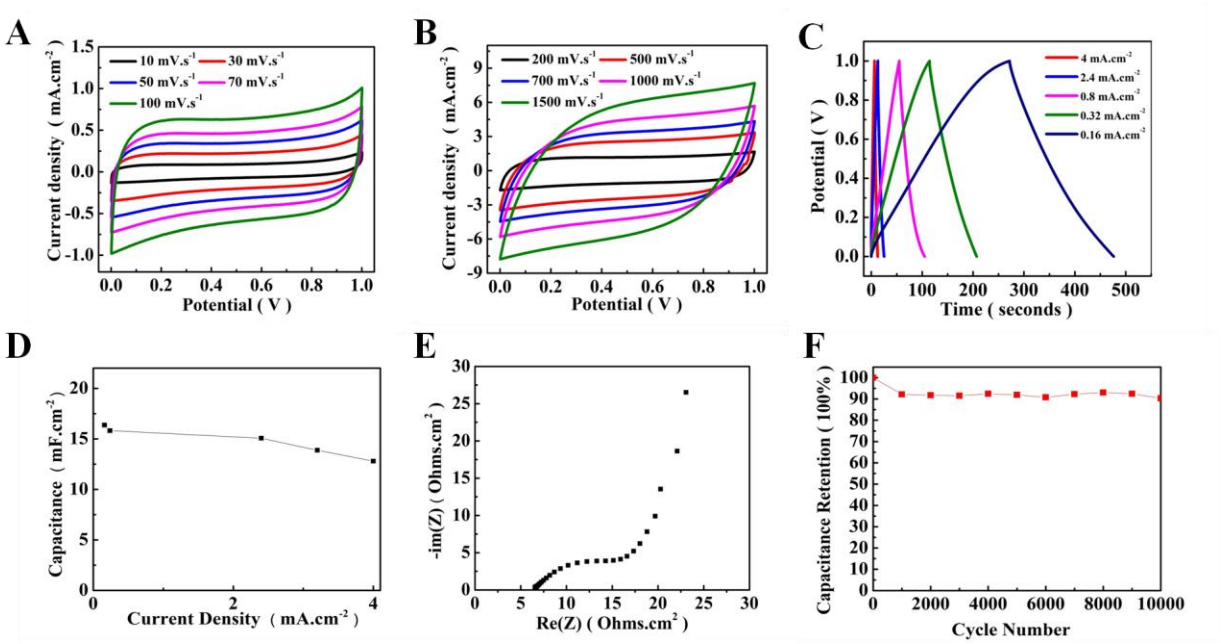

Figure 5.4 (A) (B) Cyclic voltammetry curves at various scan rates from 10 to 1500 mV/s. (C) Representative constant current (galvanostatic) charge/discharge curves at five different current densities. (D) Plot of the areal capacitance at various discharge current densities. (E) Complex plane plot of the impedance of a LSG supercapacitor. (F) Capacitance retention evaluated by repeated CV curves.

Figure 5.4A, B shows the cyclic voltammetry (CV) response of the LSG supercapacitor in a two electrode configuration at different scan rates. Rectangular shapes of the CV profile were obtained, even at a high scan rate of 1500 mV/s, indicating a rapid charge/discharge characteristic of the supercapacitor. To the best of our knowledge, there are no reports showing ideal capacitance characteristics when CV scan rates are increased up to 200 mV/s; hence, this is the best CV response so far among the reported power packs. The nearly ideal capacitive behavior is also confirmed by an essentially triangular shape of the galvanostatic curves shown in Figure 5.4C. The galvanostatic curves exhibit barely any voltage drop at the beginning of the discharge curve,

indicating a low equivalent series resistance. The areal capacitance versus discharge current density is plotted in Figure 5.4D and a high areal capacitance of 16.37 mF cm^{-2} is obtained. Moreover, the areal capacitance retains 78.2% of the initial value at a high current density (4.0 mA cm^{-2}) discharge. Electrochemical impedance spectroscopy (EIS) produces a complex plan plot of the impedance data as shown in Figure 5.4E. The series resistance is only ~10 ohms, indicative of fast ion transport within the LSG electrodes, which is consistent with the results from the galvanostatic curves. The long-term charging/discharging stability is shown in Figure 5.4F; over 90% capacitance retention is observed after 10,000 consecutive reversible cycles. For conducting polymer-based supercapacitors, by contrast, the capacitance retention drops to only 30% after 2000 cycles.[31,32]

The integrated performance of the power pack is presented in Figure 5.5. Figure 5.5A shows the first three consecutive photocharge/galvanostatic discharge cycles of the power pack. During the charging process, the power pack was irradiated at AM 1.5 G irradiation intensity. The energy harvesting functional part produces photon-generated carriers to charge the supercapacitors, which increase the voltage until it reaches the V_{oc}. In reality, the ending voltage (0.5 V) is slightly lower than the V_{oc} (0.53 V), which can be ascribed to the internal resistance. Upon discharge, the power pack was discharged with an imposed negative constant current of 5.48 A/g in the dark. The periodicity of the self-charge/galvanostatic discharge curves demonstrate a good stability of the power pack under repeated charge/discharge. Figure 5.5B shows the photo-charging curve under AM 1.5 G illumination and the discharging curves in the dark at constant current densities of 3.84, 5.48, and 10.96 A/g. Capacitance can be determined as follows:

$$C = \frac{dQ}{dV} = \frac{Idt}{dV} = \frac{I}{dV/dt} \tag{5.2}$$

From the 5.48 A/g discharge curve, an area specific capacitance of 16.37 mF/cm^2 was achieved. The energy (E_s) stored in the supercapacitor during the discharge process was then calculated to be 1.42 x 10^7 Wh, determined by the following equation:

$$E_s = \frac{1}{2} A * CV^2 \tag{5.3}$$

where A is the active area of the supercapacitor. The overall efficiency (η) of the power unit is 2.92% calculated from Equation 4:

$$\eta = \frac{E_s}{P_{in} * t_c * S} \tag{5.4}$$

where P_{in} is power input from AM 1.5 G illumination which is 100 mW/cm^2, t_c is the duration of the photo-charge and S is the effective area of the power pack under illumination. As shown in Figure 5.5C, the tandem (six units in series) power unit is able to drive a commercial red light-emitting diode.

To explore its versatile use under a wide range of light intensity conditions, particularly in an indoor environment, the photo-induced energy conversion capability of the power pack was investigated. Figure 5.5C shows photo-charging curves of the power pack at 10 mW/cm^2 and 4 mW/cm^2 illumination conditions. The light intensity in a dimly-lit living room is about 8 mW/cm^2 [38] Figure 5.5C demonstrates that the power pack can still process energy for conversion and storage under the low light intensity. The output voltage of the power pack was observed to be 0.45 V and 0.41 V respectively, which are slightly less than the output voltage under AM 1.5 G illumination. The increase of charging time is due to the decrease of the photocurrent. Unlike the outdoor solar cell module that was exposed to the AM 1.5 G illumination, most electronic products, such as

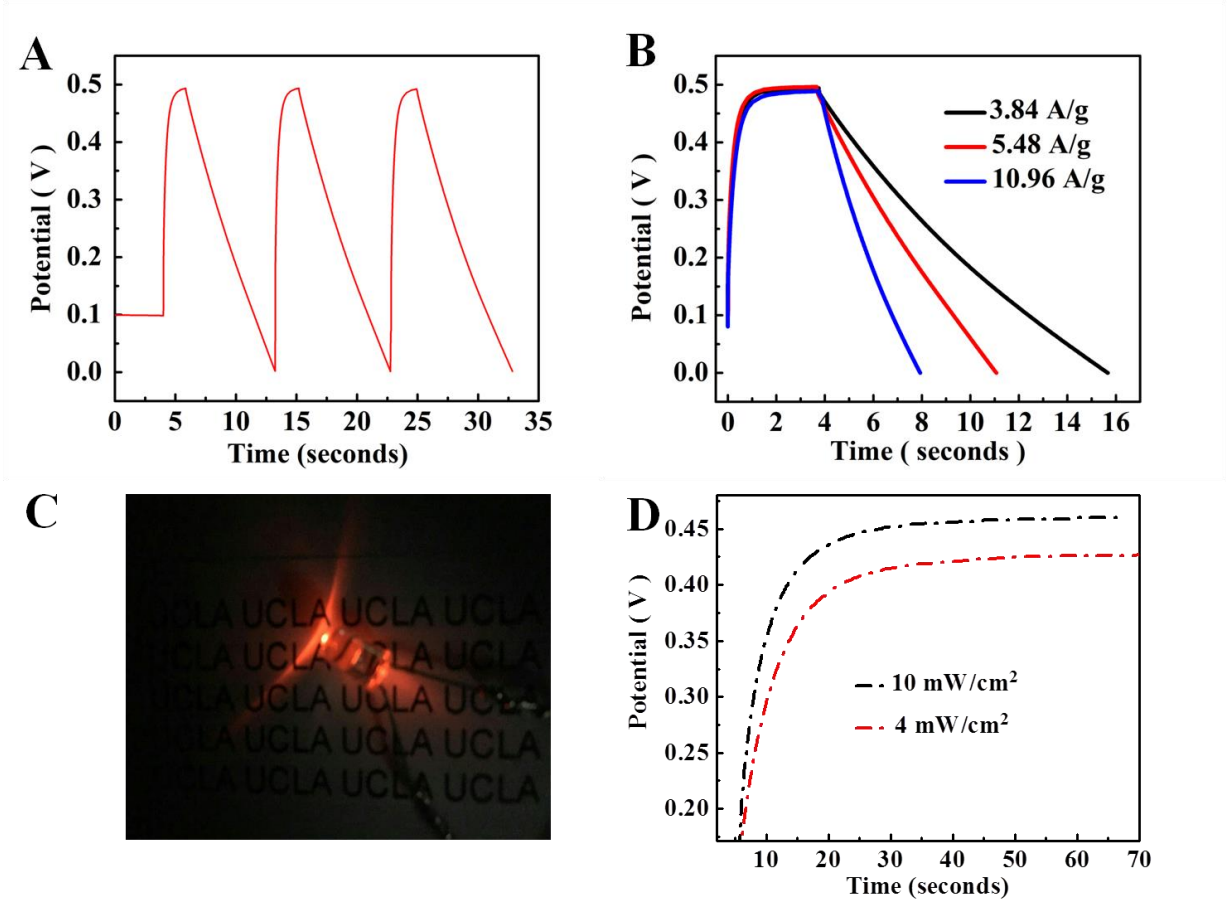

Figure 5.5 (A) Photocharge/galvanostatic discharge curves of the power pack. The discharge current was set at 5.48 A/g. (B) Photocharging under AM 1.5 G illumination and discharging in the dark at constant current densities of 3.84, 5.48 and 10.96 A/g. (C) The photograph shows an illuminated LED driven by six power packs put in series. (D) Photocharging curves of the power pack at 10 mW/cm^2 and 4 mW/cm^2 illumination conditions.

smart phones and household electrical appliances, spend most of their time under room light illumination. In this case, our power pack can provide a practical and sustainable energy supply for use in the daily life activities.

5.5 Conclusions

In summary, a new self-charging power pack consisting of a SiNW/PEDOT:PSS solar cell and an LSG supercapacitor has been demonstrated. Surface nanostructures and passivation have a substantial impact on the performance of the Si/PEDOT:PSS solar cell. With the help of surface passivation, a maximum PCE of 12.37% has been achieved for a cell with 1 μm long SiNWs. An LSG supercapacitor was combined with the hybrid solar cell through a gold common electrode. This device exhibited a superior capacitance characteristic when compared to other electrode materials used in integrated power pack systems. Excellent charge/discharge cycle stability was obtained which is essential to long service life for a hybrid power pack. Particularly, the CV response indicated successful rapid charging/discharging. The photo-induced energy conversion capability of the power pack under room light illustration has been demonstrated. Hence, this power pack could prove to be very useful for versatile, practical applications.

5.6 References

(1) Guo, W.; Xue, X.; Wang, S.; Lin, C.; Wang, Z. L. An integrated power pack of dye-sensitized solar cell and Li battery based on double-sided TiO_2 nanotube arrays. *Nano Lett.* **2012**, *12*, 2520-2523.

(2) Liu, P.; Yang, H. X.; Ai, X. P.; Li, G. R.; Gao, X. P. A solar rechargeable battery based on polymeric charge storage electrodes. *Electrochem. Commun.* **2012**, *16*, 69-72.

(3) Miyasaka, T.; Murakami, T. N. The photocapacitor: an efficient self-charging capacitor for direct storage of solar energy. *Appl. Phys. Lett.* **2004**, *85*, 3932-3934.

(4) Um, H. D.; Choi, K. H.; Hwang, I.; Kim, S. H.; Seo, K.; Lee, S. Y. Monolithically integrated, photo-rechargeable portable power sources based on miniaturized Si solar cells and printed solid-state lithium-ion batteries. *Energy Environ. Sci.* **2017**, *10*, 931-940.

(5) Zhang, X.; Huang, X.; Li, C.; Jiang, H. Dye-Sensitized Solar Cell with Energy Storage Function Through PVDF/ZnO Nanocomposite Counter Electrode. *Adv. Mater.* **2013**, *25*, 4093−4096.

(6) Yu, M.; Ren, X.; Ma, L.; Wu, Y. Integrating a redox-coupled dye-sensitized photoelectrode into a lithium-oxygen battery for photoassisted charging. *Nat. Commun.* **2014**, *5*, 5111.

(7) Chen, T.; Qiu, L.; Yang, Z.; Cai, Z.; Ren, J.; Li, H.; Lin, H.; Sun, X.; Peng, H. An Integrated "Energy Wire" for Both Photoelectric Conversion and Energy Storage. *Angew. Chem. Int. Ed.* **2012**, *51*, 11977−11980.

(8) Cheng, Y. J.; Yang, S. H.; Hsu, C. S. Synthesis of conjugated polymers for organic solar cell applications. *Chem. Rev*. **2009**, *109*, 5868-5923.

(9) De Wolf, S.; Descoeudres, A.; Holman, Z. C.; Ballif, C. High-efficiency silicon heterojunction solar cells: A review. *Green*, **2012**, *2*, 7-24.

(10) Chan, C. K.; Peng, H.; Liu, G.; McIlwrath, K.; Zhang, X. F.; Huggins, R. A.; Cui, Y. High-performance lithium battery anodes using silicon nanowires. *Nat. Nanotechnol.* **2008**, *3*, 31-35.

(11) Marom, R.; Amalraj, S. F.; Leifer, N.; Jacob, D.; Aurbach, D. A review of advanced and practical lithium battery materials. *J. Mater. Chem.* **2011**, *21*, 9938-9954.

(12) Moore, S. W.; Schneider, P. J. A review of cell equalization methods for lithium ion and lithium polymer battery systems (No. 2001-01-0959). **2001**. SAE Technical Paper.

(13) Devillers, N.; Jemei, S.; Péra, M. C.; Bienaimé, D.; Gustin, F. Review of characterization methods for supercapacitor modelling. *J. Power Sources*, **2014**, *246*, 596-608.

(14) Faraji, S.; Ani, F. N. The development supercapacitor from activated carbon by electroless plating—a review. *Renew. Sust. Energy Rev.* **2015**, *42*, 823-834.

(15) Zhang, L. L.; Zhao, X. S. Carbon-based materials as supercapacitor electrodes. *Chem. Soc. Rev.* **2009**, *38*, 2520-2531.

(16) Chen, H. W.; Hsu, C. Y.; Chen, J. G.; Lee, K. M.; Wang, C. C.; Huang, K. C.; Ho, K. C. Plastic dye-sensitized photo-supercapacitor using electrophoretic deposition and compression methods. *J. Power Sources*, **2010**, *195*, 6225-6231.

(17) Scalia, A.; Bella, F.; Lamberti, A.; Bianco, S.; Gerbaldi, C.; Tresso, E.; Pirri, C. F. A flexible and portable powerpack by solid-state supercapacitor and dye-sensitized solar cell integration. *J. Power Sources*, **2017**, *359*, 311-321.

(18) Murakami, T. N.; Kawashima, N.; Miyasaka, T. A high-voltage dye-sensitized photocapacitor of a three-electrode system. *ChemComm*. **2015,** *26*, 3346-3348.

(19) Xia, X.; Luo, J.; Zeng, Z.; Guan, C.; Zhang, Y.; Tu, J.; Zhang, H.; Fan, H. J. Integrated Photoelectrochemical Energy Storage: Solar Hydrogen Generation and Supercapacitor. *Sci. Rep.* **2012**, *2*, 981.

(20) Wee, G.; Salim, T.; Lam, Y. M.; Mhaisalkar, S. G.; Srinivasan, M. Printable photo-supercapacitor using single-walled carbon nanotubes. *Energy Environ. Sci.* **2011**, *4*, 413-416.

(21) Zhang, Z.; Chen, X.; Chen, P.; Guan, G.; Qiu, L.; Lin, H.; Yang, Z.; Bai, W.; Luo, Y., Peng, H. Integrated polymer solar cell and electrochemical supercapacitor in a flexible and stable fiber format. *Adv. Mater.* **2014**, *26*, 466-470.

(22) Liu, Z.; Zhong, Y.; Sun, B.; Liu, X.; Han, J.; Shi, T.; Tang, Z.; Liao, G. Novel Integration of Perovskite Solar Cell and Supercapacitor based on Carbon Electrode for Hybridizing Energy Conversion and Storage. *ACS Appl. Mater. Interfaces*. **2017**, *9*, 22361–22368.

(23) Liu, R.; Wang, J.; Sun, T.; Wang, M.; Wu, C.; Zou, H.; Song, T.; Zhang, X.; Lee, S.T.; Wang, Z.L.; Sun, B. Silicon Nanowire/Polymer Hybrid Solar Cell-Supercapacitor: A Self-Charging Power Unit with a Total Efficiency of 10.5%. *Nano Lett*. **2017**, *17*, 4240–4247.

(24) Li, G.; Zhu, R.; Yang, Y. Polymer solar cells. *Nat. Photonics*, **2012**, *6*, 153.

(25) Huo, L.; Liu, T.; Sun, X.; Cai, Y.; Heeger, A. J.; Sun, Y. Single‐Junction Organic Solar Cells Based on a Novel Wide‐Bandgap Polymer with Efficiency of 9.7%. *Adv. Mater*. **2015**, *27*, 2938.

(26) So, S.; Hwang, I.; Schmuki, P. Hierarchical DSSC structures based on "single walled" TiO_2 nanotube arrays reach a back-side illumination solar light conversion efficiency of 8%. *Energy Environ. Sci.* **2015**, *8*, 849.

(27) Thomas, J. P.; Leung, K. T. Defect-minimized PEDOT: PSS/planar-Si solar cell with very high efficiency. *Adv. Funct. Mater.* **2014***, 24*, 4978-4985.

(28) He, L.; Jiang, C.; Wang, H.; Lai, D. Simple approach of fabricating high efficiency Si nanowire/conductive polymer hybrid solar cells. *IEEE electron device let.* **2011**, *32*, 1406-1408.

(29) Park, K.T.; Kim, H.J.; Park, M.J.; Jeong, J.H.; Lee, J.; Choi, D.G.; Lee, J.H.; Choi, J.H. 13.2% efficiency Si nanowire/PEDOT: PSS hybrid solar cell using a transfer-imprinted Au mesh electrode. *Sci. Rep.* **2015**, *5*, 12093.

(30) Xu, X.; Li, S.; Zhang, H.; Shen, Y.; Zakeeruddin, S. M.; Graetzel, M.; Cheng, Y.B.; Wang, M. A power pack based on organometallic perovskite solar cell and supercapacitor. *ACS Nano*, **2015,** *9*, 1782-1787.

(31) Huang, Y.; Li, H.; Wang, Z.; Zhu, M.; Pei, Z.; Xue, Q.; Huang, Y.; Zhi, C. Nanostructured polypyrrole as a flexible electrode material of supercapacitor. *Nano Energy*, **2016**, *22*, 422-438.

(32) Liu, T.; Finn, L.; Yu, M.; Wang, H.; Zhai, T.; Lu, X.; Tong, Y.; Li, Y. Polyaniline and polypyrrole pseudocapacitor electrodes with excellent cycling stability. *Nano Lett.* **2014**, *14*, 2522-2527.

(33) Wang, Y.; Shi, Z.; Huang, Y.; Ma, Y.; Wang, C.; Chen, M.; Chen, Y. Supercapacitor devices based on graphene materials. *J. Phys. Chem. C*, **2009**, *113*, 13103-13107.

(34) El-Kady, M. F.; Strong, V.; Dubin, S.; Kaner, R. B. Laser scribing of high-performance and flexible graphene-based electrochemical capacitors. *Science*, **2012**, *335*, 1326-1330.

(35) Wang, Y.; Shi, Z.; Huang, Y.; Ma, Y.; Wang, C.; Chen, M.; Chen, Y. Supercapacitor devices based on graphene materials. *J. Phys. Chem. C*, **2009**, *113*, 13103-13107.

(36) Gao, W.; Singh, N.; Song, L.; Liu, Z.; Reddy, A.L.M.; Ci, L.; Vajtai, R.; Zhang, Q.; Wei, B.; Ajayan, P.M. Direct laser writing of micro-supercapacitors on hydrated graphite oxide films. *Nat. Nanotechnol.* **2011***, 6*, 496-500.

(37) Huang, Z.; Geyer, N.; Werner, P.; De Boor, J.; Gösele, U. Metal-assisted chemical etching of silicon: a review. *Adv. Mater.* **2011**, *23*, 285-308.

(38) Butler, D.L; Biner, P.M. Preferred lighting levels: Variability among settings, behaviors, and individuals. *Environ. Behav.* **1987**, *19*, 695–721.

CHAPTER 6

Conclusion and Future Work

6.1 Conclusions

In this dissertation, we studied novel materials for use as electrodes, electrolyte sand separators to boost the performance of supercapacitors. Power units were also built based on advanced supercapacitors, enabling energy generation and storage at the same time.

The first project described embedding hollow Co_3O_4 nanoboxes into three-dimensional laser scribed graphene (LSG) to improve the electrochemical performance of carbon-based supercapacitors. The capacity of the Co_3O_4/LSG is enhanced due to the huge charge storage capacity of the metal oxide from redox reactions, while LSG serves as a conductive scaffold to maintain high power. Thanks to the unique hollow structure, not only the outer surface, but also the inner surface of the metal oxide is exposed to the electrolyte. In this way, ions can diffuse freely, minimizing the ion diffusion resistance in the system. The material will also be utilized efficiently and there will be less dead mass. The composite material exhibits a high volumetric capacity of 60.0 C/cm^3, which can be transformed into a specific capacity of 542.3 C/g. The capacity of the composite kept increasing for the first several hundred cycles due to the activation process of the graphene. It is also able to maintain 113.1% of its original capacity after 10,000 cycles.

The second project focused on boosting the energy density of state-of-the-art activated carbon supercapacitors by combining laser scribing with a redox active electrolyte. The laser scribing process provides the activated carbon with a more porous structure, facilitating ion diffusion and the accessibility of the active material, which improves the capacitance. The

introduction of $Fe(CN)_6^{3-}/Fe(CN)_6^{4-}$ as a redox electrolyte enlarges the potential window to 2 V as well as further enhances the capacitance by redox reactions. Our device with laser scribed activated carbon in a redox electrolyte was able to store 9 times greater energy density than a traditional activated carbon supercapacitor. It is also capable of charging 700 times faster than a Li thin-film battery.

In the third project, a self-charging supercapacitor was developed to harvest biomechanical energy by utilizing the piezoelectric material as the separator. When the device undergoes stress, a potential difference between two faces of the piezoelectric film develops and the supercapacitor can be charged spontaneously. ZnO with diverse particle sizes were studied as sacrificial templates to optimize the pore size and pore volume of the polyvinylidene fluoride (PVDF) separator. In this way, the separator film will have both good piezoelectric and ion diffusion processes. When applying the film as a separator between two polyaniline electrodes, the supercapacitor was able to generate >0.2 V by palm pressing.

The last project was to build a power unit by integration of a silicon nanowire array/PEDOT:PSS solar cell with an LSG supercapacitor. With surface passivation of Al_2O_3, the solar cell reached a high power conversion efficiency (PCE) of 12.37%. The LSG supercapacitor was connected to the solar cell by a gold electrode in common. Thanks to the high conductive network of LSG, it is able to handle the high current from the solar cell and showed good electrochemical performance. The power pack was able to store energy at a total conversion efficiency of 2.92%. By connecting 6 power units in series, a red LED was able to be lit up.

Although we have made a lot of progress in the area of supercapacitors, there is still room to improve, which we will discuss in the next section.

6.2 Future work

Supercapacitors are promising for applications such as portable electronic devices, electric vehicles and regenerative braking thanks to their unique properties.[1] However, the energy density of state-of-the-art supercapacitors is still way too low when compared to lithium ion batteries.[2-3] This is the number one problem that prevents them from more potential applications nowadays. It is reported that the energy density of a supercapacitor is proportional to its capacitance and the square of its voltage window.[4]

$$\mathrm{E} = \frac{1}{2} C V^2 \tag{6.1}$$

In order to improve the energy density, scientists are trying to develop new types of electrode materials with high charge storage capability. There are also numerous research projects on novel electrolytes to enhance the electrochemical performance of supercapacitors. In future work, we would like to focus on applications of redox electrolytes for supercapacitors.

6.2.1 Introduction to redox electrolytes

Redox electrolytes can be made by dissolving redox additives into traditional electrolytes. Common redox couples include $Fe(CN)_6^{3-}/Fe(CN)_6^{4-}$, Cu_2^{+}/Cu^{+}, VO_2^{+}/VO^{2+} and some organic molecules such as methylene blue and viologens.[5] The capacity of the electrode will be enhanced by Faradaic reactions resulting from the redox couples on the electrolyte-electrode interfaces.[6] As reported, redox electrolytes have been used as an inexpensive method to improve the charge storage performance for supercapacitors. Hwang *et al*.[7] boosted the areal capacitance of their LSG/Fe_3O_4 4 times by use of the $Fe(CN)_6^{3-}/Fe(CN)_6^{4-}$ redox couple. Mai *et al*.[8] observed a 10-fold

increase in volumetric capacitance with the help of a redox electrolyte. Redox electrolytes can even be utilized to protect the current collector from corrosion.[9]

However, there are also issues with redox electrolytes, such as the low cycle life of some redox couples. Most redox electrolytes also have sharp redox peaks over a small potential range, which is not practical for applications.

6.2.2 Hydroquinone/Benzoquinone (HQ/BQ) redox couple to enhance the performance of polyaniline electrodes

Polyaniline (PANI) is a typical battery-like material for supercapacitors. It is well studied due to its good specific capacity.[10] However, we have observed one problem when we test a symmetric device of PANI as shown in Figure 6.1B. The cyclic voltammetry (CV) curve of the device shows a good current density at low potential, while there is barely any current in the high potential range. As a result, the device discharges very quickly, resulting in a sharp potential drop from 0.8 V to 0.5 V as the constant current charging/discharging curves (CC) illustrates in Figure 6.1C. It would be a disaster for real world applications since electronic devices all need a minimum voltage to work.

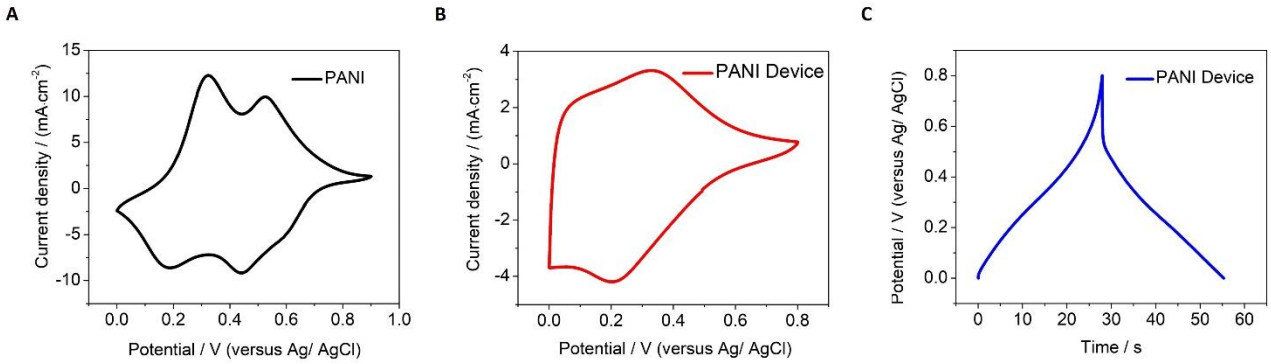

Figure 6.1 (A) Cyclic voltammetry (CV) of PANI in a three-electrode set-up showing two pairs of redox peaks. (B) CV of PANI in a two-electrode device. (C) Constant current charging/discharging curves (CC) of PANI in a device.

The phenomenon of charge drop is due to the fluctuation of PANI's current density at different potentials. To solve this problem, we would like to introduce a redox electrolyte into our system to balance the charge storage capacity of PANI over its potential window. The redox couple of HQ/BQ is a good choice since it has an oxidation peak around 0.5 V and a reduction peak around 0.3 V, which are between those of PANI as Figure 6.1A exhibits. With a well-designed concentration of the redox couple, it is possible for the PANI to endure a relatively constant current throughout its potential window. The problem of the dramatic charge drop could thus be fixed.

Future work for this project will include testing HQ/BQ under different current densities to figure out the best concentration, and the use of multiple redox couples if HQ/BQ can't fix the problem.

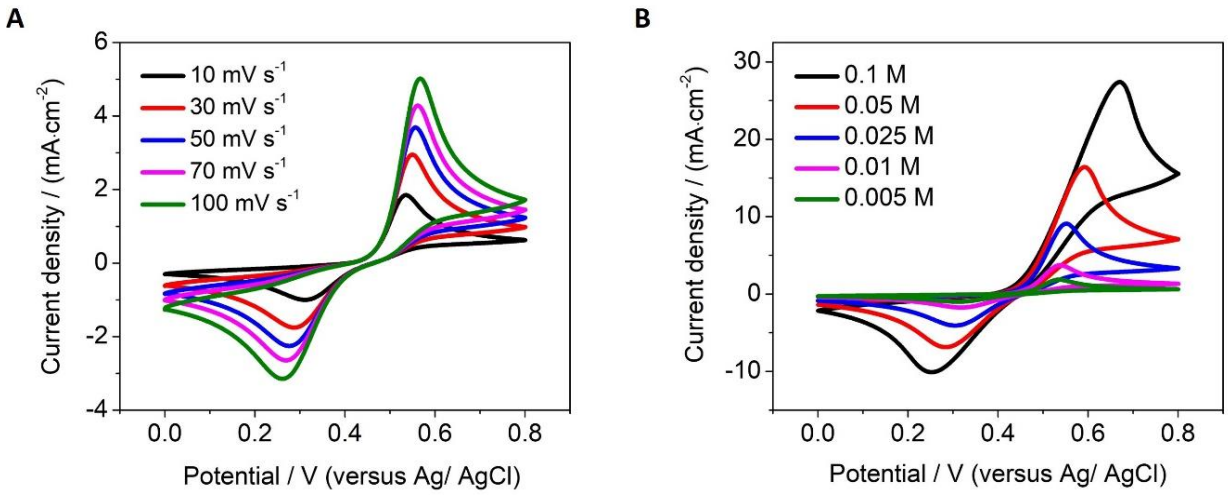

Figure 6.2 (A) CV curves of 0.005 M HQ/BQ redox couple in 1 M H_2SO_4 under different scan rates. (B) CV profiles of HQ/BQ (0.1 M – 0.005 M) at the scan rate of 10 mV/s.

6.2.3 Mimicking the performance of pseudo-capacitive materials by superimposing of several redox electrolytes

As discussed in the introduction, one drawback of redox electrolytes is that they only have high capacity over a small potential range. As Figure 6.3 shows, all 6 different types of redox couples show sharp redox peaks. There is almost no capacity other than under the peak areas. As a result, the role of a redox electrolyte is usually to improve or balance the capacity in addition to other solid active materials. This has limited their application as redox-active materials for supercapacitors.

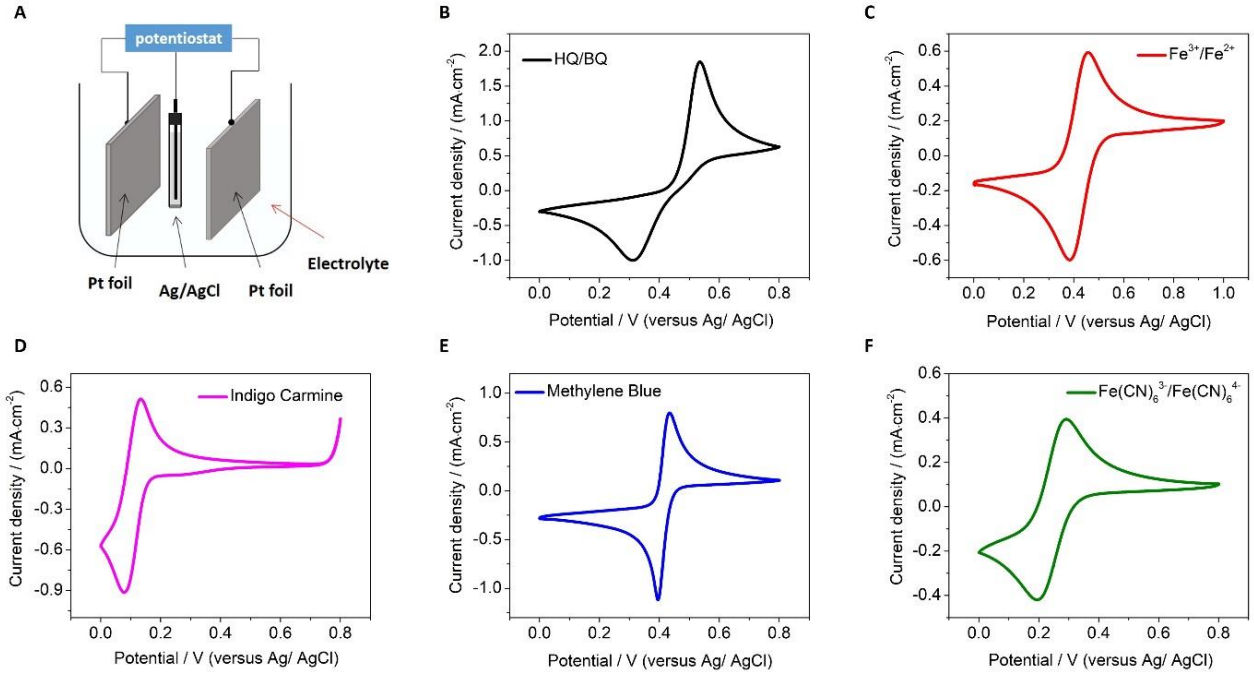

Figure 6.3 (A) Three-electrode step-up for measuring the electrochemical performance of redox couples. Platinum foils are used as both working and counter electrodes and an Ag/AgCl

electrode works as the reference. (B) CV curve of 0.005 M hydroquinone/benzoquinone in 1 M H_2SO_4. (C) CV curve of 0.005 M Fe^{2+}/Fe^{3+} in 1 M H_2SO_4. (D) CV curve of 0.005 M indigo carmine in 1 M H_2SO_4. (E) CV curve of 0.005 M methylene blue in 1 M H_2SO_4. (F) CV curve of 0.005 M $Fe(CN)_6^{3-}/Fe(CN)_6^{4-}$ in 1 M Na_2SO_4. The CVs were tested at 10 mV/s.

Lin *et al.*[11] reported in their Science paper that they are able to reach a rectangular electric double layer capacitor (EDLC) like CV curve when they mix three different materials with Faradaic peaks together. Inspired by their idea, we would like to dissolve multiple redox couples together. With a rational choice of the redox species and the concentration to use, it is expected to show a plateau over a broader potential range and therefore redox electrolytes can be utilized as the active material for charge storage.

In order to figure out which redox additives to select, we made summaries of the reduction potentials of diverse redox couples based on our experiments and literature values[5] as shown in Figure 6.4. Figure 6.4A sums up the redox couples that work in a neutral environment, while Figure 6.4B is a summary of those that function in an acidic electrolyte. By comparison of the two

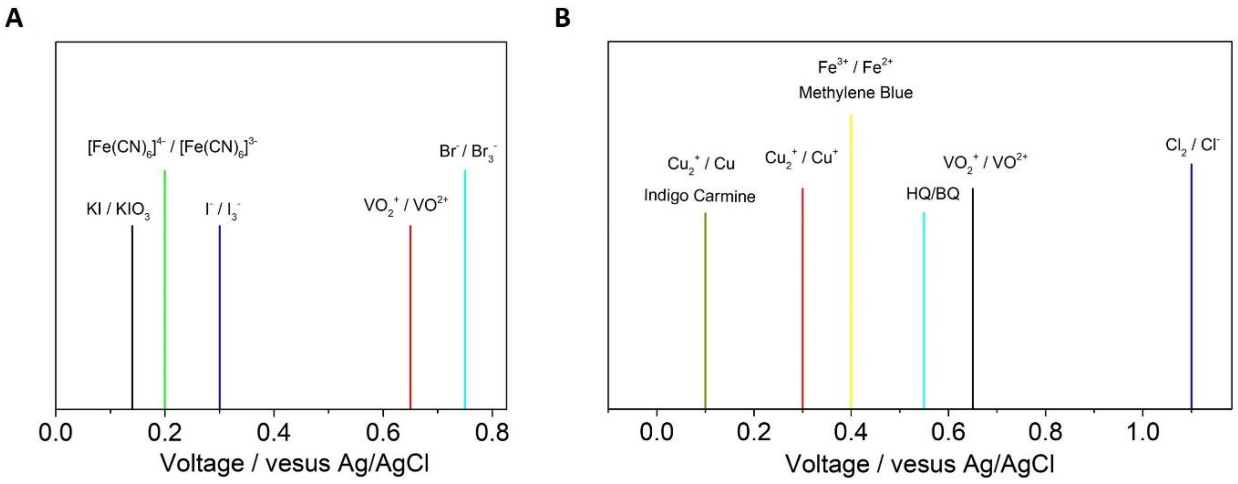

Figure 6.4 Reduction potentials of redox couples in (A) 1 M Na_2SO_4 and (B) 1 M H_2SO_4 versus an Ag/AgCl reference.

figures, we prefer to choose the redox additives in Figure 6.4B since they are spread over a wider potential range. Indigo carmine, Fe^{2+}/Fe^{3+} and VO_2^{+}/VO^{2+} would be ideal since they each have 0.2 V difference for their reduction potentials.

In the future, we would like to do CV tests on the three materials mentioned above. By comparing their peak current densities at different scan rates, we will calculate the optimal ratio in which to mix them and create an ideal EDLC-like shape.

6.3 References

(1) Miller, J. R.; Burke, A. F. Electrochemical capacitors: challenges and opportunities for real-world applications. *Electrochem. Soc. Interface* **2008**, *17*, 53.

(2) Burke, A. R&D considerations for the performance and application of electrochemical capacitors. *Electrochim. Acta* **2007**, *53*, 1083-1091.

(3) Simon, P.; Gogotsi, Y. Materials for electrochemical capacitors. *Nat. Mater.* **2008**, *7*, 845-854.

(4) Conway, B. E. *Electrochemical supercapacitors: scientific fundamentals and technological applications*; Springer Science & Business Media: New York, **2013**.

(5) Chun, S.E.; Evanko, B.; Wang, X.; Vonlanthen, D.; Ji, X.; Stucky, G.D.; Boettcher, S.W. Design of aqueous redox-enhanced electrochemical capacitors with high specific energies and slow self-discharge. *Nat. Commun.* **2015**, *6*, 7818.

(6) Senthilkumar, S.T.; Selvan, R.K.; Melo, J.S. Redox additive/active electrolytes: a novel approach to enhance the performance of supercapacitors. *J Mater. Chem. A*, **2013**, *1*, 12386-12394.

(7) Hwang, J.Y.; El-Kady, M.F.; Li, M.; Lin, C.W.; Kowal, M.; Han, X.; Kaner, R.B. Boosting the capacitance and voltage of aqueous supercapacitors via redox charge contribution from both electrode and electrolyte. *Nano Today*, **2017**, *15*, 15-25.

(8) Mai, L.Q.; Minhas-Khan, A.; Tian, X.; Hercule, K.M.; Zhao, Y.L.; Lin, X.; Xu, X. Synergistic interaction between redox-active electrolyte and binder-free functionalized carbon for ultrahigh supercapacitor performance. *Nat. Commun.* **2013**, *4*, 2923.

(9) Abbas, Q.; Ratajczak, P.; Béguin, F. Sodium molybdate–an additive of choice for enhancing the performance of AC/AC electrochemical capacitors in a salt aqueous electrolyte. *Faraday discussions*, **2014**, *172*, 199-214.

(10) Wang, Y.; Wei, H.; Wang, J.; Liu, J.; Guo, J.; Zhang, X.; Weeks, B. L.; Shen, T. D.; Wei, S.; Guo, Z. Electropolymerized polyaniline/manganese iron oxide hybrids with an enhanced color switching response and electrochemical energy storage. *J. Mater. Chem. A* **2015**, *3*, 20778-20790.

(11) Lin, T.; Chen, I.W.; Liu, F.; Yang, C.; Bi, H.; Xu, F.; Huang, F. Nitrogen-doped mesoporous carbon of extraordinary capacitance for electrochemical energy storage. *Science*, **2015**, *350*, 1508-1513.